FACULTY OF SCIENCE
UNIVERSITY OF COPENHAGEN

PhD thesis

Peter Krogstrup

Dynamical Theory and Experiments on GaAs Nanowire Growth for Photovoltaic Applications

Niels Bohr Institute
University of Copenhagen
Denmark

Academic advisor: Jesper Nygård

Submitted: 13/10/2012

The PhD School of Science, Faculty of Science, University of Copenhagen, Denmark

Abstract

The geometry of nanowire solar cells provides many potential advantages compared to planar solar cells, such as reduced reflection, built-in light concentration due to absorption resonances, improved band gap tuning for multi-junction devices and an increased defect tolerance. Moreover, the use of nanowires reduces the quantity of material necessary to approach the limits of light to electric power conversion efficiency, allowing for substantial cost reductions if they are grown on a cheap substrate. However, it is far from straightforward to achieve optimum design of bottom up grown nanowire solar cells, as it requires control and an in-depth understanding of complex growth kinetics controlling the nanowire crystal formation and dopant incorporation.

This thesis is concerned with the growth of self catalyzed GaAs based semiconductor nanowires on silicon substrates in a molecular beam epitaxy system, with the aim of growing nanowires for highly efficient photovoltaic applications. As it is crucial to control and understand the mechanisms behind the nanowire crystal formation, not only in terms of the overall nanowire morphology but also in terms of the crystal phase purity, this thesis begins with a formulation of a theoretical framework which can serve as a basis to model and understand the dynamics of III-V nanowire growth via the 'vapor-liquid-solid' method. The formalism is based on principles from transition state kinetics driven by a Gibbs free energy minimization process. The crystallization process is described in terms of a dynamic liquid-solid growth system which continuously seeks to lower the excess Gibbs free energy originating from the adatoms and gas states. Nucleation statistics and the nucleation limited growth at the topfacet which force the solid-liquid growth system far from equilibrium are discussed in detail. Self-catalyzed GaAs nanowire growth which will be the main focus for the photovoltaic applications is used as a model system, and examples of in depth dynamical simulations compared with experiments are shown. The work gradually involves more detailed growth experiments such as in-situ x-ray characterization of growing nanowires and growth of advanced photovoltaic structures and finally photovoltaic characterization of both lying and standing single nanowire devices are presented. All the different kind of single NW

solar cell devices show an enormous potential as light absorbers. Especially the single vertical NW solar cells which are characterized as grown on the substrate shows an apparent solar cell efficiency of $\eta_{eff}^{app} \cong 40\%$ and a photo generated current which is much higher than previous reported on single NW solar cells.

Resumé på dansk

Denne afhandling beskæftiger sig med væksten af selv-katalyserede GaAs baserede halvleder nanotråde (nanowires), med det formål at producere nanowires til højeffektive fotoelektriske applikationer, heraf primært solceller. Selve væksten af nanowires foregår i et ultra høj vacuum kammer (kaldet et ”molekylær epitaxy system”) hvor det relevante materiale ankommer i form af en termisk atomar beam flux. Da det er afgørende at kunne kontrollere og forstå mekanismerne bag nanowirenes krystal formation, ikke kun i forhold til den samlede nanowire morfologi men også i form af krystallernes kvalitet, begynder denne afhandling med en formulering af en teoretisk ramme, der kan tjene som et grundlag til at modellere og forstå dynamikken i III-V nanowire vækst via "vapor-liquid-solid”-metoden. Formalismen er baseret på principper fra overgangstilstand kinetik drevet af minimering af Gibbs fri energi. Selve krystallisationsprocessen er beskrevet i en dynamisk formulering af væske-faststof-overgangen, som kontinuerligt søger at sænke den overskydende Gibbs fri energi som stammer fra overflade og beam flux atomerne. Statistisk kim-dannelses teori og kimdannelse-begrænset vækst på den dominerende dyrkningsfront som tvinger faststof-væske systemet langt fra ligevægt er diskuteret i detaljer. Selv-katalyseret GaAs nanowire vækst, som vil være den primære fokus for de fotoelektriske applikationer bruges som et modelsystem, og eksempler på dybdegående og detajleret dynamiske simuleringer sammenlignes med resultater fra forsøg som er udført under projektet. Gradvist introduceres mere detaljerede vækst eksperimenter som fører til avancerede solceller strukturer og endelig fotoelektrisk karakterisering af både liggende og stående enkelt nanowire solceller bliver præsenteret. De forskellige nanowire solceller, viser alle et enormt potentiale som lys-absorbers og lys koncentratorer. Især de solceller, der karakteriseres som dyrket på substratet, udviser en tilsyneladende solcelle effektivitet og en lysgenereret strøm, som er meget højere end tidligere rapporteret på enkelt nanowire solceller. På grund af geometrien af nanowire solceller, er der mange umiddelbare fordele i forhold til plane solceller, såsom reduceret refleksion, indbygget lys koncentration på grund af absorption resonanser, større frihed for båndgab tuning for multi-junction-celler og en forøget defekt tolerance. Endvidere reducerer anvendelsen af nanowires den mængde materiale nødvendig for at nærme sig grænserne

for lys til el effektivitetsgrænsen, hvilket tillader betydelige omkostningsbesparelser hvis de dyrkes på et billigt substrat. Men det er langt fra ligetil at opnå et optimalt design af nanowire solceller, da det kræver en dybdegående forståelse af den komplekse vækst-kinetik der kontrollerer nanowirenes krystal formation og doterings inkorporations mekanismer. Dette vil derfor have primære fokus i denne afhandling.

Contents

List of papers and contributions

The following list of papers will be referred to in the text as references I-X.

----------- Papers which are concerned with the mechanisms of nanowire growth:

I. **Theoretical formalism of III-V nanowire growth dynamics via the vapor-liquid-solid mechanism**
P. Krogstrup, H. Ingerslev, E. Johnson, M. H. Madsen, C. B. Sørensen, A. Fontcuberta i Morral, M. Aagesen, J. Nygård, F. Glas, submitted to *Phys. Rev. B.* (Nov 2012)
I was the primary investigator of this project, including all the writing

II. **Structural phase control in self-catalyzed Growth of GaAs nanowires on Silicon (111)**
P. Krogstrup, R. Popovitz-Biro, E. Johnson, M. H. Madsen, J. Nygård and H. Shtrikman, *Nano Letters*, 10, 4475 (2010)
I wrote the paper, did the analysis and interpretation of data, and carried out approximately half of the NW growth experiments

III. **Impact of the liquid phase shape on the structure of III-V nanowires**
P. Krogstrup, S. Curiotto, E. Johnson, M. Aagesen, J. Nygård and D. Chatain *Phys. Rev. Lett.* 106, 125505 (2011)
I was the primary investigator of this project, including all the writing

IV. **In-situ x-ray characterization of wurtzite formation in GaAs nanowires**
P. Krogstrup[§], M. H. Madsen[§], W. Hu, M. Kozu, Y. Nakata, J. Nygård, M. Takahasi and R. Feidenhans'l, *App. Phys. Lett.* 100, 093103 (2012)
I got the idea for the project, took active part in the data acquiring at the x-ray synchrotron in Japan, and was the primary driving force in the data analysis and writing the paper

V. ***Junctions in axial III-V heterostructure nanowires obtained via an interchange of group III elements**
P. Krogstrup, J. Yamasaki, C. B. Sørensen, E. Johnson, J. B. Wagner, R. Pennington, M. Aagesen, N. Tanaka and J. Nygård, *Nano Letters*, 9, 11, 3689 (2009)
I was the primary investigator of this project, including all the writing

VI. **Three-Dimensional Multiple-Order Twinning of Self-Catalyzed GaAs Nanowires on Si Substrates**
E. Uccelli, J. Arbiol, C. Magen, P. Krogstrup, E. Russo-Averchi, M. Heiss, G. Mugny, F. Morier-Genoud, J. Nygård, J. R. Morante, and A. Fontcuberta i Morral, *Nano Letters*, 11, 9, 3827 (2011)
I took active part in both the nanowire growths and data analysis

VII. Influence of the oxide layer for growth of self-assisted InAs nanowires on Si(111)
M. H. Madsen, M. Aagesen, P. Krogstrup, C. Sørensen and J. Nygård, *Nanoscale Res. Lett.* 6, 516 (2011)
I participated actively in both the discussions regarding the data and the growths experiments

VIII. Suppression of three dimensional twinning for a 100% yield of vertical GaAs nanowires on silicon
E. Russo-Averchi, M. Heiss, L. Michelet, P. Krogstrup, J. Nygård, C. Magen, J. R. Morante, E. Uccelli, J. Arbiol, and A. Fontcuberta i Morral, *Nanoscale*, 4, 1486 (2012)
I took active part in both the nanowire growths and data analysis

IX. Experimental determination of diffusion lengths for growth of InAs nanowires
M. H. Madsen, P. Krogstrup, E. Johnson, S. Venkatesan, E. Mühlbauer, C. Scheu, C. B. Sørensen and J. Nygård, under review, Jour. of Crys. Growth. (Oct 2012)
I contributed with ideas for the project, participated actively in both the discussions regarding the data and the growths experiments

X. Doping incorporation and acceptor deactivation in Be-doped GaAs nanowires
A.Casadei[§], P. Krogstrup[§], J. Rohr, S. Upadhyay, J. Nygård, A. Fontcuberta i Morral, *App. Phys. Lett* (Accepted, Nov. 2012)
I did all the nanowire growths, participated actively in the data interpretation

----------- Papers concerned with the photovoltaic properties of GaAs nanowires:

XI. Enhanced photon collection in a single as-grown nanowire solar cell
P. Krogstrup[§], H. I. Jørgensen[§], M. Heiss[§], O. Demichel, J. V. Holm, M. Aagesen, J. Nygård, A. Fontcuberta i Morral, under review, *Nature Photonics* (Oct, 2012)
I got the idea for the project, I did all the positioned solar cell nanowire growths and participated actively in the data interpretation and writing

XII. Engineering light absorption in single-nanowire solar cells with metal nanoparticles
C. Colombo, P. Krogstrup, J. Nygård, M. L Brongersma and A. Fontcuberta i Morral, *New Journal of Physics* 14 (2011)
I did the nanowire growth and took a minor role in discussing the data and solar cell device processing.

XIII. Gold free GaAsP single nanowire solar cells grown on silicon
J.V. Holm[§], H. I. Jørgensen[§], P. Krogstrup, J. Nygård, H. Liu and M. Aagesen, Under review, *Nature Photonics* (Oct, 2012)
I took an active part discussing the NW solar cell growth and discussing the data.

XIV. An electrically-driven GaAs Nanowire Surface Plasmon Source
P. Fan, C. Colombo, K. C. Y. Huang, P. Krogstrup, J. Nygård, A. Fontcuberta i Morral and M. L. Brongersma, *Nano Letters*, 12, 9 (2012)
I did the nanowire growth

XV. Statistically relevant contacting procedure of nanowires: application to a single nanowire solar cell and light emitting diode.
P. Blanc, M. Heiss, C. Colombo, A. Dalmau-Mallorqui, T. S. Sabaei and A. Fontcuberta i Morral, P. Krogstrup and J. Nygård, *Int. J. of Nanotech*, under review (2012)
I did the nanowire growth

Papers not referred to in the thesis:

XVI. Coherent X-ray nano-diffraction on single GaAs nanowires
J. Gulden, S. O. Mariager, A. P. Mancuso, O. M. Yefanov, J. Baltser, P. Krogstrup, J. Patommel, M. Burghammer, R. Feidenhans'l, and I. A. Vartanyants, *Phys. Status Solidi A* 208, 11 (2011)

XVII. Absolute dimensions of eclipsing binaries
J.V. Clausen, S. Fransen, H. Bruntt, E. H. Olsen, B. E. Helt, K. Gregersen, D. Juncher and P. Krogstrup**,** *A&A*, 516, A42 (2010)

* This paper is based on the work I did during my master thesis, but was published in the beginning of my PhD period. It will only be used as reference in this work.

[§] Equal contributors

List of symbols and abbreviations

MBE:	Molecular Beam Epitaxy
TEM:	Transmission Electron Microscopy
SEM:	Scanning Electron Microscopy
NW:	Nanowire
ML:	Monolayer
VLS:	Vapor-Liquid-Solid
ZB:	Zinc Blende
WZ:	Wurtzite
ERS:	Equilibrium reference state
TL:	Triple phase line
i :	Refers to the i'th element
j :	Refers to the j'th interface (unless other stated)
T :	Substrate temperature
$T_{b,i}$:	Beam flux temperature
$f_{i(,\perp)}$:	Beam flux in the direction of the beam ($\perp$ refers to the flux perpendicular to the given interface)
p_i :	Vapor pressure
$\rho_{j,i}$:	Density of adatoms
x_i :	Atomic fraction in the liquid phase $\bar{c}_{p,i}^{ERS}$
$\bar{c}_{p,i}$:	General symbol for the normalized atomic fraction in phase *p*
G_p :	Global Gibbs free energy of the *p* phase
g_p :	Gibbs free energy per atom in phase *p*
$\mu_{p,i}^{(\infty)}$:	Chemical potential in state *p* (∞ refers to infinitely large phases)
$\delta\mu_{p-ERS,i}$:	Chemical potential in phase *p* with respect to the *ERS*
$\Delta\mu_{pq,i} = \delta\mu_{p-ERS,i} - \delta\mu_{q-ERS,i}$:	Change in free energy due to a *p* to *q* atomic state transition
$\delta g_{pq,i}^{TS}$:	The activation free energy per *p* atom needed to reach the transition state between *p* and *q*
$\Gamma_{pq,i}$:	*p* to *q* state transition flux
$\Delta\Gamma_{pq,i}$:	The net flux of the *p* to *q* state transitions
$S_{b(v),i}$:	Sticking coefficient of beam or vapor elements
A_{pq} :	Area of the *pq* interface
$\lambda_{j,i}$:	The effective adatom diffusion length
$D_{j,i}$:	The effective diffusivity coefficient
$\tau_{j,i}$:	The mean lifetime in the adatom state
$\Xi_{pq,i}$:	Rate constant of the p to q transition
$\bar{Z}'_{pq}$:	The effective coordination number of the p to q transition. (') includes activation entropy.

$N_{p,i}$: Number of atoms of element *i* in phase *p*

$n_p^{(*)}$: Total number of III-V pairs in a cluster (* refers to the solid critical nucleus)

h_{ML} : Monolayer height along the growth axis

γ_j: The tension of the *j*'th interface

l_{TL}: Total length of the triple phase line

φ_j: The wetting angle given by Young's equation

$\theta(\omega)$: The angle between the *lv* and the *sl* interface at ω

ω: The angle between the middle of the side facet and the nucleation site, as measured from the center of the top-facet

χ: The fraction of the TL in contact with both the topfacet vertical sidefacets

I_{hkl}: The difference in interface energy between the hkl facet and maximum 'off facet' energy

Ω_p: The average atomic volume in phase *p*.

$I_i, I_{i,des}, I_{i,inc}$: The liquid sorption current, the liquid desorption current, the incorporation current

Z: The Zeldovich factor

A_n: Active step area of a 2D cluster of size *n*

σ: The ratio between *vs* and *ls* interfacial energies

w_{hkl}: Parameter specifying the half-width half maximum of the cusp in the gamma function around the (hkl) facet

c_{hkl}: Correction parameter at high w_{hkl} values

ξ: Contact angle of the constant curvature construction

θ: The angle from the topfacet to a given orientation

θ_T: Truncation angle defined as $\theta_T = 90 - \theta$

GR_{planar}: Corresponding planar growth rate

Δt: Time steps in simulation

t_{nuc}: Time since last nucleation event at the topfacet

t_{ax}: Growth time of the axial growth step

t_{rad}: Growth time of the radial growth step

Symbols introduced for the photovoltaic analysis

μ: Electron mobility

ρ_{eff}: The effective resistivity in a NW extracted from the four probe measurements

p_{eff}: The effective carrier concentration in a p-doped NW extracted from the four probe measurements

R_{res}: The resistance of the NW extracted from the four probe measurements

FF: Diode fill factor

I_{sc}: Short circuit current

V_{oc}: Open circuit voltage

V_{oc}^{macro} :	Open circuit voltage under a light concentration of 1 sun in a corresponding macroscopic device
η_{eff}^{macro} :	The solar cell efficiency in a corresponding macroscopic planar device under one sun
η_{eff}^{app} :	The apparent solar cell efficiency in a NW device under one sun
P_{sun} :	The incident solar power density, one sun
P_{macro} :	The effective light power density in a macroscopic device
P_{NW} :	The effective light power density inside the NW
A_{pj}^{app} :	Physical apparent projected cross section of a NW solar cell with respect to the incident light
A_{pn} :	Area of the pn junction
w :	Depletion width

Preface and Acknowledgement

This thesis is mainly based on the papers I have written as a first author during the last three years, but contains also brief summaries of few projects in which I have played a secondary role. The project is based on collaboration between University of Copenhagen and the spin-out solar cell company SunFlake A/S, which was supported by the Danish National Advanced Technology Foundation through project number 002-2009-1. It is concerned with the formation of III-V nanowires for photovoltaic applications and in particular the formation of GaAs solar cell nanowires on Si substrates using a solid source Molecular Beam Epitaxy (MBE). The vast majority of the nanowire growths which are characterized, analyzed and presented in this thesis are grown in the solid source Varian Gen II MBE system located at the Nano-Science Center, Niels Bohr Institute, University of Copenhagen.

The project began in September 2009 where the focus was on growing ordered arrays of InAs and GaAs nanoflakes on (001) orientated substrates. Ideally the ultimate goal was to grow ordered GaAs nanoflakes on Silicon substrates. After many initial and intense growth studies it became clear that controlling the growth of such nanostructures is far from being a straight forward task, and even though research on crystal growth has made huge progress recent years, the detailed growth mechanisms is still far from being understood in detail. In October 2009 I meet Hadas Shtrikman, Weizmann Institute, at the nanowire growth workshop in Paris where she told about some initial but very interesting studies on self-catalyzed GaAs nanowires she had grown on Silicon substrates. We agreed to cooperate on a detailed growth study which involved many growths carried out in the MBE systems in both Israel and Denmark. It turned out that this type of growth was very promising for photovoltaic applications and focus was from at that point turned towards this. However, still many challenges in terms of controlling the overall nanowire morphology and controlling the crystal structure were piling up. Thus, it was decided that the main focus of the research should be directed towards a better understanding of the fundamental mechanisms behind the crystal growth, with a secondary focus on the photovoltaic properties. I have been collaborating with many fantastic and talented people throughout the whole period of the project and trying to write meaningful and fair acknowledgements to all these people would increase the change of forgetting someone or some contributions. Thus, I will here just like to thank all the people I have been working together with during the last three years.

The thesis is primarily based on the papers I have written and been primary investigator on. I have also used few images/figures which I have not designed or taking myself, and this will mentioned by referring to the relevant person or paper. For the people who made significant and direct contributions to this thesis are acknowledged here;

I would first like to thank Frank Glas, CNRS, for the enlightening and helpful theoretical discussions on NW growth mechanisms and treatment and calculations of thermodynamical parameters. I have really learned a lot from these discussions and especially chapter 2 which is based on our paper [I] would not have been the same without these discussions. I'm also really grateful for all the time he has spend on the many drafts I sent him and the very useful comments he returned. I hope that we can continue our collaboration in the future.

Hadas Shtrikman is gratefully acknowledged for all the helpful discussions on NW growth conditions and tons of emails back and forth between us before submitting paper [II]. A significant portion of this thesis would not have happened without her. (Also thank for the great sightseeing trips in very fast and characteristic ‘Shtrikman step walking’ around Rome, Paris and Jerusalem.)

Claus. B. Sørensen is acknowledged for teaching me almost everything I know about the MBE system and for having an incredible source of knowledge about the epitaxy system. Without all the doping level and planar growth rate calibrations and maintenance of the MBE system this study would not have been possible.

I would like thank Henrik I. Jørgensen for a great collaboration on both experimental and theoretical projects. Especially introducing me to dynamical modeling methods in Mathcad and setting up a big part of the simulation programs was a great help for paper [I]. Also a big thank for the experimental collaboration on the positioned GaAs growth for paper [XI] and the I-V measurements from the optical lab presented in Figure 9-3.

Morten H. Madsen is acknowledged for being a close collaborator throughout the three years, right from NW growths to wafer preparations to discussions on growth kinetics ect. His great technical skills both in terms of software and hardware related issues have been very helpful in many situations. He is especially acknowledged for the common work on in-situ x-ray characterization on NW growth presented in paper [IV] and chapter 7, were he in particular played an important role on acquiring the data and doing the follow up TEM work at the microscope in the basement.

Martin Aagesen is the main reason why I got involved in this PhD project, for which I’m very grateful. It is not always a lot of time he have been able to spend on research because main focus has been on keeping SunFlake running, but discussions is always with enthusiasm and great optimism given inspiration in particular while writing papers [I] and [III].

Jeppe V. Holm, is acknowledged for all the experimental work done in optimization of contacts, etching rates, filler thickness ect. All this is very important contributions in papers [XI] and [XIII].

Jason Röhr is acknowledged for his great job on device fabrication and I-V characterization on a large part of the wires presented in paper [X] and Chapter 8.

Shivendra Upadhyay is acknowledged for some enlightening discussions on electrical properties of GaAs and InAs nanowires, which has improved the interpretation of the measurements presented in Chapter 8.

I would like to thank Robert Feidenhans'l, who has taught me a lot on x-ray diffraction and for starting up many interesting x-ray characterization studies on III-V nanowires. Especially the trips to Japan for in-situ characterization GaAs NW growths in a MBE chamber were very special, paper [IV]. But also the x-ray studies on single InAs nanowires in arrays at the synchrotron in Grenoble, was a very productive and fruitful study. These results will hopefully be published in the coming year.

Dominique Chatain and Stefano Curiotto, CNRS, Marseille, are acknowledged for all the things I learned about wetting behavior of liquids on solids and for introducing me to the software program Surface Evolver, paper [III]. Also a special thank to Stefano for helpful discussions on thermodynamics.

I would like to give a special thank to Anna Fontcuberta i Morral, for inviting me to Lausanne and including me in many fantastic projects (papers [VI],[VIII],[X],[XI],[XII],[XV]) and for giving me a lot of support throughout the entire process. I'm incredibly grateful for the opportunities this have giving me and for all the things I have learned from her. Her contribution to this thesis is enormous and in particular her contributions to chapter 8 and 9 are extremely important. Many researchers and students from her lab have played an active role in the work. Pierre Blanc is acknowledged for fabricating many of the single lying nanowire solar cell devices, which are presented in Chapter 9.1. Also thank to Carlo Colombo, who is acknowledged for his great experimental work on the p-i-n solar cells, which in my opinion has resulted in two great papers [XII] and [XIV]. Paper [XIV] is briefly discussed in section 9.4. Also thank for a lot of experimental support and for the nice times drinking beers and discussing physics during my stay in Lausanne. Martin Heiss is acknowledged for both his experimental and theoretical contributions in the paper [XI], which is discussed in Chapter 9.5, and for the quick replies on email when I try to understand optical resonances and photovoltaic properties in nanowires. The last person in Anna's lab who need a special thank is Alberto Casadei who I have been collaborated closely together with on paper [X]. Chapter 8 which concerns Be doping mechanisms is based on this work.

I would also like to give a special thank to Erik Johnson, my private supervisor or maybe 'support teacher' as he would call it. I deeply thank him for not only all the great and helpful discussions on thermodynamics, kinetics and for his fantastic TEM work (shown in Figure 1-4 and Figure 7-1), but also for the sincere interest he always have shown in my work and for all the things I have learned from him. Erik has in many ways played an active and important role in the research, which has resulted in the papers of NW growth mechanisms. I hope it will be possible to persuade him to stay in contact with research field and interact as often as possible after his retirement next year.

Finally, even though this project has not been a core subject of the nanowire transport group I still got regular and very helpful inputs from group leader Jesper Nygård. He has always been supporting and giving me the opportunity and freedom to go in directions I found interesting, which has been very important for the outcome of this project. I specially acknowledge the open minded approach towards the collaborations I have started with different groups and people around the world, which have ensured a continuous and dynamical process throughout the project.

At the end I would like thank my family deeply for without their patience, especially in the busy periods, this work would not have been possible.

Peter Krogstrup
Center for Quantum Devices & Nano-Science Center
Niels Bohr Institute, University of Copenhagen
Universitetsparken 5, 2100 Kbh. Ø, Denmark
E-mail: *krogstrup@fys.ku.dk*

1 Introduction

A nanowire (NW) is a crystal structure with a diameter constrained to tens of nanometers (typically 10^{-8} to 10^{-7} m) and an unconstrained length (typically 10^{-6} to 10^{-5} m). The finite lateral size gives rise to many interesting physical properties which are not seen in bulk materials, such as electron quantum confinement and optical resonances. Formation of NWs is typically achieved by depositing growth material onto a substrate at high temperatures in a vacuum chamber. The most typical III-V NW formation techniques are Metal Organic Chemical Vapor Deposition (MOCVD) and Molecular Beam Epitaxy (MBE). This work are primarily concerned with the growth of self-catalyzed GaAs NWs via the Vapor-Liquid-Solid (VLS) mechanism[1] in a Varian Gen-II solid source MBE system, which is sketched in Figure 1-1 (A).

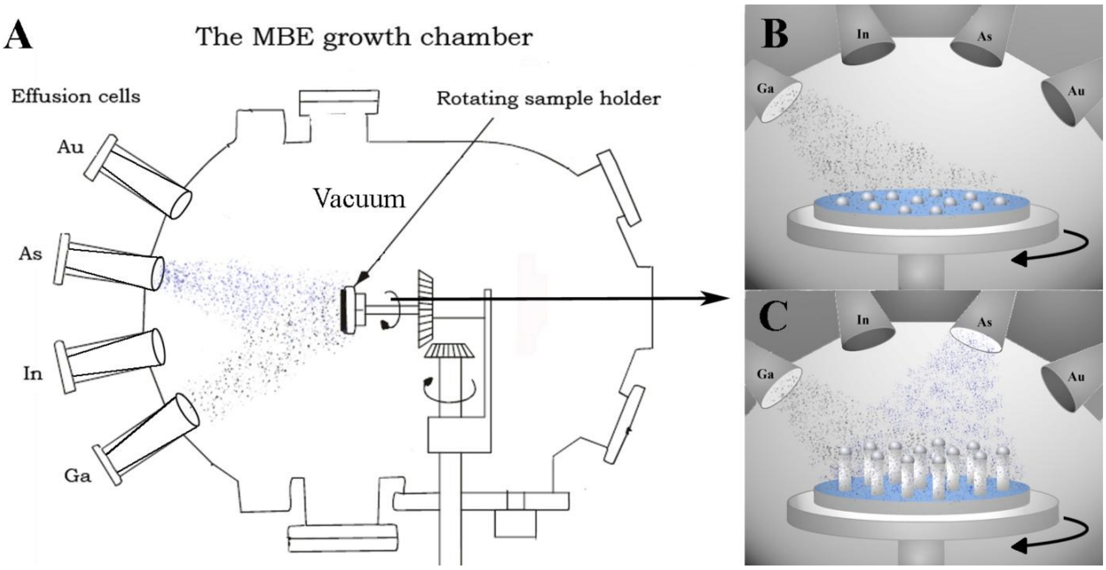

Figure 1-1. (A) A MBE growth chamber with four typical solid source effusion cells; Ga, In, As and Au. The relevant sources for a specific type of growth are heated up by a thermal heater which is wrapped around the effusion cells in order to get a flux of growth material (atoms/molecules) directed towards the substrate. (B) In the case of self-catalyzed growth of GaAs nanowires, first a beam of Ga atoms are used to form small liquid Ga droplets at the substrate surface. Hereafter is the shutter for the As valve opened (C), and the droplet acts as sorption centers for both the Ga and As elements. The droplets become supersaturated with As, which leads to solidification of GaAs at the liquid-solid interface and form the unidirectional NW growth.

A rough sketch of the NW growth is shown in Figure 1-1 (B) and (C). Most of the III-V semiconductor NWs are grown by the VLS process, in which a supersaturated liquid droplet initiates NW growth in the [111] direction of the stable cubic (C) zinc blende

(ZB) structure (ABCABC, 3C stacking) or in the equivalent [0001] direction of the hexagonal (H) metastable wurtzite (WZ) structure (ABAB, 2H stacking), see Figure 1-2. Higher order stacking sequences such as 4H (ABCB-ABCB) and others are possible but are occurring very rarely and only in small segments.

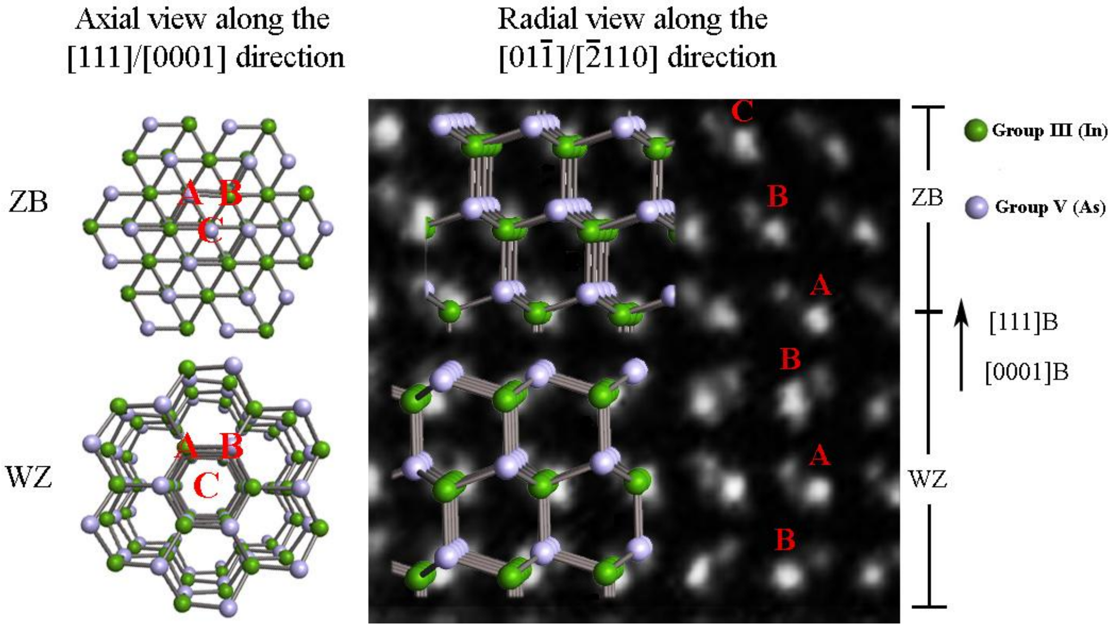

Figure 1-2. The two most common stacking sequences, ZB (ABC-ABC) and WZ (AB-AB), viewed along the axial $[111]/[0001]$ NW crystal growth directions and radial $[01\bar{1}]/[\bar{2}110]$ crystal directions. The background of the radial view is a STEM image of InAs NW taken from ref.[V]. STEM image is taken by Jun Yamasaki.

Characterization of the NW growth in terms of NW density, morphology and crystal structure are typically done with post growth electron microscopy techniques, such as Scanning Electron Microscopy (SEM), Transmission Electron Microscopy (TEM) and Scanning Transmission Electron Microscopy (STEM), see Figure 1-3.

Light reflectivity and absorption in semiconductor NWs depend on the energy of the incident light in a complex manner, since optical interference and wave guiding effects play a dominant role on the optical properties.

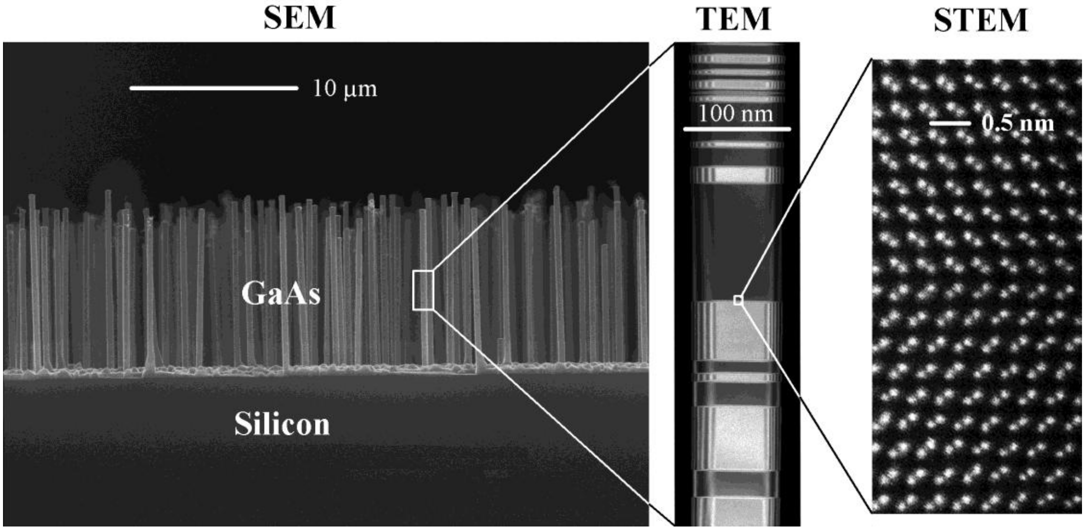

Figure 1-3. Post growth characterization of the NW growth is typically done with electron microscopy techniques. For characterization of the overall NW density and morphology, SEM is a fast and convenient way to get an overview of the growth result. The SEM image shown is a cross-sectional view on a cleaved Si (111) substrate with GaAs solar cell NWs (the same growth as the NWs characterized in section 9.2 and 9.4). The traditional TEM technique which can go one step up in resolution is also a relatively fast and convenient way to obtain information on a single NW morphology and crystal structure from an electron diffraction analysis. The contrast variation along the NW length seen in the image is due to a rotation in the ZB crystal structure around the growth axis, a so-called twin plane. This is seen in the atomic resolution in the high angle annular dark field STEM image. The STEM technique is sensitive to the atomic mass z as the measured intensity of the columns depends roughly on the mass as $z^{1.7}$. Even though the atomic masses are very close (z^{Ga}=31 and z^{As}=33) it is still possible to see a small difference in the intensity between the columns, see ref.[VI] for details. TEM and STEM images are taken by Erik Johnson.

III-V NW crystals are currently at the focus of attention due to their potential for applications in a variety of opto-electronic devices, such as photovoltaics, photo detectors, optical switches, ect. The potential prospects for possible applications of NW photovoltaic devices are still uncertain as the research in this area is at an early stage. However, the superior opto-electronic properties of GaAs materials such as efficient light absorption, ideal and direct bandgab and remarkable light concentrator efficiency, makes GaAs nanowire solar cells one of the most promising candidates for a future highly efficient solar cell solution. A problem related to the use of III-V's, is the high material cost which makes them unsuitable as large scale bulk solutions. Hence in order for them to be serious candidates as a future solution of solar cells with a competitive energy to cost ratio, it is necessary not only to grow the NWs on a relatively cheap substrate such as silicon, but maybe most importantly, it is also necessary to control the growth of the NWs. This is because the primary challenge in constructing an efficient

NW solar cell, lies within the abilities to form and control the NW growth, as the optical and electrical properties of NWs are determined by their crystal structure and overall morphology, which again are determined by the structure and morphology of the growth interface region[2,III,IV]. This is one of the reasons why it has been highly desirable to understand how the basic control parameters; temperature and beam fluxes, influence the NW formation.

The VLS growth mechanism that has been the standard model for decades was first proposed in 1964 by Wagner and Ellis as an explanation for unidirectional Si crystal growth in the presence of an Au droplet.[1] The typical diameters of the crystals (called whiskers) were at that time in the range 10^{-6} to 10^{-5} m. They concluded on the basis of a set of observations that the liquid phase acts as a sorption center for growth material arriving from the vapor phase, and that the whisker formation takes place by precipitation of growth material from the droplet. In the 1970's theoreticians lead by primarily Givargizov[3] proposed the first advanced growth models, where fundamental aspects of VLS growth, such as axial and radial growth rates, size effects, nucleation and diffusion phenomenon were discussed. It was not until the 1990's that controlled growth and systematic characterization of NWs were merging forward as the growth and characterization equipment was improving. In 1995, Hiruma et al.[4] presented a comprehensive work on growth of InAs and GaAs NWs with diameters down to 15-40 nm's, where they also presented measurements on the optical properties of GaAs NWs with photoluminescence spectra. This was one of the main papers which started an enormous interest in III-V NWs and therefore also in the NW growth mechanisms. The scene was now set for an intensive research in the formation of III-V NW crystals, in which the vast majority of NWs were catalyzed by Au droplets. Figure 1-4 (A) shows an example of a post-growth TEM image of a very thin GaAs NW crystal.

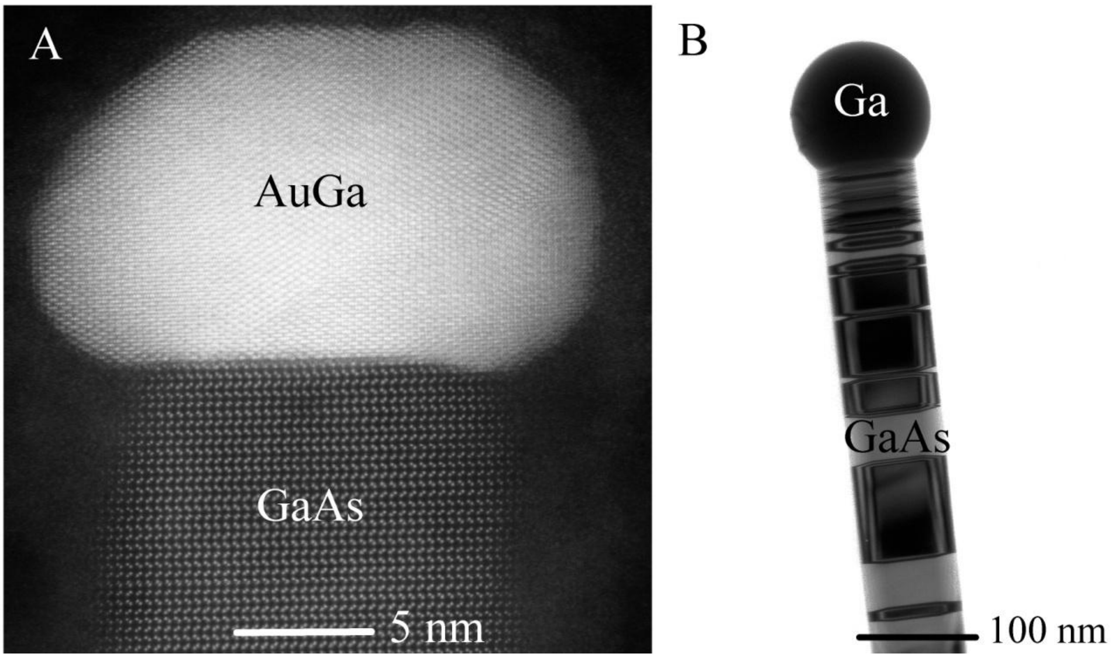

Figure 1-4. Two post growth images of the most common types of growth of GaAs NWs via the VLS mechanisms; (A) Au catalyzed and (B) self-catalyzed growth. (A) shows a thin GaAs NW with a solidified AuGa crystal cap. The image was acquired with the high angle annular dark field (STEM) technique, using the probe corrected TEAM0.5 microscope. This technique makes it possible to resolve the atomic columns of the dumbbells revealing a perfect As-terminated WZ structure. In (B) a relatively thick multiply twinned ZB structured GaAs NW with a liquid Ga droplet on top, is shown. This image is acquired with a 200keV CM20 microscope on film which is ideal for low magnification images with a large field of view. Both the AuGa and the Ga cap have been emptied of As upon cooling down to room temperature after growth termination. Electron micrographs are taken by Erik Johnson.

Even though many groups started to study the growth of III-V NWs, the VLS models from the 1970's where not significantly refined until Dubrovskii et al.[5,6,7] in 2004 and Johansson et al.[8] in 2005 proposed detailed VLS growth models of III-V NWs. These models were capable of describing new important details such as NW size effects and adatom collection, and many new models were to follow. It is today well accepted that a large fraction of the group III vapor material contributing to the axial growth of III-V NWs is adsorbed at the vapor-solid surfaces and diffuse to the growth region as adatoms. We should therefore in principle refer to it as the b(V)aLS growth mechanism, where 'b' and 'a' denotes the beam flux and adatom states respectively, but due to historical reasons we will keep the VLS abbreviation. The understanding of the complex growth mechanisms and experimental control of the crystal phases[9], morphology and many different kind of heterostructure growth have undergone a huge progress in recent years.[10,11] In spite of the progress, a unified description of the complex dynamic nature of nanostructure growth and in particular VLS growth is still far from being achieved.

Lately self-catalyzed growth of GaAs NWs (Figure 1-4 (B)) has become a hot topic[12], mainly because influence of Au on the optical and electronic properties is still ambiguous[13,14,15], but also because it has many other advantages, for example when growing on Si substrates.[II] Thus this material system seems to be an obvious choice for this project.

Chapters 2, 4 and 5 represent the work presented in Paper [I], with few modifications and additions from paper [III]. The primary focus in this thesis is on the growth mechanisms controlling crystal morphology and structure, since this is the essential part in obtaining optimized NW solar cells. Chapter 2 presents a proposal of a general theoretical framework which can be used to understand the evolution and mechanisms of the III-V NW growth and the influence of the basic growth parameters, temperature and incoming beam fluxes. Such a framework requires that the theoretical formalism is treated dynamically as all parameters depend on each other in a complex manner. Using the proposed framework, simulations of the overall NW growth morphology of self-catalyzed GaAs NW growth are shown and discussed and related to experiments in Chapter 4, whilst Chapter 5 goes into detail about the actual growth dynamics around the growth region. The formation of radial p-i-n core-shell GaAs NW solar cells is achieved through two different growth mechanisms, the p-core is formed via the VLS mechanism through a self-catalyzed growth mode[12] and the radially grown shell formation is carried out via a standard planar vapor-solid growth mode, discussed in the Chapter 6 (work which is only discussed in this thesis). Chapter 7 is based on results presented in papers [II] and [IV], where the structural formation probabilities seen in experiments are discussed briefly in the framework of the proposed theory presented in Chapter 2 and 4. In Chapter 8 which is based on paper [X], a qualitative treatment on the doping mechanisms during formation of the p-core is discussed and compared with a series of electrical measurements on NWs grown under different conditions. Finally a series of single NW solar cell experiments are performed and presented in Chapter 9.

2 Theoretical formalism for axial growth of III-V nanowires

The aim of this chapter is to construct a general formalism which can serve as a basic theoretical framework for analyzing a wide variety of important aspects of III-V NW growth, in terms of the basic growth parameters, temperature and beam fluxes. For this, the formalism is built on a dynamical framework with a special focus on the growth in a Molecular Beam Epitaxy (MBE) system. The formalism relies on an out of equilibrium treatment of the total state of Gibbs free energy, where the dynamical evolution of the system based on principles from transition state theory with detailed considerations of the kinetics and thermodynamics of the various states of matter. This chapter is directly based on the theoretical formalism for axial III-V nanowire growth via the VLS mechanism which will be presented in paper [I] with few modifications and additions from paper [III].

2.1 General theoretical formalism for III-V nanowire growth via the VLS mechanism

Describing crystal growth by MBE within a thermodynamic representation is not straightforward because the system is forced far away from equilibrium by applying different rates of thermal energy to the substrate and the evaporation cells. As the thermal equilibration time in the crystals is assumed to be much shorter than the characteristic time of crystal growth, the desorbed atoms or molecules takes part of a vapor phase which have temperatures irrespective of the energy of the incoming beams. This implies that there is a constant net flow of heat transferred from the beam fluxes to the reservoir (the NWs, substrate and substrate holder ect.). Thus the system is not in thermodynamic equilibrium and, in order to quantify the evolution of this complex system in terms of thermodynamic parameters, we need to refer to an equilibrium reference state (*ERS*). Such a global state refers to three classical phases, namely a solid, a liquid and a vapor with equal chemical potentials. The total Gibbs free energy and the Gibbs free energy per atom of a given phase p are denoted G_p and $g_p = \frac{G_p}{N_p}$, respectively, where N_p is the number of atoms in the phase. Changes in the total Gibbs free energy when an atom of group i (III or V) is removed at constant temperature and pressure will be the definition of the chemical potential, $\mu_{p,i} = \frac{\partial G_p}{\partial N_{p,i}}$. For the actual growth we will distinguish between five main types of states for each element i; beam flux (*b,i*), vapor (*v,i*), adatom/admolecule (*a,i*), liquid (*l,i*) and solid (*s,i*). The *b* and *v* states will be called the gas states and the *a*, *l* and *s* states condensed states.

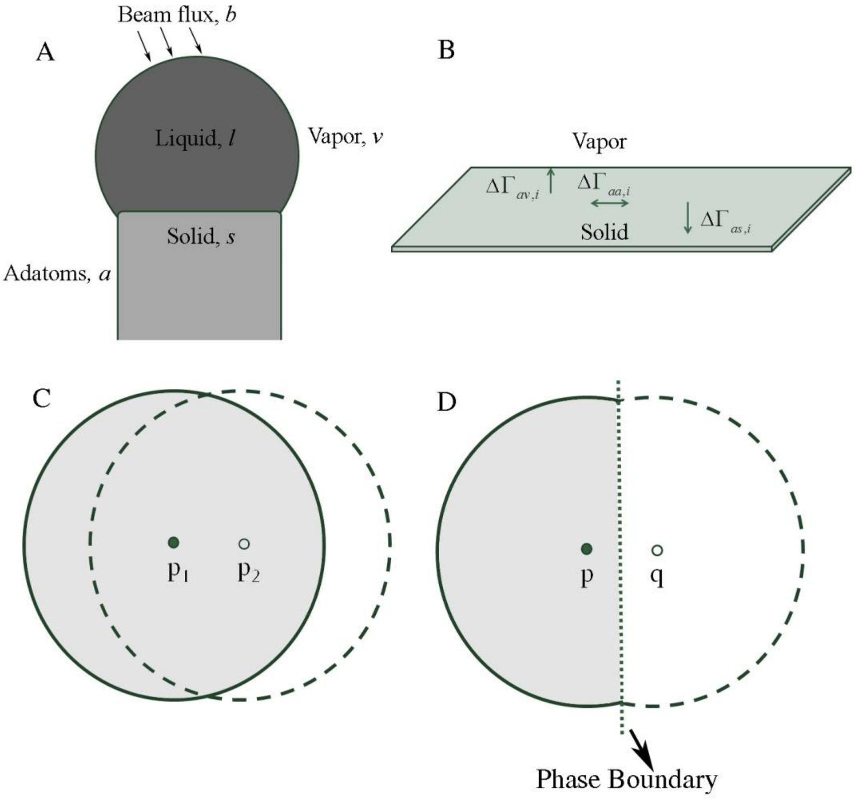

Figure 2-1. A) The five types of states considered during the NW growth process. B) An example of the processes which need to be considered for changes in an adatom microstate. The $\Delta\Gamma_{pq}$ term's symbolize the various net transition state fluxes from *p* to *q* states. C) The principle of describing atomic transition rates in a continuum language relies on the choice of small volume segments in the vicinity of the atomic state in which every property of the microstate takes on average values of such ensemble. Within one of the main states shown in A) two adjacent microstates are described with almost the same parameters. D) Between two distinct types of states we choose a Gibbs dividing interface where atomic microstates on each side of the phase boundary are described with mean parameters from a small volume segment within each respective main state. Thus in this formalism a discontinuous jump in the chemical potentials between two adjacent main states is possible during growth.

The *ERS* will be characterized by a corresponding set of intrinsic parameters, where all atoms of the same species have equal chemical potentials in each state. Because the solid III/V stoichiometry is considered to be fixed at 1:1, the chemical potential of the infinite solid phase is a function of temperature only and therefore serves as a natural reference for the *ERS*. To determine the global thermodynamic state of such a system it is convenient to choose the *ERS* temperature such that it equals the given growth temperature. This requires at least one degree of freedom. In the case of self-catalyzed growth, 4 intrinsic parameters are needed to describe the global *ERS* state; temperature T, liquid concentration x_V^{ERS} (group III concentration follows from $x_{III} + x_V = 1$) and partial vapor pressures p_{III}^{ERS}, p_V^{ERS}. Counting the number of constraints for the free energy equilibrium conditions gives three constraints; $\mu_{v,III} = \mu_{l,III}$, $\mu_{v,V} = \mu_{l,V}$ and $\mu_{l,III-V} = \mu_{s,III-V}$. Here $\mu_{p,III-V}$ refers to the chemical potential of a III-V pair, which is possible because the assumed fixed 1:1 solid stoichiometry. Hence, the *ERS* is entirely determined by the choice of one parameter, for instance the temperature. Moreover the corresponding adatom densities ρ_{III}, ρ_V will be estimated from the kinetic treatment presented below, under ERS conditions and additional constraints; $\mu_{a,III} = \mu_{l,III}$, $\mu_{a,V} = \mu_{l,V}$. This is consistent with the prediction that adatoms do exist at equilibrium at typical crystal growth temperatures[16]. For foreign element catalyzed growth there is one additional degree of freedom of the *ERS* description which means that both the temperature and say the group *III* atomic fraction in the liquid has to be fixed. Calculations of chemical potentials for III-V liquids including Au can be found in ref.[17]. The chemical potentials of the various states are measured with respect to the chemical potential of the *ERS,*

$$\delta\mu_{p-ERS,i} = \mu_{p,i} - \mu_i^{ERS} \tag{2.1}$$

where the definition of the *ERS* chemical potential is given as the liquid chemical potential of group III (or V) when the liquid and solid are in equilibrium

$$\mu_{III(V)}^{ERS}(T) \equiv \mu_{l,III(V)}^{\infty}(x_{III}^{ERS}(T), x_V^{ERS}(T)) = \mu_{s,III}^{\infty}(T) + \mu_{s,V}^{\infty}(T) - \mu_{l,V(III)}^{\infty}(x_{III}^{ERS}(T), x_V^{ERS}(T)) \tag{2.2}$$

Here $x_i^{ERS}(T)$ is the *ERS* mole fraction of group *i* in the liquid, and '∞' refers to large phases (i.e. without size effects, such as the Gibbs-Thomson effect). The change in the global Gibbs free energy when an atom is brought from a *p* to a *q* state is given by $\Delta\mu_{pq,i} = \delta\mu_{p-ERS.i} - \delta\mu_{q-ERS.i}$. To understand the mechanisms of atomic movement, we need to take a detailed look at the atomic/molecular state transition probabilities.

When the system is out of equilibrium, we allow for local variations of the intrinsic parameters. Within each of the main types of states (Figure 2-1A), a 'local state' *p* which depends on the spatial coordinates, will be characterized by the mean intrinsic properties of some local surrounding (the 'local ensemble') which is large enough to represent the thermodynamic characteristics and small enough to represent the local environment when the global system is out of equilibrium (Figure 2-1C). At interfaces between two main types of states, we choose a single Gibbs interface and distinguish between particles on each side of the interface with local state properties depending only on the local environment of the main state to which they belong (Figure 2-1D). An important aspect of this approach is that the rate at which a given single particle transition takes place is independent of the final state, i.e. the probability of a $p \to q$ state transition is independent of the *q* state. This probability depends according exponentially on the Gibbs free energy of activation as $P_{pq,i} \propto \exp\left(-\frac{\delta g_{pq,i}^{TS}}{k_B T}\right)$, consistent with transition state theory[18]. The activation energy $\delta g_{pq,i}^{TS}$ is taken as the difference in free energy per atom between the state *p* (calculated from the thermodynamic parameters describing the local environment) and the free energy of the state where an atom/molecule at position *p* is moved to the transition state between *p* and *q* (see Figure 2-2).

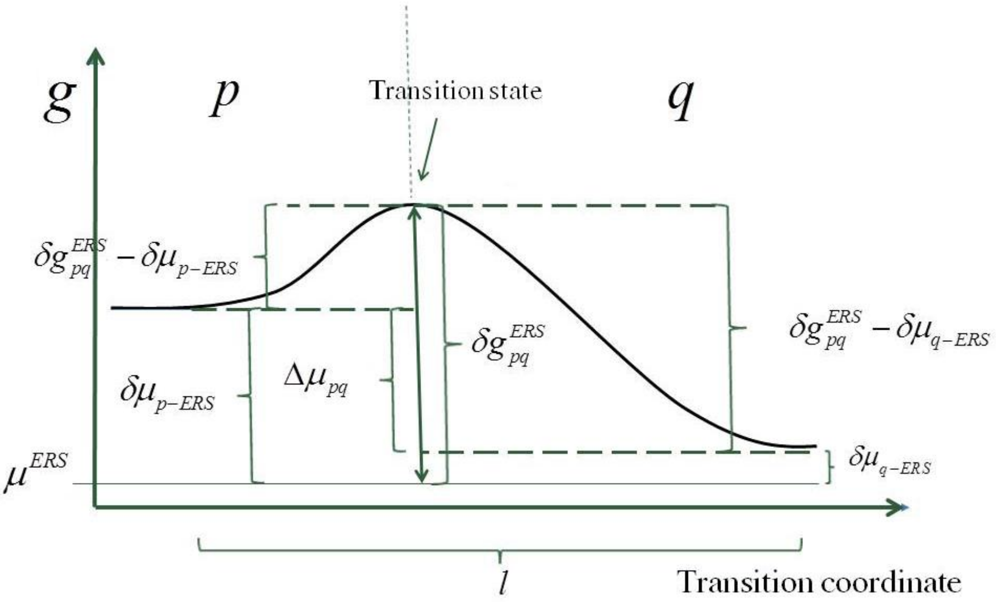

Figure 2-2. Conceptual one dimensional illustration of the free energy barrier associated with a *pq* state transition. Here the equilibrium state barrier is symmetric (i.e. $\delta g^{ERS,TS}_{pq,i} = \delta g^{ERS,TS}_{qp,i}$), as would be the case for a reversible state transition without requirements for dissociation/formation of bonds within a main state. The illustration is a typical atomistic view however it should seen in a continuum view as the free energies are based on mean parameter values of the local ensemble.

If a given transition requires a bond-dissociation of molecules into single atoms (e.g. $As_2 \rightarrow 2As$), the dissociation enthalpy and entropy should be added to $\delta g^{ERS,TS}_{pq,i}$. The activation free energy barrier for reaching the transition state *TS* can be written as, $\delta g^{TS}_{pq,i} = \delta g^{TS,ERS}_{pq,i} + \delta\mu_{p-ERS,i}$, where $\delta g^{TS,ERS}_{pq,i}$ is the activation free energy for an atom in a *ERS* state *p*, and $\delta\mu_{p-ERS,i}$ is the relative chemical potential with respect to the *ERS*. The flux of atoms in the state *p* crossing the *pq* boundary per unit area (or length) is given as,

$$\Gamma_{pq,i} = \begin{cases} \Xi_{pq,i}\bar{c}_{p,i} \exp\left(-\dfrac{\delta g^{TS,ERS}_{pq,i} - \delta\mu_{p-ERS,i}}{k_B T} \right) & if \quad \delta g^{TS,ERS}_{pq,i} \geq \delta\mu_{p-ERS,i} \\ \Xi_{pq,i}\bar{c}_{p,i} & if \quad \delta g^{TS,ERS}_{pq,i} \leq \delta\mu_{p-ERS,i} \end{cases} \tag{2.3}$$

where $\Xi_{pq,i}$ is a 'single atom flux' prefactor accounting for the number of attempts per atom to pass from the *p* state to the transition state per unit time and unit area. $\bar{c}_{p,i}$ is the normalized density of group *i* atoms in the sub-state *p*, i.e. the probability of having an atom in the state. When $\delta g_{pq,i}^{TS,ERS} < \delta\mu_{p-ERS,i}$, the transition is barrier free and, when $\delta g_{pq,i}^{TS,ERS} \cong 0$, thermodynamics only plays an important role when $\delta\mu_{p-ERS,i}$ becomes negative. The form of $\Xi_{pq,i}$ can be very different depending on the type of transition. The form of $\Xi_{pq,i}$ can be very different depending on the type of transition. In a simplified picture we can divide the transitions into two forms depending on whether the *p* state is a condensed or gaseous state. If the local *p* state is part of a condensed state the prefactor can be written as, $\Xi_{pq,i} = Z_{pq,i}\nu_{p,i}$, where $Z_{pq,i}$ is the steric factor[19] of the *p* to *q* transition per unit area and $\nu_{p,i}$ is a vibration frequency. For the gas states (beam flux or vapor), the prefactor can be written as, $\Xi_{b(v),i} = \dfrac{S_{b(v)q,i}\, f_{b(v),i}^{\perp}}{\bar{c}_{b(v),i}}$.

In order to calculate the effective flux across a *pq* boundary, the backward *q* to *p* flux needs to be subtracted from the forward *p* to *q* flux, $\Delta\Gamma_{pq,i} = \Gamma_{pq,i} - \Gamma_{qp,i}$. In the ERS, we assume a detailed balance, i.e. the fluxes of material across a boundary equal zero, $\Delta\Gamma_{pq,i}^{ERS} = 0$, which implies that

$$\Xi_{qp,i} = \Xi_{pq,i}\frac{\bar{c}_{p,i}^{ERS}}{\bar{c}_{q,i}^{ERS}}\exp\left(-\frac{\Delta g_{pq,i}^{TS,ERS}}{k_B T}\right) \tag{2.4}$$

with $\Delta g_{pq,i}^{TS,ERS} = \delta g_{pq,i}^{TS,ERS} - \delta g_{qp,i}^{TS,ERS}$ (Note that the exponential simply vanishes in the barrier free case). This is a general consequence of merging thermodynamics and transition state kinetics, where $\Delta\mu_{pq,i}^{ERS} = \delta\mu_{p-ERS} - \delta\mu_{q-ERS} \equiv 0$.[20] As the intrinsic parameters describing the *ERS* is defined from the equalities of the chemical potentials, eq.(2.4) provides an equilibrium relation between the ratios of coordination factors, attempt frequencies, possibly asymmetries for transition barriers and fixed compositions. Finally, using eq.(2.3) and eq.(2.4), the effective transition flux is given as:

$$\Delta\Gamma_{pq,i} = \Xi_{pq,i}\exp\left(-\frac{\delta g_{pq,i}^{TS,ERS}}{k_B T}\right)\left(\bar{c}_{p,i}\exp\left(\frac{\delta\mu_{p-ERS,i}}{k_B T}\right) - \frac{\bar{c}_{p,i}^{ERS}}{\bar{c}_{q,i}^{ERS}}\bar{c}_{q,i}\exp\left(\frac{\delta\mu_{q-ERS,i}}{k_B T}\right)\right) \tag{2.5}$$

As in eq.(2.3), if $\delta g_{pq,i}^{T,ERS} \le \delta\mu_{p-ERS,i}$, the exponential(s) vanish (i.e. $\exp\left(-\frac{\delta g_{pq,i}^{TS,ERS} - \delta\mu_{p-ERS,i}}{k_B T_p}\right) \equiv 1$). The entropy in the first exponential can be put into a new prefactor: $\Xi_{pq,i}^{'} = \Xi_{pq,i} \exp\left(\frac{\Delta s_{pq,i}^{TS,ERS}}{k_B}\right)$, and used as a temperature independent fitting parameter.[21]

To keep track of the atomic movements involved in the axial NW growth a continuity equation will be used to describe the atomic flow to and from the liquid phase,[II,IX]

$$\frac{d}{dt} N_l = I_{III}^{eff} + I_V^{eff} - I_{inc} \tag{2.6}$$

Here the effective liquid sorption currents I_i^{eff} of group i atoms,

$$I_i^{eff} = \int \Delta\Gamma_{al,i} dl_{TL} + \int \Delta\Gamma_{(vb)l,i} dA_{vl} \tag{2.7}$$

describes the effective 'adatom to liquid' and 'gas to liquid' currents. I_{inc} is the effective atomic incorporation current from the liquid into the solid, N_l is the number of atoms in the liquid, l_{TL} is the triple line (TL) length and A_{vl} is the liquid-vapor surface area, see ref.[22] for the effective *vl* area projected towards the beam. In eq.(2.7) the vapor and beam states have been merged into the same transition flux and eq.(2.5) for the gas-liquid transition as

$$\Delta\Gamma_{(vb)l,i} = \sum_n \frac{S_{v,i_n}}{\sqrt{2\pi m_{i_n} k_B T}} \left(p_{i_n} - \frac{x_i}{x_i^{ERS}} p_{i_n}^{ERS} \exp\left(\frac{\delta\mu_{l-ERS,i}}{k_B T}\right)\right) + S_{b,i}(\varphi, \hat{n}) f_{b,i,\perp} \tag{2.8}$$

where the sum runs over the different types of molecules carrying *n* atoms of group *i*. $S_{b,i}$ and S_{v,i_n} are the sticking coefficients of the beam and vapor phase, respectively. $S_{b,i}$ depends on the angle between the surface normal and direction of the impinging species and on the mean kinetic energy given by the temperature of the beam(vapor). Here it is assumed that $\delta g_{vl,i}^{TS,ERS} < \delta\mu_{v-ERS,i}$ and $\delta g_{bq,i}^{TS,ERS} < \delta\mu_{b-ERS,i}$.[23] A simple version (sufficient version in most cases) would be to assume unity sticking and a single vapor species, $\Delta\Gamma_{(vb)l,i} \cong f_{i,\perp} - \frac{x_i}{x_i^{ERS}} \frac{p_{i_n}^{ERS}}{\sqrt{2\pi m_{i_n} k_B T}} \exp\left(\frac{\delta\mu_{l-ERS,i}}{k_B T} \right)$ where $f_{i,\perp} = f_{b,i,\perp} + f_{v,i,\perp}$ is the effective impinging flux of group *i*. For typical growth conditions where $f_V > f_{III}$, the vapor pressure of group V can be assumed to be proportional to the incoming flux, $f_{v,V} \propto f_{b,V}$. This is because, if $f_V > f_{III}$, a huge contribution of the excess As species must come from secondary adsorption, and background pressure and be neglected.

Secondary adsorption of group III can typically be neglected, although for growth on substrates covered with a thermal oxide layer it can play a significant role. For the adatom to liquid transitions eq.(2.5) becomes:

$$\Delta\Gamma_{al,i} = \Xi_{la,i}^{'} \exp\left(-\frac{\delta h_{la,i}^{TS,ERS}}{k_B T} \right) \left(\frac{\bar{\rho}_i}{\bar{\rho}_i^{ERS}} x_i^{ERS} \exp\left(\frac{\delta\mu_{a-ERS,i}}{k_B T} \right) - x_i \exp\left(\frac{\delta\mu_{l-ERS,i}}{k_B T} \right) \right) \qquad (2.9)$$

where we have chosen to write it explicitly in terms of the *la* enthalpy barrier, because the atoms are presumably stronger bound in the liquid than in the adatom state. Consistent with the transition state approach the net sorption currents (eq.(2.7)) can be written as,

$$\begin{aligned} I_{(vb)l,i} &= \int \Delta\Gamma_{(vb)l,i} dA_{vl} = A_{vl} \left(f_{v,\perp} - \frac{x_i}{x_i^{ERS}} \frac{p_{i_n}^{ERS}}{\sqrt{2\pi m_{i_n} k_B T}} \exp\left(\frac{\delta\mu_{l-ERS,i}}{k_B T} \right) \right) + A_{vl}^{'} f_{b,i} \\ I_{al,i} &= \int \Delta\Gamma_{al,i} dA_{vl} = L_{TL} \Xi_{al,i} \left(\bar{\rho}_i - \bar{\rho}_i^{ERS} \frac{x_i}{x_i^{ERS}} \exp\left(\frac{\delta\mu_{l-ERS,i}}{k_B T} \right) \right) \end{aligned} \qquad (2.10)$$

In eq.(2.10) all information about the transition state barriers from the liquid to the vapor or adatom states are stored in the ERS parameters. Here only a given projection of the liquid surface $A_{vl}^{'}$ is exposed the incident beam flux (see ref.22 for details). L_{TL} is the length of the triple phase line.

The relative chemical potentials in the four main states are:

$$\delta\mu_{v-ERS,i}\left(p_i,T\right)=k_BT\ln\left(\frac{p_i}{p_i^{ERS}}\right) \tag{2.11}$$

$$\delta\mu_{a_j-ERS,III(V)}\left(\rho_{j,III},\rho_{j,V},T\right)=k_BT\ln\left(\frac{\bar{\rho}_{j,III(V)}\left(1-\bar{\rho}_{j,III}^{ERS}-\bar{\rho}_{j,V}^{ERS}\right)}{\bar{\rho}_{j,III(V)}^{ERS}\left(1-\bar{\rho}_{j,III}-\bar{\rho}_{j,V}\right)}\right)-\bar{Z}_{j,aa}\left(B_{j,III(V)}\left(\bar{\rho}_{j,III(V)}-\bar{\rho}_{j,III(V)}^{ERS}\right)+B_{j,III-V}\left(\bar{\rho}_{j,V(III)}-\bar{\rho}_{j,V(III)}^{ERS}\right)\right) \tag{2.12}$$

$$\delta\mu_{l-ERS,i}(x_{III},x_V,T)=\mu_{l,i}^{\infty}(x_{III},x_V,T)+\gamma_{vl}\frac{\partial A_{vl}}{\partial N_{l,i}}-\mu_i^{ERS} \tag{2.13}$$

$$\delta\mu_{s-ERS,III-V}^{X}=\sum_j\gamma_j\frac{\partial A_j}{\partial X}\frac{\partial X}{\partial N_{s,III-V}} \tag{2.14}$$

where $\rho_{j,i}$ and $\rho_{j,i}^{ERS}$ are the adatom densities on the *j*'th facet under actual and ERS conditions, respectively, and A_j and γ_j are the area and interface energy of the j 'th interface, respectively. The form of eq.(2.12) is derived from the partition function of a 2D binary mixture on an isomorphic substrate[24]. $\bar{Z}_{aa}$ is a reaction constant (including coordination number) of the facet j, and $B_{j,III(V)}$ and $B_{j,III-V}$ are the binding free energies for III-III(V-V) and III-V bonds on the j'th surface, respectively. Note that if a molecular bond of say an As_2 ad-dimer needs to be broken before forming a Ga-As bond the effective binding energy is lowered. Note also that as the surface is most likely reconstructed in a complex way depending on growth conditions and this should in principle also be taken into account on the values of $\bar{Z}_{aa}$, $B_{j,III(V)}$ and $B_{j,III-V}$. If the adatom concentrations and binding energies are predicted to be low, eq.(2.12) can be approximated with ideal behavior, $\delta\mu_{a_j-ERS,i}(\rho_{j,i},T)\cong k_BT\ln\left(\frac{\rho_{j,i}}{\rho_{j,i}^{ERS}}\right)$, which strongly reduces computation time in simulations. $\delta\mu_{v-ERS,i}\left(f_i,T\right)$ may be a negative quantity during growth in an MBE chamber as the cold walls act as sinks for the vapor. However it plays an important role for elements with high desorption rates[II,25]. The change in the Gibbs free energy when an atom is brought from a p to a q state is given by $\Delta\mu_{pq,i}=\delta\mu_{p-ERS.i}-\delta\mu_{q-ERS.i}$, and is a measure of the thermodynamical driving force for the transition. The relative solid chemical potential, eq.(2.14), in terms of the evolution of a given parameter, X (can be facets, angles or any other parameter describing the solid) is given by the change in the Gibbs free energy of the solid part of the growth system when $\partial N_{l,pair}$ III-V pairs have been brought from the liquid to the solid. $\delta\mu_{s-ERS,\,III-V}^{X}$ is only a size effect as the bulk chemical potential is the same as the *ERS*. In the continuum view, growth of a facet changes the areas of the facet and adjacent facets and therefore changes the energy of the system. If the solid was completely isotropic, the equilibrium shape would be with a curved *ls* interface, but in the anisotropic case which is the relevant case for III-V NW growth, the morphology is strongly faceted. This will be discussed in detail in section 2.3 and 5. In addition to interface size effects it was suggested by Schwartz and Tersoff[26] that the triple line energy, which may arise from an in-balance of capillary forces meeting at the TL, plays an important role on the dynamics of NW growth. They used the tangential component of the TL force on a locally smooth solid surface to describe the TL motion, and the normal component altering the solid chemical potential at the TL. In appendix E we include the effect of TL stress in the formalism using a slightly different approach.

2.2 Adatom collection

In the condensed regime the adatoms are bound to specific sites because the activation enthalpy of diffusion in all directions is larger than $k_B T$, which is the most typical regime. However even though it will not be considered here it might be possible that the activation enthalpy of diffusion in a given direction is smaller than $k_B T$ and that the adatoms therefore will move more or less freely with the characteristics of a one or two dimensional gas depending on the type of interface.

For the condensed adatom regime under quasi steady state conditions, it can be shown (using mass conservation) that the general equation for adatom collection can be written in a relatively compact form,

$$\Delta\Gamma_{al,i} = \frac{2\pi}{l_j} \sum_{r'=\frac{d_{NW}}{2}}^{\infty} r' \left(\Delta\Gamma_{(vb)a_{sub,r'}} - \Delta\Gamma_{a_{sub,r'}sub} \right) + \sum_{l=0}^{\frac{L_{NW}}{h_{ML}}} \left(\Delta\Gamma_{(vb)a_l,i} - \Delta\Gamma_{a_l s,i} \right) \qquad (2.15)$$

where the first summation accounts for the net transition flux from the substrate to the sidefacets and the second summation account for the net generation of adatoms along the NW sidewalls. $a_{a_{j,l}}$ is the adatom site at *r'*(*l*) along the *j*'th surface as measured from the NW root. l_j is the distance between the two adjacent adatom states. The substrate diffusion is assumed isotropic, which is a reasonable for growths carried out on substrates with a (111) orientation or substrates covered with an amorphous oxide layer. The summation can reasonably be replaced with an integral (if the adatoms are in the gaseous state both summations should be changed to integrals). Now because all adatom densities at all sites depends on each other, it has not been possible find a way to solve eq.(2.15). It needs to be solved numerically in a heavy iterative loop at every time step, using eq.(2.5) as constraints for the transition fluxes. Thus, for the modeling we decided to apply a less computational demanding approach and use a Fickian diffusion scheme with constrains consistent with the transition state kinetics.

But before going into the details with the adatom density calculations, we need to take a look at the adatom kinetics on a large homogenous planar interface. Since we in this case do not have to distinguish between the adatoms as all states are independent of position in the continuum approach we will just label all adatoms with a 'a'. The mean length displacement (i.e. the mean distance between 'birth' and 'death' positions, where 'death' is determined by either a '*as*' or '*av*' state transition) at such an interface is given by, $\lambda_{j,i} = \sqrt{D_{j,i}\tau_{j,i}}$, where $D_{j,i} = Z_{aa,i}\upsilon_{a,i}l_{j,i}{}^{2}(1-\bar{\rho}_{j,i})\exp\left(-\frac{\delta g_{aa,i}^{TS,ERS} - \delta\mu_{a-ERS,i}}{k_B T}\right)$ is the mean adatom diffusivity which depends on the dimensionality of the motion, and $\tau_{j,i} = \left(\tau_{j,i,as}^{-1} + \tau_{j,i,av}^{-1}\right)^{-1}$ the average adatom lifetime. Here $l_{j,i}$ is the distance between the two adjacent adatom 'sites' along the lowest energy direction(s) with activation free energy, $\delta g_{aa,i}^{TS}$. Higher energy directions are ruled out as less probable for simplicity. If an adatom occupies a given site, it is unlikely for another adatom to jump into the same site. Thus, the relative probability of jumping into a free site given by, $1-\bar{\rho}_{j,i}$, is included in the diffusivity with $\bar{\rho}_{j,i}$ being the normalized adatom density. The lifetimes ended by an '*as*' or '*av*' state transition are inversely proportional to the respective transition rates, $\tau_{j,i,as} = \frac{1}{\bar{Z}_{as,i}\bar{c}_{inc,i}\nu_{a,i}}\exp\left(\frac{\delta g_{as,i}^{TS,ERS} - \delta\mu_{a-ERS,i}}{k_B T}\right)$ and

$\tau_{j,i,av} = \frac{1}{\bar{Z}_{av,i}\nu_{a,i}} \exp\left(\frac{\delta g_{av,i}^{TS,ERS} - \delta\mu_{a-ERS,i}}{k_B T}\right)$, respectively. $\bar{c}_{inc,i}$ is the normalized density of probable incorporation sites (kinks or possibly steps at high densities and/or low temperatures) which is an important factor and illustrates the main difference between the nature of the *av* and *as* transitions, as desorption can take place everywhere. $\tau_{j,i,as}$ depend on the incorporation of both a group III and a group V because of the fixed 1:1 solid stoichiometry of III-V structures. For the modeling, $\tau_{j,i,as}$ is limited by incorporation of an adatom into a kink site, which means that the solid chemical potential equals the *ERS* state, and the nucleation events will not be considered explicitly. For desorption of adatoms the intrinsic activation barrier[27], $\delta g_{av,i}^{TS,ERS}$, is not related to the other component or to the state of the vapor.

The general equation for the adatom mean length displacement at a given point at the *j*'th interface is therefore given as,

$$\lambda_{j,i} = \sqrt{\bar{Z}_{aa,i} l_{a,i}^{2}\left(1-\bar{\rho}_{j,i}\right)\exp\left(-\frac{\delta g_{aa,i}^{TS,ERS}}{k_B T}\right)\left(\bar{Z}_{as,i}\bar{c}_{inc,i}\exp\left(-\frac{\delta g_{as,i}^{TS,ERS}}{k_B T}\right)+\bar{Z}_{av,i}\exp\left(-\frac{\delta g_{av,i}^{TS,ERS}}{k_B T}\right)\right)^{-1}}$$

(2.16)

which apparently is a chemical potential and vibration independent quantity. However the number of incorporation sites $\bar{c}_{inc,i}$ may depend strongly on the chemical potential and therefore on the local adatom densities of both components and on the orientation of the local facet. For the modeling it will be assumed that $\bar{c}_{inc,III(V)} \propto \exp\left(\frac{\delta\mu_{a-ERS,i}}{k_B T}\right)$, where proportionality as well as the respective entropy contributions are included in the prefactors $\bar{Z}'_{pq,i} = \bar{Z}_{pq,i}\exp\left(\frac{\Delta s_{pq.i}}{k_B T}\right)$. With this, eq.(2.16) can be estimated as

$$\lambda_{j,i}\left(\delta\mu_{a-ERS,i},T\right) = \sqrt{\bar{Z}'_{aa,i} l_{a,i}^{2}\exp\left(-\frac{\delta h_{aa,i}^{TS,ERS}}{k_B T}\right)\left(\bar{Z}'_{as,i}\exp\left(\frac{\delta\mu_{a-ERS,i}}{k_B T}\right)+\bar{Z}'_{av,i}\exp\left(-\frac{\delta h_{av,i}^{TS,ERS}}{k_B T}\right)\right)^{-1}}$$

(2.17)

Note that it is assumed that the activation enthalpy at the incorporation sites vanishes, $\delta h_{as,i}^{T,ERS} = 0$. An estimation of the different diffusion lengths are plotted in Figure 2-3, using the parameters given in Appendix B.

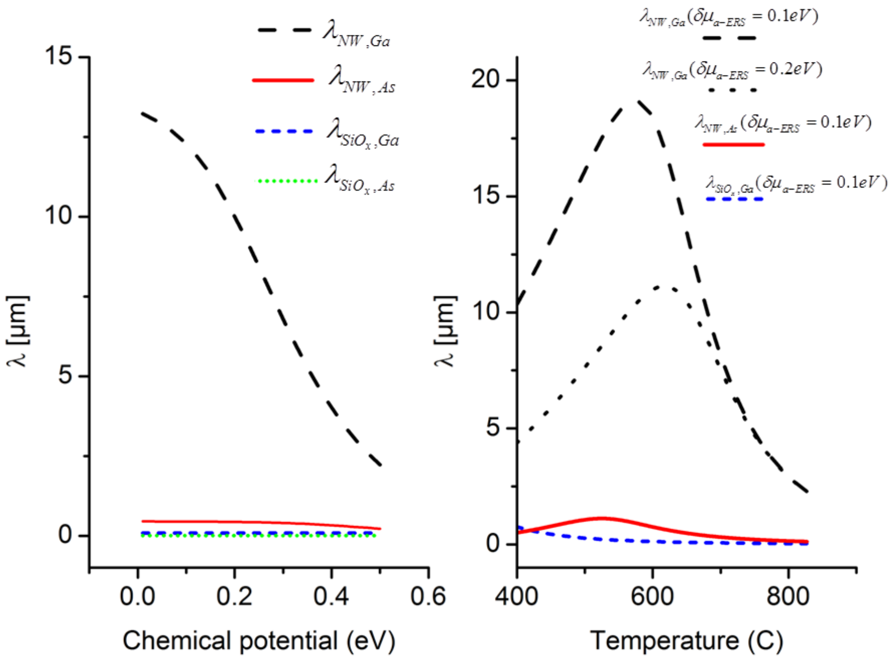

Figure 2-3. Diffusion length estimations for Ga and As on the NW sidefacets and thermal oxide at $T = 630°C$, using activation enthalpies listed in Appendix B. It is seen that on the oxide surface the diffusion length is independent of the chemical potential because it is in the desorption limited regime where the chemical potential does not play a role according to eq.(2.17). But a very strong dependence is seen on the sidefacet diffusion length for Ga adatoms on both temperature and chemical potential. At a fixed chemical potential it is seen in the plot on the right how the growth goes from being at the incorporation limited regime a low temperatures to a desorption limited regime at high temperatures. However the exact dependence and transition from the low to the high temperature regime depends strongly on how the chemical potential is influenced by a change in temperature.

Now to find the adatom densities $\rho_{j,i}$ at height z along the nanowire sidewall we will follow the approach proposed by Dubrovskii et al.[28] and Johansson et al.[29] only distinguish between two types of facets, the NW sidefacets (*NW*) and a planar substrate facet (*sub*). If we assume that; $1-\bar{\rho}_{j,i} \approx 1$, and that $\bar{c}_{inc,i}$ is a constant along the substrate and NW length, meaning that the diffusion lengths only varies with time and does not vary along a given facet, two coupled Fickian diffusion equations,

$D_{NW,i}\frac{d^2}{dz^2}\rho_{NW,i}(z)=D_{NW,i}\frac{\rho_{NW,i}(z)}{\lambda_{NW,i}^2}-f_{NW,i}-\Gamma_{sa(NW),i}-\Gamma_{va(NW),i}$ and $D_{sub,i}\frac{1}{r}\frac{d}{dr}\left(r\frac{d}{dr}\rho_{sub,i}(r)\right)=D_{sub,i}\frac{\rho_{sub,i}(r)}{\lambda_{sub,i}^2}-f_{sub,i}-\Gamma_{sa(sub),i}-\Gamma_{va(NW),i}$ need to be solved. If shadowing effects and other influence from other NWs on the substrate are ignored we can assume that $\left.\frac{d\rho_{sub,i}}{dr}\right|_{r\to\infty}=0$ and we can write the average incoming beam fluxes as $f_{NW,i}=\frac{f_i\sin(\varphi_i)}{\pi}$ and $f_{sub,i}=f_i\cos(\varphi_i)$. φ_i is the angle of the incoming beam of group *i* with respect to the substrate normal. $\frac{1}{\pi}$ is the fraction of the NW facets which is exposed to the beam which is perfectly consistent with the transition state approach where transitions are independent of the state they are moving into. Solutions are then of the form,

$$\rho_{NW,i}(z)=C_1\exp\left(\frac{z}{\lambda_{NW,i}}\right)+C_2\exp\left(-\frac{z}{\lambda_{NW,i}}\right)+\frac{\lambda_{NW,i}^2\left(\frac{f_i\sin(\varphi_i)}{\pi}+\Gamma_{sa,i}+\sum_n\Gamma_{va,i_n}\right)}{D_{NW,i}} \tag{2.18}$$

$$\rho_{sub,i}(z)=C_3K_{0,\frac{r}{\lambda_{NW,i}}}+\frac{\lambda_{sub,i}^2\left(f_i\cos(\varphi_i)+\Gamma_{sa,i}+\sum_n\Gamma_{va,i_n}\right)}{D_{sub,i}} \tag{2.19}$$

where $K_{h,x}$ is the modified Bessel function of order *h* evaluated at *x*. To solve for the constants (C_i) we need three boundary conditions;

$$D_{NW,i}\left.\frac{d\rho_{NW,i}}{dz}\right|_{z=L_{NW}}=\Delta\Gamma_{al,i} \tag{2.20}$$

$$D_{NW,i}\left.\frac{d\rho_{NW,i}}{dz}\right|_{z=0}=-D_{sub,i}\left.\frac{d\rho_{sub,i}}{dr}\right|_{r=\frac{d_{NW}}{2}} \tag{2.21}$$

$$\rho_{NW,i}(z=0)=\rho_{sub,i}\left(r=\frac{d_{NW}(z=0)}{2}\right) \tag{2.22}$$

Eq.(2.20) assumes quasi steady state growth, combining the adatom to adatom state transition flux at $z = L_{NW}$ with the effective adatom to liquid state transition flux, which is driven primarily by the thermodynamic driving force across the phase boundary.

Because the net flux (eq.(2.5)) for the *al* transition is given as

$$\Delta\Gamma_{al,i} = \Xi'_{la,i} \exp\left(-\frac{\delta h_{la,i}^{TS,ERS}}{k_B T}\right)\left(\frac{\bar{\rho}_{NW,i}(L_{NW})}{\bar{\rho}_{NW,i}^{ERS}} x_i^{ERS} \exp\left(\frac{\delta\mu_{a-ERS,i}}{k_B T}\right) - x_i \exp\left(\frac{\delta\mu_{l-ERS,i}}{k_B T}\right)\right),$$

$\rho_{NW,i}(L_{NW})$ needs to be isolated in eq.(2.18) before it is put into eq.(2.12). Using eq.(2.3) for $\Gamma_{sa,i}$ and $\Gamma_{va,i}$, with $c_{v,i} = \frac{p_i}{RT}$ (ideal gas), $\delta\mu_{a-ERS,i}$ (which depends on the adatom densities (eq.(2.12)) is solved numerically at every time step and before being put back into $\Delta\Gamma_{al,i}$. Detailed calculations are shown in Appendix A (section 11.1). Eq.(2.21) combines the effective transition fluxes at the NW root, whereas eq.(2.22) combines the adatom densities which require a continuous adatom density function across the substrate – nanowire interface, see Dubrovskii et al.[28] and Johansson et al.[29]. To save computation time, adatom diffusion of As can in a simplified approach be neglected as it is predicted to play a minor role on the collection.[30,31]

2.3 The Liquid-Solid phase transition

We will now turn to the actual crystal formation. In order to discuss the mechanisms determining the shape and crystal structure formation, a detailed formulation of the liquid-solid (*ls*) growth region needs to be addressed. As in ref.[III], the *ls* system will be divided into two main regimes, *I* and *II*;

Regime *I*: The TL stays in contact with the topfacet.

Regime *II*: The TL is not in contact with the topfacet or possibly only in the short time during a nucleation event at the topfacet.

The vast majority of literature on the nucleation at the topfacet has assumed ideal regime *I* where the *ls* interface is perfectly flat.[2,36,III] In ref.[III] we have used the software *Surface Evolver*[32] to calculate the equilibrium shape of a drop sitting on top of a hexagonal shaped facet (ideal *regime I*), and to see how the fraction of the TL in contact with side-facet and the contact angle depend on the relative size of the droplet and equilibrium wetting angle (ϕ), see Figure 2-4. There have recently been indications that this regime is dominant for Ga assisted GaAs NW growth under non steady state conditions where the liquid decreases significantly in size, such as immediately after closing the shutter of the group III source or upon during cool down where the nucleation barrier is lowered.[33]

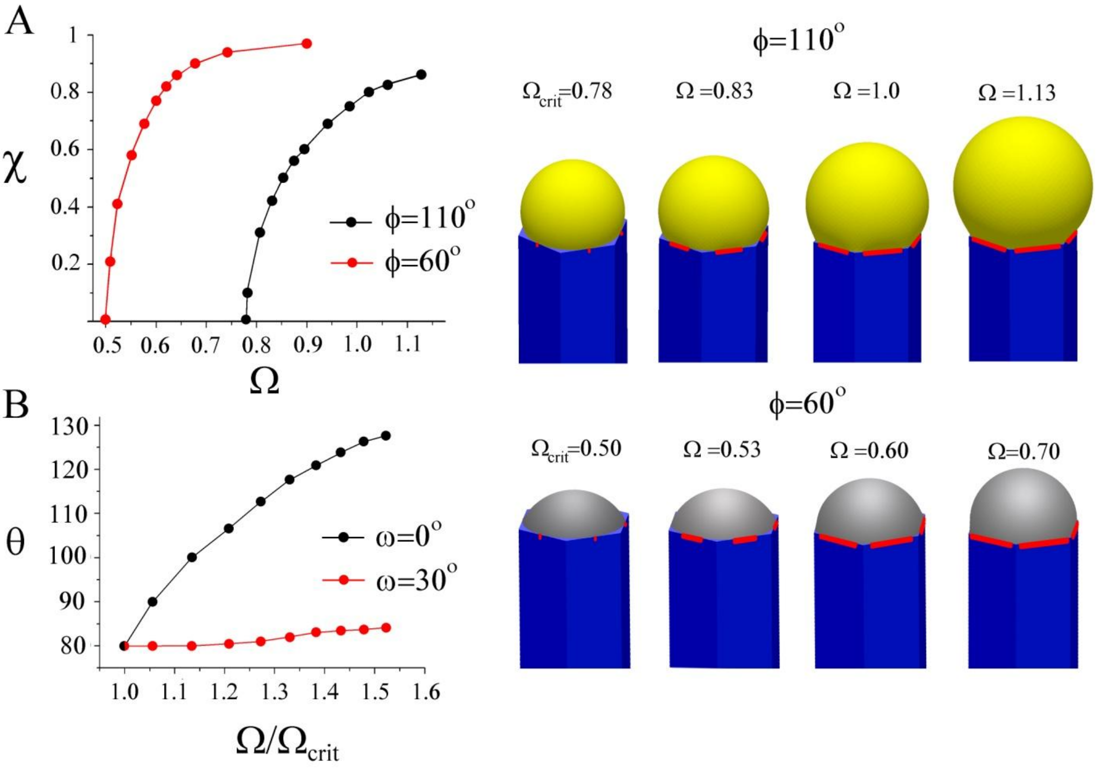

Figure 2-4. Equilibrium wetting of the topfacet under static regime *I* conditions. (A) The fraction χ of the TL at the growth interface edge as function of the dimensionless drop size Ω is shown in the case of two extremes, $\phi = 60^o$ (corresponding to liquid $Ga_{1-x}As_x$) and b) $\phi = 110^o$ (corresponding to an estimate for liquid Au). In the NW illustrations, the red line between the liquid and solid phases indicate the location where the TL is in direct contact with the NW side-facet. (B) The contact angle between droplet and top-facet as function of the droplet size at $\phi = 80^o$ is shown for the maximum and minimum values, $\omega = 0^o$ and $\omega = 30^o$, respectively. The system will move into regime II for large relative droplet sizes.

For a detailed analysis on the nucleation statistics under ideal regime *I* conditions in terms of the liquid wetting see ref.[III].

On the basis of recent reports on in-situ TEM experiments[38,39,40] and energy calculations presented in Chapter 5, regime *II* may be the dominant *VLS* steady state growth mode and we will therefore allow for the possibility of forming truncated facets at the edge of the topfacet. It is reasonable to assume that the liquid diffusivity is the same everywhere in the catalyst and that interface diffusion along the growth interface during VLS is negligible[34,V].

Growth of a faceted crystal can be described in terms of the evolution of a set of independent parameters $\{X\}$, which describes facet 'areas' or 'orientations'. For crystals which contain a certain set of low energy facets, it is enough to describe the facet growth in terms of only facet sizes (and therefore a parameter set $\{X\}$ of only 'areas'). The evolution of the crystal shape can be complicated by the fact that certain facets may be limited in their growth rate by the formation of a small nucleus. An additional complication for the dynamical evolution occurs if the solid is partially wetted by a droplet which at the same time is changing in size during growth. For such a system the preferential orientations of the facets depends on the droplet size and it is necessary to describe the crystal growth in terms of both facet sizes and facet orientations (and therefore a parameter set $\{X\}$ of both 'areas' and 'orientations'). For VLS growth we only consider growth at the *ls* interface and distinguish between two types of *ls* transitions:

Nucleation limited growth: Facets which are limited in their growth rate by the formation of a small nucleus, or limited in their change of orientation due to an energy barrier which is larger than the single pair transition state barrier.

Nucleation-free growth: Facets which are limited in their growth rate or in their change of orientation by the transfer of single pairs, as described by the transition state barrier.

Many studies suggest that the dominating type of growth at the topfacet is nucleation limited[40] while small truncation facets at the edges of the growth interface might be nucleation free or at least with a very small nucleation barrier[38]. We will therefore assume here that these transitions are nucleation free. The solid chemical potential depends on the stacking type *j* of the crystal structure {*j*: WZ(2H), ZB(3C), 4H, 6H, ect.}, with ZB and WZ being the most common sequences. The liquid to solid driving forces per III-V pair of large condensed phases are measured with respect to the ZB phase, $\Delta\mu^{\infty}_{ls,ZB}(x_{III},x_V,T)=\mu^{\infty}_{l,III}(x_{III},x_V,T)+\mu^{\infty}_{l,V}(x_{III},x_V,T)-\mu^{\infty}_{s,pair,ZB}(T)$, where $\mu^{\infty}_{s,pair,ZB}(T)=\mu^{\infty}_{l,III}(x^{ERS}_{III},x^{ERS}_{V},T)+\mu^{\infty}_{l,V}(x^{ERS}_{III},x^{ERS}_{V},T)$ is the solid chemical potential of a III-V pair in the bulk ZB phase. The driving force for solidification of a structural phase *j* such as WZ is typically smaller for large solid phases, $\Delta\mu^{\infty}_{ls,ZB}=\Delta\mu^{\infty}_{ls,j}+\Delta e_{coh}$, due to a difference in cohesive energy, Δe_{coh} (counted as positive). During growth the morphology of the *ls* growth system is continuously aiming to reach the lowest free energy configuration as the system is fed with excess free energy from the gas states and adatoms. However as the axial growth (growth at the (111) *ls* topfacet) is generally nucleation limited[35], it puts an extra limit on the ability to reach the lowest free energy configuration. As we will see in Chapter 5, there can be other barriers due to the solid anisotropy which can force the system even further from equilibrium. The liquid needs to reach a critical level of supersaturation (typically of the order of a few 100's of meV per III-V pair) before it can overcome the nucleation barrier at the topfacet. Under this constraint other facets which are not nucleation limited will reshape in respond to the elevated liquid chemical potential at a rate given by eq.(2.5), and the whole growth system is therefore in a configuration far from equilibrium. For *VLS* growth, group V is typically the limiting element since its concentration is low due to a low liquid solubility. The activation energy for the diffusion limited single pair *ls* transitions, eq.(2.5), can for a fixed solid stoichiometry be written as

$$\Delta\Gamma^{X}_{ls,III-V}=\Xi_{ls,III-V}\exp\left(-\frac{\delta g^{TS,ERS}_{ls,III-V}}{k_BT}\right)\left(x_V\exp\left(\frac{\delta\mu_{l-ERS,III-V}}{k_BT}\right)-x^{ERS}_{V}\exp\left(\frac{\delta\mu^{X}_{s-ERS,III-V}}{k_BT}\right)\right) \tag{2.23}$$

As $\delta\mu_{l-ERS,III-V}$ is an oscillating function due to the nucleation limited growth at the topfacet the parameter X (facet size or angle) will therefore oscillate in responds. Because the chemical potentials depend on location and system morphology, so do the transition fluxes, and the free energy minimization needs to be described with respect to an appropriate set of parameters, $\{X(\omega)\}$, which characterizes the growth system, such as facet size, angles and shape of the liquid phase ect. In three dimensions, the chosen set of parameters $\{X(\omega)\}$ will depend on ω which is the angle between the middle of the sidefacet and position as measured from the center of the top facet, see ref.[III] for clarification. The anisotropy of the NW crystals will be discussed below.

From eq.(2.14) the equilibrium shape of the growth system under given vapor and adatom chemical potentials can in principle be extracted by minimizing all driving forces

through a cyclic iteration process for all the chosen parameters until the they converge. We will assume that the timescale of NW growth is much larger than the characteristic time needed for the liquid to reach quasi steady state shape and composition. The shape of a NW is far from being an equilibrium crystal shape and it is therefore natural to consider the solid to be fixed after it has 'left' the growth system. Thus, we define a constant reference length z_{ref} which is measured from the (111) topfacet to a position beneath which the solid is considered fixed. As shown in Figure 2-5, it is sufficient to divide the crystal into 3 sections because the ZB crystal structure has 3-fold symmetry.

The WZ crystal structure has 6-fold symmetry along the growth axis and is therefore well described within this region. In table 1 (Appendix B), we show the most important and lowest interface energy directions of ZB and WZ structure for the upper half hemisphere centered around the (111) [0001] direction. To describe the NW diameter in terms of the cross sectional Wulff shape we need to look at the $\theta = 90°$ plane (the outer ring) in the stereographic projection in Figure 2-5 (A).

For a cross sectional six-fold symmetric NW it is enough to describe the NW diameter at the growth interface in the range $\omega = [-30° : 30°]$ as

$$d_{NW}(\omega) = \frac{d_{NW}(\omega = 0^\circ)}{\left(1 + \omega\eta(\omega)\right)\cos(\omega)} \tag{2.24}$$

where the function $\eta(\omega)$ determines the cross sectional shape of the growth interface. $\eta(\omega)$ depends on many factors and is a very complicated function to merge into the formalism. In a simplified approach it can be written as $\eta(\omega) = \eta_0\left(\cos^{-1}(\omega) - 1\right)\omega^{-1}$, where $\eta_0 = 0$ for complete hexagonal facetting and $\eta_0 = 1$ in the isotropic case (complete axi-symmetric cross section).

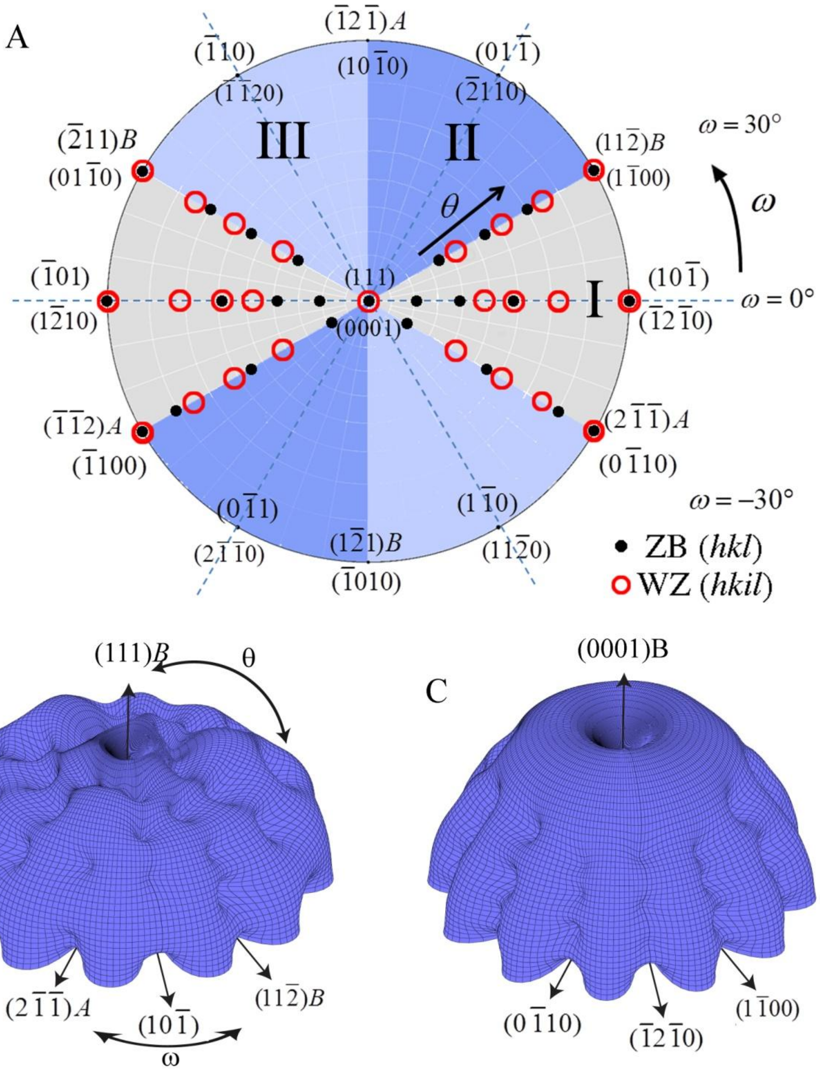

Figure 2-5. III-V NW crystal anisotropy for ZB and WZ structures. (A) A stereographic projection of the upper hemisphere along the [111] ([0001]) zone axis of a ZB (WZ) crystal. Due to the 3-fold symmetry of the ZB structure along (111), we only need to consider the grey areas, which are described in the range $\omega = [-30°;30°]$. The black dots represent the facets (hkl) with the lowest predicted energy of the ZB structure and the red rings represent the corresponding facets $(hkil)$ of the WZ structure. The edge of the projection represents the plane normal's perpendicular to the growth axis, $\theta = 90°$. Lower hemisphere orientations are found by mirroring the upper hemisphere orientations in the zone axis and change sign of the miller indices. The specific angles shown are given in Appendix B. 3D γ-plot function plotted in spherical coordinates (θ,ω) of the anisotropic *ls* interface energy for (B) ZB and (C) WZ structure using eq.(2.26) with the lowest miller index facets in the 12 directions between the (111) growth direction and {1-10} or {11-2} families (see Appendix B). The distance between origo and the surface is proportional to the interface energy of the given orientation.

In the case of especially ZB structure which has a three-fold symmetric crystal structure, it is very likely that the NW cross section does not have a perfect six-fold symmetric geometry. In this case we need to take account of the possibility of a three-fold symmetric cross section where the diameter is given by $d_{NW}(\omega) = r_+(\omega) + r_-(\omega)$ with $r_+(\omega)$ and $r_-(\omega) = r_+(\omega + 180°)$ being the radius as measured from the center of the NW crystal. For complete facetting $\eta_0 = 0$ and a constant NW volume the relation between r_- and r_+ is given by

$$r_+ = 2r_- - \sqrt{3r_-^{\,2} - 2\sqrt{3} \cdot A_{topfacet}} \qquad (2.25)$$

where $A_{topfacet}$ is the given cross sectional area of the topfacet. In the absence of a liquid phase the cross sectional equilibrium shape of the NW crystal would be given by $\frac{\gamma_A}{\gamma_B} = \frac{r_+}{r_-}$ according to Wulff, where $\gamma_A(\gamma_B)$ is the effective vertical surface energy of the facet normal to the $r_-(r_+)$ vector.

For a more complete description of the dynamics of the total *ls* growth system we need to know the anisotropic surface and interface energy functions for the different types of crystal structures. Differentiable functions are needed to model the dynamics of the free energy minimization process trough iterative processes. To do this we need a γ plot with rounded cusps that can approach arbitrarily close to the sharp cusps of faceted orientations. This can be done with a set of 2D Lorentzian functions around the facets with the high symmetry which have the lowest interface energies. The angular dependence of the interface energy is described in angular coordinates (θ, ω), by:

$$\gamma_{vs,j}(\theta, \omega) = \gamma_{vs0} - \sum_{hkl} c_{hkl} \frac{\mathrm{I}_{hkl}}{1 + \left(\frac{\phi_{hkl}(\theta, \omega)}{w_{hkl}} \right)^2} \qquad (2.26)$$

where $\phi_{hkl}(\theta, \omega) = \arccos\left(\cos(\theta - \theta_{hkl}) + \sin(\theta)\sin(\theta_{hkl})\left(\cos(\omega - \omega_{hkl}) - 1\right)\right)$ is the angle between the facet *hkl* (see table 1, in appendix) and the direction (θ, ω), where $\theta = 0$ corresponds to the growth direction (see Figure 2-5 (B) and (C) for ZB and WZ structure). The maximum interface energy is noted γ_{vs0}, and the decrease in interface energy at each facet is given by the ‘intensity’, $\mathrm{I}_{hkl} = \gamma_{vs0} - \gamma_{vs,j}$, where the most important values of $\gamma_{vs,j}$ can typically be found in the literature or can be estimated from density functional theory calculations. w_{hkl} is a scale parameter which specifies the half-width at half maximum of the energy increase around the (hkl) facet. c_{hkl} is a constant close to unity, but if w_{hkl} is large the interface energy may have to be adjusted to a value slightly lower than unity because the intensity from adjacent facets will pull the facet energies below the given facet energy. The liquid-solid surface energy is here simply given by $\gamma_{ls}(\theta,\omega) = \sigma\gamma_{vs}(\theta,\omega)$, where σ is a constant predicted to be of the order $0.3-0.5$.[36]

3 Nucleation limited axial growth and crystal structure formation

We now turn to the axial growth which takes place at the *ls* top facet. Many recent experimental studies have indicated that growth on the dominating *ls* 111(0001) top facet is limited by formation of a stable step, which means that the liquid supersaturation needs to exceed a certain critical value before the step and a new monolayer can be formed (see for example ref.[37],[38],[39],[40]). This is discussed in ref.[III] under regime *I* conditions, where it is argued that the nucleation probability for a given type of structure is dominated by the factor $\exp\left(-c\frac{\gamma_{ls,step}}{\Delta\mu_{ls,III-V}kT}\right)$, where c is a nucleus shape dependent constant and $\gamma_{ls,step}$ is the nucleus step energy. Due to the exponential factor, the total probability of nucleation is practically zero below a critical driving force $\Delta\mu_{ls,III-V}^{crit}=\delta\mu_{l-ERS,III-V}^{crit}-\delta\mu_{s-ERS,III-V}$ and increases sharply above, see Figure 3-1, which means that the driving force will oscillate around $\Delta\mu_{ls,III-V}^{crit}$ due to lowering of the liquid concentrations x_{III} and primarily x_V, upon forming each ML.

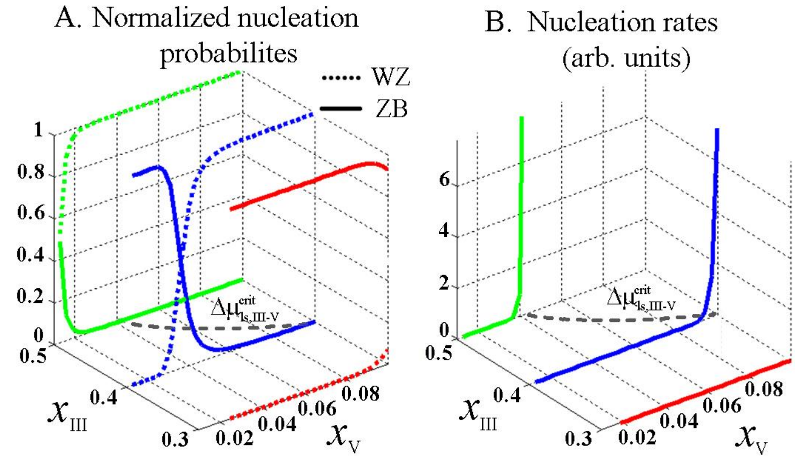

Figure 3-1. (A) Single nucleation site calculation in regime *I* of normalized ZB and WZ formation probabilities of Au-assisted GaAs NW growth. See ref.[III] for details on the calculations. (B) The total probability of a nucleation event is highly dependent on the liquid composition x_{III} and x_V, and thus nucleation with a $\Delta\mu_{ls,III-V}$ significantly different from $\Delta\mu_{ls,III-V}^{crit}$ (shown the $(c_{III},c_V,0)$ plane) is unlikely for a given *ls* morphology. In of both figures, $\Delta\mu_{ls,III-V}^{crit}=300$ meV/pair is chosen to illustrate the correlation between structural formation and probability of a nucleation event which is proportional to the nucleation rate. This figure is taken from ref.[III].

Because the volume of the mother phase (the liquid) is small and because the probability of having a second nucleation is impossible just after a first nucleation and the subsequent formation of a ML, we are only interested in single nucleation events. To describe the probability of forming a critical nucleus we need to take account of the stochastic nature of the phase fluctuations which causes nucleation. But first, we need an expression for the mean 2D nucleation rate $j(t_{nuc})$. Because the nucleation rate is an oscillating function with periods of ML formation,[37] it is convenient to measure the time t_{nuc} with respect to the last nucleation event. Assuming a large mother phase with constant supersaturation, $\delta\mu$, Kashchiev[41] showed in 1968, that the nucleation rate can be written in the form $j(t_{nuc}) = j^{st} f\left(t_{nuc}\right)$ where j^{st} represents the steady state nucleation rate (which will be treated below) and $f\left(t_{nuc}\right)$ is the correction accounting for a time-lag in the nucleation rate when going instantly from an under-saturated to a constant supersaturated mother phase at a given time $t_{nuc} = 0$. Because the distribution of clusters at the *ls* interface varies exponentially as a function of the liquid supersaturation[III] $\delta\mu_{l-ERS}$, it is reasonable to assume that there is a negligible amount of clusters just after a nucleation event. This mean that Kashchiev's time-lag factor is appropriate when describing nucleation phenomenon where the mother phase is of nanoscale size. Using the general formalism, Kashchiev's factor can be written as,

$$f\left(t_{nuc}\right) = 1 + 2\sum_{i=1}^{\infty}(-1)^i \exp\left(-i^2 \frac{\pi^2 Z^2 \Gamma_{ls,III-V} A_{n^*}}{16} t_{nuc}\right) \tag{3.1}$$

where Z is the Zeldovich factor[42] and A_{n^*} is the active step area of the critical nucleus with n^* pairs. Kashchiev's factor seems perfectly applicable to NW growth because $\delta\mu_{l-ERS}$ only drops by a small amount after a nucleation event and subsequent ML formation, whereas the probability of finding clusters of various sizes changes several orders of magnitude. The time-lag depends exponentially on the liquid to cluster attachment frequency $\Gamma_{ls,III-V}$ of the limiting growth species (typical group V) to the clusters. $\Gamma_{ls,III-V}$ is difficult to estimate because $\Xi_{ls,i}$ in eq.(2.3) is unknown. For the estimated value of $\Xi_{ls,i}$ used in the modeling shown in the next sections, we get

$f\left(t_{nuc}\right) \cong 1$ at the time of nucleation (so it will not be discussed further in the next sections). Put in another way, if the movement of atoms in and out of a given cluster (smaller than the critical nucleus) at the growth interface, takes place on a timescale much smaller than the time between each nucleation event, the nucleation probability can be derived assuming steady state conditions. However, it may play an important role for lower values of $\Xi_{ls,i}$ and especially at high growth rates, which will increase critical nucleation $\Delta\mu_{ls,III-V}^{crit}$ with increasing growth rate. Thus a change in $\Delta\mu_{ls,III-V}^{crit}$ may in principle also have an effect on the preferential structural phase formed (see Figure 3-1).

Now we need to find an expression for the 2D steady state nucleation rate j^{st}. For the modeling we will use the general classical expression for the nucleation rate at site (r,ω) at the topfacet, which is given as[43]: $j_{(r,\omega)}^{st} = Z_{(r,\omega)} c_1 \Gamma_{ls,III-V} \exp\left(-\frac{\Delta G_{n*}(r,\omega)}{k_B T}\right)$.

Here $Z_{(r,\omega)} = \frac{1}{n^*}\sqrt{\frac{\Delta G_{n*}(r,\omega)}{4\pi kT}}$ is the 2D Zeldovich factor and c_1 is the concentration of single III-V pairs attached to the interface (single pair clusters). $\Delta G_{n^*} = \sum_{i=2}^{n^*}\left(\delta\mu_{s_i-ERS,III-V} - \delta\mu_{l-ERS,III-V}\right)$ is formation free energy of the critical nucleus. With this, the mean nucleation rate at the topfacet can be written as:

$$j_{(r,\omega)}^{st} = A_{n^*} Z_{(r,\omega)} c_1 \Xi_{ls,III-V} x_V \exp\left(-\frac{\delta g_{ls,\text{int}}^{TS,ERS}}{k_B T}\right) \exp\left(-\frac{\Delta G_{n*}(r,\omega)}{k_B T}\right) \qquad (3.2)$$

where A_{n^*} is the step area of the critical nucleus of n^* pairs, $Z_{(r,\omega)} = \frac{1}{n^*}\sqrt{\frac{\Delta G_{n*}(r,\omega)}{4\pi kT}}$ is the 2D Zeldovich factor. The forward flux from the liquid to the solid is assumed independent of the solid state, $\Gamma_{ls,III-V}$. $\delta g_{ls,\text{int}}^{TS,ERS}$ is the single pair transition state barrier for attachment to the clusters at the interface (if any). If attachment to the clusters require dissolution or formation of molecular bonds apart from the ones in the nucleus it should be included in $\delta g_{ls,\text{int}}^{TS,ERS}$. However it will assumed that $\delta g_{ls,\text{int}}^{TS,ERS} < \delta\mu_{l-ERS,III-V}$, and therefore $\exp\left(-\frac{\delta g_{ls,\mathrm{int}}^{TS,ERS}}{k_B T}\right)\approx 1$. For a detailed derivation and discussion on the steady state nucleation rate using the general formulation as proposed in section 2.1, see appendix E.

Once the nucleation event has occurred, the ML is completed in a non-nucleation limited manner, at a rate given by eq.(2.5), and the liquid supersaturation builds up slowly again (in the timeframe of atomic movement in and out) until the next nucleation event takes place. It is assumed that the attachment/detachment frequency of III-V pairs to and from the clusters on the (111)B topfacet is limited by the group V elements. This is not only because the concentration of group V is low in the liquid but also because the group III elements are attached with only one covalent bond on average in the 'B' terminated surface when group V is absent. Once group V is present, the pair is stabilized leaving only one free covalent bond per pair on average (interface reconstruction phenomenon are left out in this continuum formalism).

The nucleus formation free energy of the nucleus, where *j* denotes stacking type (*ZB (3C), WZ (2H), 4H ect.*, see Johansson et al. [44] for a nice discussion on the various types of stacking sequences), can be written as in a more familiar form,

$$\Delta G_{n^*,j}\left(r,\omega\right)=-\Delta\mu_{ls,III-V,j}^{\infty}n^*+h\sum_{k=1}^{m}l_k\gamma_{step(r,\omega),k} \tag{3.3}$$

where the first term is the formation free energy required to form the volume part of the nucleus. The second term is the excess free energy due to the formation of a step. $\gamma_{step(r,\omega),k}$ and l_k are the free energy and length of the k 'th step facet, respectively. As the nucleation takes place when the number of pairs in the cluster exceeds the critical value, $n\geq n^*$, which is associated with the maximum free energy increase given by the condition,

$$\frac{d\Delta G_{n,j}}{dn}=-\Delta\mu_{ls,III-V,j}^{\infty}+h\sum_{k=1..m}\left(\frac{dl_k}{dn}\gamma_{step(r,\omega),k}+l_k\frac{d\gamma_{step(r,\omega),k}}{dn}\right)=0 \tag{3.4}$$

We can derive an explicit expression for the nucleation barrier ΔG_n^* by extracting n^* from eq.(3.4) (l_k depends on n^*) and insert it into eq.(3.3).

The term $\frac{d\gamma_{step(r,\omega),k}}{dn}$ is typically set to zero, even though it might play an important role for small nuclei.

For regime *II* we will divide all the different nucleation site possibilities at the *ls* topfacet into three main classes of nucleation sites, as shown in Figure 3-2.

A. Nucleation at the edge between the topfacet and truncated facet. Here the nucleus forms an extension to the truncated facet where the preferential crystal structure can be dictated by the truncation facet orientation with the lowest interface energy at the time of nucleation. Thus the preferred crystal structure formation at this site depends on the facet orientation.

B. Nucleation at the center of the topfacet. The preferential crystal structure here is the structure with the lowest cohesive energy which is typically ZB.[45]

C. If the relative droplet size is sufficiently small and/or the liquid supersaturation is sufficiently high at nucleation, it is possible that the truncation size becomes positive which will induce a TL nucleation event at the topfacet and the necessary step for step flow is formed. A fast completion of the monolayer will lower the supersaturation and move the truncation back to negative values. For a six-fold crystal geometry it is likely that such an event will take place at the corners, i.e. $\omega = 30°$. The preferential structure at TL nucleation is very likely the structure with the lowest sidefacet energy, typically WZ, as proposed by Glas et al.[2.] If the liquid size is decreasing TL nucleation becomes more and more dominant and the system will eventually move into regime *I*.

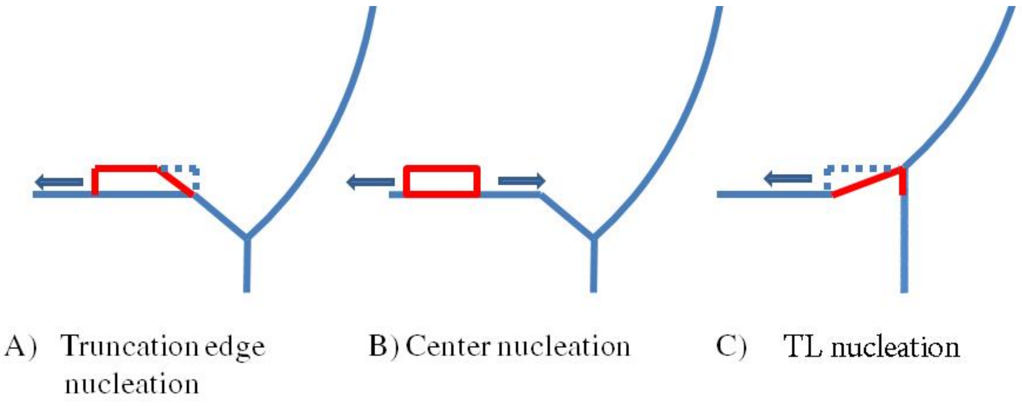

Figure 3-2. Cross section view on the triple line region at a given ω, showing three different ways to form an energetically favorable step on the topfacet. A) A step formed due to a nucleation event at the corner between the topfacet and a truncated facet, a regime II type nucleation. B) A step formed due to a nucleation event at the center of the top facet. C) If the relative droplet size is sufficiently small and/or the liquid supersaturation is sufficiently high at nucleation, it is possible that the truncation size becomes positive which will induce a TL nucleation event at the topfacet and the necessary step for step flow is formed.

Under conditions where the time taking to reach steady state composition in the liquid is smaller than the timescale between two consecutive ML formations, the total center-nucleation rate can be written as $J_c \cong 2\pi j_c \int_{Center} \left(\frac{d_{NW}(\omega)}{2} - \Delta z(\omega)\tan\left(\theta_T(\omega)\right) - l_m^* \right) d\omega$, where $\Delta z(\omega)\tan\left(\theta_T(\omega)\right)$ is the decrease in topfacet length at ω due to the truncation. For truncation edge nucleation we will integrate over the part with a negative truncation, $J_T \cong \pi \int_{l_T} l_m^*(\omega)\left(d_{NW}(\omega) - \Delta z(\omega)\tan\left(\theta_T(\omega)\right)\right) j_T(\omega) d\omega$. In order to carry out a more realistic modeling of the *j*-stacking probabilities we account for the stochastic nature of nucleation by multiplying the total nucleation rates by a random number between 0 and 1, $\Re(0,1)$, for every site x at the growth interface and at each time step Δt, and define a normalized value δ (taken as 0.5 in the modeling) above which nucleation will take place

$$\int_{Topfacet} j_{(r,\omega)} dA_{topfacet} \cdot \Delta t \cdot \Re(0,1) \geq \delta \tag{3.5}$$

Finally, all nucleation sites at the topfacet are checked at all time steps and whenever one or more sites fulfill eq.(3.5) the rate of the subsequent step flow and completion of a ML are determined by eq.(2.23). However it is possible that the truncation under certain conditions and at certain positions becomes positive before eq.(3.5) is fulfilled, see Figure 3-2 C. In this case a step is naturally provided at the TL and completion of a monolayer will take place at the same time as the truncation becomes negative again due to a lowering of the liquid supersaturation. As suggested by Glas et al.[2] if the first solidification event of a given (111) monolayer at the topfacet takes place in direct connection to the sidefacet, the structure of the whole monolayer is likely to maintain the structure of first solid formed. The most likely structure is the one with the lowest formation free energy, which can be different from the typical ZB structure if the nucleation takes place at the TL. However it is also possible to form WZ structure or other polytypes from truncation edge nucleation events, because of anisotropic truncation interface energies as discussed in the previous section.

4 Dynamical modeling of the overall morphology

In this chapter we will focus on modeling the overall NW growth morphology. This can be done without detailed considerations of the liquid-solid growth region, and therefore a flat liquid-solid topfacet and a constant liquid curvature will be assumed. This can be a convenient choice because the detailed modeling of the growth interface region is time demanding and does not seem to have a significant effect on the overall qualitative evolution of the NW growth. Before illustrating the applicability of the formalism it is important to mention that when modeling such a complicated system there are many unknown quantities involved, which are either gathered into temperature independent fitting parameters or just estimated. However, as many constraints are put on the system due to the huge amount of literature reporting on growth conditions, energies and so on, it is in principle possible to determine all fitting parameters to a reasonable extent, and it is hoped that more precise values of these parameters will become available in the future.

4.1 Calculating the ERS and size effects for Ga assisted GaAs nanowires in the axi-symmetric approximation

To simulate a specific growth process such as self-catalyzed GaAs NW growth on Si (111) substrates requires the relevant *ERS* parameters and size effects based on the assumptions made for the simulation. Thus, before carrying out detailed simulation examples of the overall NW growth we will here first go through the specific calculations needed for this system. As mentioned, modeling the overall morphology does not require detailed information of the shape of the *ls* interface, and in this section we will therefore assume an axi-symmetric cross section (ω dependence can be neglected) and an ideal regime *I* with a single flat *ls* interface. The parameter set describing the liquid-solid growth system in this section is therefore simply $\{X\} = \{d_{NW}, \theta\}$. The size effect terms in eq.(2.13) and (2.14) for the relative chemical potentials can be found using the trigonometric relations, $A_{ls} = \frac{\pi d_{NW}{}^2}{4}$,

$A_{vl}(\theta) = \dfrac{\pi d_{NW}{}^2 \left(1-\cos(\theta)\right)}{2\sin^2(\theta)}$ and $N_l(d_{NW},\theta) = \dfrac{\pi d_{NW}{}^3}{24\Omega_l}\dfrac{\left(1-\cos(\theta)\right)^2\left(2+\cos(\theta)\right)}{\sin^3(\theta)}$, where Ω_l is the atomic volume in the liquid. A change of d_{NW} implies not only a change in the *ls* and *vl* areas but also the formation of a new *vs* area corresponding to the absolute change in the *ls* area. For the overall morphology simulations we neglect the ω dependence on the system, which leads to an axi-symmetric (circular) cross section of the NW crystal. As discussed before, growth on the topfacet can be limited by formation of a step and nucleation will therefore be taken into account. We have for simplicity not taken account here of the possibility of wetting the sidefacets which is a possibility proposed by Dubrovskii et al.[46].

To calculate the chemical potentials of the *ERS* (eq.(2.2)), we need to calculate the liquid chemical potentials when the liquid phase is in equilibrium with the solid. For liquid binaries (self-assisted growth) we find the chemical potential from the intercepts of the tangent method, or correspondingly;

$$\mu_{l,i}^{\infty}\left(x_V,T\right) = g_l^{\infty}\left(x_V,T\right) + (1-x_i)\frac{\partial g_l^{\infty}\left(x_V,T\right)}{\partial x_i} \tag{4.1}$$

Here the liquid free energy per atom of an infinitely large binary alloy is given by, $g_l^{\infty}\left(x_V,T\right) = \left(1-x_V\right)g_{l,III}\left(T\right) + x_V g_{l,V}\left(T\right) + g_{l,mix}\left(x_V,T\right)$ where $g_{l,mix}(x_V,T) = \left(1-x_V\right)x_V\left[L_0(T) - L_1(T)\left(1-2x_V\right)\right] + RT\left[\left(1-x_V\right)\ln\left(1-x_V\right) + x_V\ln\left(x_V\right)\right]$ accounts for the asymmetry of compositional effect on the free energy by using the Redlich-Kister formalism[47] as in ref.[48] with two liquid interaction parameters L_0 and L_1. These parameters together with the free energy values of the pure components $g_{l,i}$ are given for $g_{Ga_{1-x_V}As_{x_V}}$ and $g_{In_{1-x_V}As_{x_V}}$ in Table 1, where the equilibrium concentrations are estimated from fitting the liquidus values reported in ref.[50]. All Gibbs free energies and chemical potentials are relative to the enthalpy of the standard element reference (HSER$_i$),[48] and denoted $g_l\,'(T)$ and $\mu_{l,i}\,'(T)$, respectively. Using these data, *ERS* chemical potential $\mu_i^{ERS}\,' = \mu_{l,i}^{\infty}\,'(x_V^{ERS},T)$ is calculated using eq.(4.1), and the relative chemical potential is $\delta\mu_{l,i}(x_V,T) = \mu_{l,i}\,'(x_V,T) - \mu_i^{ERS}\,'$.

To calculate the partial vapor pressures over a liquid of a given composition we note that $\mu_{v,i_n}{}'^{n} = n\mu_{l,i}{}'$ where n is the number of atoms in the molecule considered and $'^{n}$ denotes that the value is given with respect to n times the standard reference. Using the thermodynamic data from appendix 2 in *Ansara et al.*,[48] we find an expression for the Gibbs free energy of a pure i_n species, $g_{v,i_n}^{pure}{}'^{n}(T) = \Psi_i{}'^{n}(T) + RT\ln(P)$, where P is the total pressure and $\Psi_i{}'^{n}(T)$ is a function of temperature only (Table 2). Now because $\mu_{v,i_n}{}'^{n} - \mu_{v,i_n}^{pure}{}'^{n} = RT\ln\left(\frac{p_{i_n}}{P}\right)$, where $\mu_{v,i_n}^{pure}{}'^{n} = g_{v,i_n}^{pure}{}'^{n}$, it leads us to the following expression for the vapor pressure of element i_n,

$$p_{i_n}(x_V,T) = \exp\left(\frac{n\mu_{l,i}{}'(x_V,T) - \Psi_i{}'^{n}(T)}{RT}\right) \tag{4.2}$$

The corresponding ERS pressures are then found by setting the $\mu_{l,i}{}'(x_V,T) = \mu_i^{ERS}{}'$.

Liquid	$g_{Ga_{1-x_V}As_{x_V}} \quad \left[\frac{J}{mole}\right]$	$g_{In_{1-x_V}As_{x_V}} \quad \left[\frac{J}{mole}\right]$
$g_{l,III}{}'(T)$	$-1389.2 + 114.049T - 26.069299T\ln(T)$ $+1.0506\cdot10^{-4}T^2 - 4.0173\cdot10^{-8}T^3 - 118332T^{-1}$	$-3479.81 + 116.8358T - 27.4562T\ln(T)$ $+5.4607\cdot10^{-4}T^2 - 8.367\cdot10^{-8}T^3 - 211708T^{-1}$
$g_{l,V}{}'(T)$	$1.717245\cdot10^{4} + 99.78639T - 23.3144T\ln(T)$ $-0.00271613T^2 + 11600T^{-1}$	$1.717245\cdot10^{4} + 99.78639T - 23.3144T\ln(T)$ $-0.00271613T^2 + 11600T^{-1}$
$L_0(T)$	$-25503.6 - 4.3109\cdot T$	$-15851 - 11.27053\cdot T$
$L_1(T)$	-5174.7	-1219.5
$x_V^{ERS}(T)$	$6.752\cdot10^{-7}\exp(0.0141\cdot T)/100$	$(9.9\cdot10^{-4}\exp(0.00972\cdot T) - 0.3)/100$

Table 1. The coefficients of the free energy expressions of the pure elements in the case of InAs and GaAs are taken from the SGTE database[49], and are relative to the to the enthalpy of the standard element reference (HSER). The interaction parameters are taken from Ansara et. al.[48]. T is the (dimensionless) Kelvin temperature and all values are in Joule per mole. The equilibrium As mole fraction $x_{V,eq}$ is found from fitting liquidus values from ref.[[50]], in the range $T = 400 - 800^\circ C$ for ZB GaAs and $T = 350 - 550^\circ C$ for ZB InAs. All equilibrium data are found from experimental measurements and are relying on thermodynamical parameters which therefore should coexist in kinetic equilibrium.

Gas	$\Psi_i^{'n}(T)\ \left[\frac{J}{mole}\right]$
Ga	$263612.519 + 33.4871429T - 30.75007T\ln(T)$ $+ 0.00537745T^2 - 5.46534\cdot10^{-7}T^3 - 150942.65T^{-1}$
In	$237868.024 - 110.524313T - 8.405227\,T\ln T$ $- 0.0156847T^2 + 2.21196333\cdot10^{-6}T^3 - 110674.05T^{-1}$
As	$272027.85 - 32.2533338T - 21.21551T\ln T$ $+ 4.3891495\cdot10^{-4}T^2 - 7.393995\cdot10^{-8}T^3 + 9666.555\,T^{-1}$
As_2	$179351.548 + 10.5519715T - 37.35966\,T\ln T$ $- 5.61806\cdot10^{-5}T^2 - 2.13098\cdot10^{-8}T^3 + 104881.15T^{-1}$
As_4	$129731.745 + 230.754352T - 83.04465\,T\ln T$ $- 2.5148475\cdot10^{-5}T^2 + 1.0444733\cdot10^{-9}T^3 + 252728.45T^{-1}$

Table 2. Thermodynamic gas data taking from Ansara et al.[48], where $g_{v,i_n}^{pure\ 'n}(T) = \Psi_i^{'n}(T) + RT\ln(P)$, with P being the total vapor pressure in units of 0.1MPa. T is the (dimensionless) Kelvin temperature and all values are in Joule per mole.

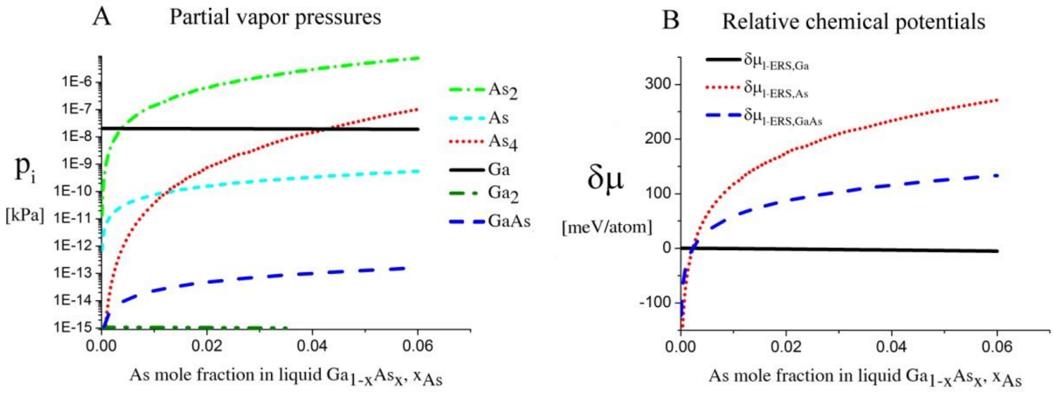

Figure 4-1. Partial vapor pressures and relative liquid chemical potentials of the relevant species in the liquid Ga-assisted GaAs case as a function of the As mole fraction at $T = 630°C$. (A) It is shown that as the liquid supersaturation increases (increasing x_{As}) the vapor pressure of Ga remains almost constant. This means that the *vl* and *al* transition fluxes for the Ga species are roughly independent of the supersaturation. On the other hand, as the supersaturation increases the desorption of the As species increase very strongly (note the log scale). This keeps the As concentration low in the liquid, and there exist a certain threshold value of beam flux/vapor pressure where the steady state concentration of As in the liquid exceeds the critical value for nucleation at the topfacet. The critical value $\delta\mu_{l-ERS,III-V}^{c}$ is typically of the order 100meV per atom which corresponds to few percent of As in the liquid as shown in (B).

From Figure 4-1A we see that the only species that may have significant partial pressures are the Ga and As_2 species. If we assume; $S_{b,Ga(As_2)}(\varphi,\hat{n},T_{b,Ga(As_2)}) \cong S_{v,Ga(As_2)}$, the incoming flux from the gas states under ERS conditions are given as; $f^{ERS}_{As_2,\perp} = 0.515\cdot 10^{17} m^{-2}\cdot s^{-1}$ and $f^{ERS}_{Ga,\perp} = 2.14\cdot 10^{17} m^{-2}\cdot s^{-1}$, at $T = 630°C$. To complete the *ERS* description we need to calculate the adatom densities, $\rho^{ERS}_{NW,i}$ and $\rho^{ERS}_{sub,i}$, which we do by using kinetics. For the adatom collection we follow the approach outlined in Appendix A, and the ERS adatom densities are found using eq.(10.1) under ERS conditions, where $\rho^{ERS}_{NW,i}$ and $\rho^{ERS}_{sub,i}$ is calculated by setting all chemical potentials to zero and $\Delta\Gamma_{al,i} \rightarrow 0$, both under conditions of the calculated *ERS* beam fluxes found above. Using the parameters listed in appendix B, *ERS* adatoms densities give, $\rho^{ERS}_{NW,Ga}\left(T = 630°C\right) = 5.3\cdot 10^{17} m^{-2}$ and $\rho^{ERS}_{NW,As}\left(T = 630°C\right) = 0.16\cdot 10^{17} m^{-2}$.

Tuning the fitting parameters can be time demanding. The fitting values of the relevant prefactors and activation free energies for adatom desorption and incorporation are given in appendix B. In order to make use of the diffusion length concept given by eq.(2.16) we need estimates of the activation energies $\Delta g^{TS,ERS}_{pq,i} = \Delta h^{TS,ERS}_{pq,i} - T\Delta s^{TS,ERS}_{pq,i}$ which are involved in the expression. As the entropy change as a function of temperature is negligible compared to the enthalpy term we include the entropy contribution into the temperature independent prefactors as $\bar{Z}'_{as,i} = \bar{Z}_{as,i}\exp\left(\frac{\Delta S^{ERS}_{pq,i}}{k_B}\right)$. This leaves us with enthalpy barriers which can be estimated from zero temperature ab initio calculations such as Density Functional Theory methods.[69] After having built up the simulation framework it can be used to analyze a variety of features and systems. Here, we will only give a few examples.

4.2 Dynamics of self catalyzed GaAs NW growth on Si(111) at low As fluxes

For typical *MBE* growth of self-assisted GaAs NWs on a Si (111) covered with a thin native SiO_x layer, Ga beam fluxes corresponding to planar growth rates of $0.1-0.3\frac{\mu m}{hr}$ are commonly used with a V/III flux ratio in the range $5-100$ and a substrate temperature around $T=630^{\circ}C$ [II,VI,VIII]. There exists a certain "growth parameter window" namely ranges of values for the basic growth parameters (temperature and beam fluxes), where it is possible to obtain NW growth. This depends on the type of wafer and the type of oxide layer.[VII] However, a general feature of the simulations is that there are sharp and well defined boundaries for the growth parameter window.
As the critical liquid supersaturation needed for nucleation at the topfacet is almost independent of the applied beam fluxes[III], the axial growth rate is simply dictated by the time it takes for the liquid to reach the critical concentration of As, $\delta\mu_{l-ERS,As}^{crit}$, after being lowered upon a nucleation event and subsequent ML formation.

If we neglect for simplicity the surface diffusion of As species and account for the impinging *v* states by simply using that the beam flux hits the total vl interface, the minimum As flux needed to obtain growth is roughly given as,

$$f_{vl,As,\perp}^{crit} \approx \frac{x_{As}^{crit}}{x_{As}^{ERS}} f_{lv,As}^{ERS} \exp\left(\frac{\delta\mu_{l-ERS,As}^{crit}}{k_B T}\right) \qquad (4.3)$$

Here x_{As}^{crit} is the critical concentration of As needed for a nucleation event and $f_{lv,As}^{ERS} \approx \sum_n \frac{p_{As_n}^{ERS}}{\sqrt{2\pi m_{As_n} k_B T}}$ is the flux of material evaporating from the liquid under *ERS* conditions. This means that the critical As flux is strongly dependent on the nucleation barrier and is only very little dependent on the Ga flux as long as there is a large liquid Ga phase. For the simulation shown in Figure 4-2 (A), the critical impinging As flux needed to overcome the nucleation barrier is roughly $f_{(bv)l,As,\perp}^{crit} \approx 100 \cdot f_{lv,As}^{ERS}$.

To examine how the axial growth rate depends on the incoming fluxes, we need to look at the time it takes to refill the liquid phase after a ML formation in order to recover the critical level. The outgoing *lv* flux of As depends roughly on the liquid chemical potential as $\Gamma_{lv} \propto \left(\frac{x_{As}}{x_{As}^{ERS}} \right)^2$ (because $\delta\mu_{l-ERS,i}$ depends roughly on the As concentration as $\ln\left(\frac{x_{As}}{x_{As}^{ERS}} \right)$, see eq.(2.10)). Now, because a relative small (large) droplet size will lead to a large (small) decrease in the As concentration immediately after a ML formation, means that the time taking to fill up the liquid to the critical concentration depends on the relative droplet size. Thus, especially in the limits of the growth parameter window where the relative droplet size is changing with growth time, the incoming fluxes of Ga may also play an important role on the growth rate.

In Figure 4-2 it is seen that the droplet size increase at low V/III ratios, but as the V/III ratio is increased the expansion of the droplet slows down as the grow increase and Ga is taken faster into the NW. For moderate V/III ratios where the droplet stays in a steady state regime the growth rate becomes more or less linearly with the As flux until it reach a limit where the droplet gets small and eventually gets consumed. The apparent linear relation between NW length and As flux at moderate V/III ratios is consistent with previous reports[51]. At very high incoming As fluxes, As just consumes the droplet and NW growth stops.

To start the simulation we need to know the initial condition. To estimate this the initial contact angle and liquid size in the case of self-catalyzed GaAs, post SEM images (Figure 4-3 (A)) was taken of a growth where Ga was deposited on a Si(111) wafer with the a native oxide layer at the same initial conditions as before a typical NW growth (here 1 min of Ga pre-deposition) without opening the valve to the As cell. In Figure 4-3 (B) a 6 min simulation show an example of the huge change in morphology when changing the As_2 flux around the lower limit of the growth window.

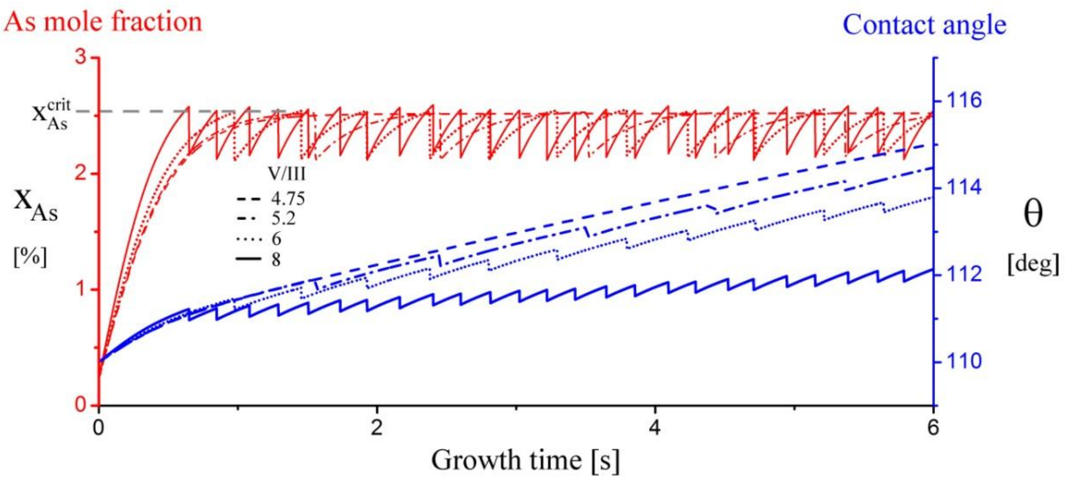

Figure 4-2. Initial transitory stage for the self-catalyzed growth of GaAs NWs on Si(111) at $T = 630°C$ using a Ga flux equivalent to a planar growth rate of $GR_{planar} = 0.3\frac{\mu m}{hr}$. The initial contact angle and NW diameter were set to $\theta_{initial} = 110°$ and $d_{NW,0} = 50\,nm$, and the time step was set to 0.001 sec. The As molar fraction in the $Ga_{1-x}As_x$ liquid phase and contact angle just after opening the As shutter, are shown for four different V/III ratios close to the lower limit of the growth window. A fast drop in the curve corresponds to a nucleation event and the formation of one monolayer at the topfacet (for V/III=4.75 it takes about 10 sec before the first nucleation event takes place and for lower V/III ratios it becomes impossible overcome the nucleation barrier). This event lowers the liquid chemical potential $\delta\mu_{l-ERS,As}$ and $\Delta\Gamma_{vl,As}$ and $\Delta\Gamma_{al,As}$ immediately increase and forces the As molar fraction back to a level sufficient to overcome the nucleation barrier again.

However, when growing the same type of wires on a patterned substrate with a thicker thermal oxide layer, the Ga flux needs to be equivalent to a planar growth rate of $0.8-1.2\frac{\mu m}{hr}$ and the V/III flux ratios need to be in the range 1-5.[52] This is a much higher Ga flux than for growth on untreated substrates with native oxide and is an indication that the *av* transition rate from the thick thermally grown oxide layer is dominant for the adatom state, as also predicted in Figure 2-3. This is an indication that the *av* transition rate from the oxide surface is dominant for these adatom states.

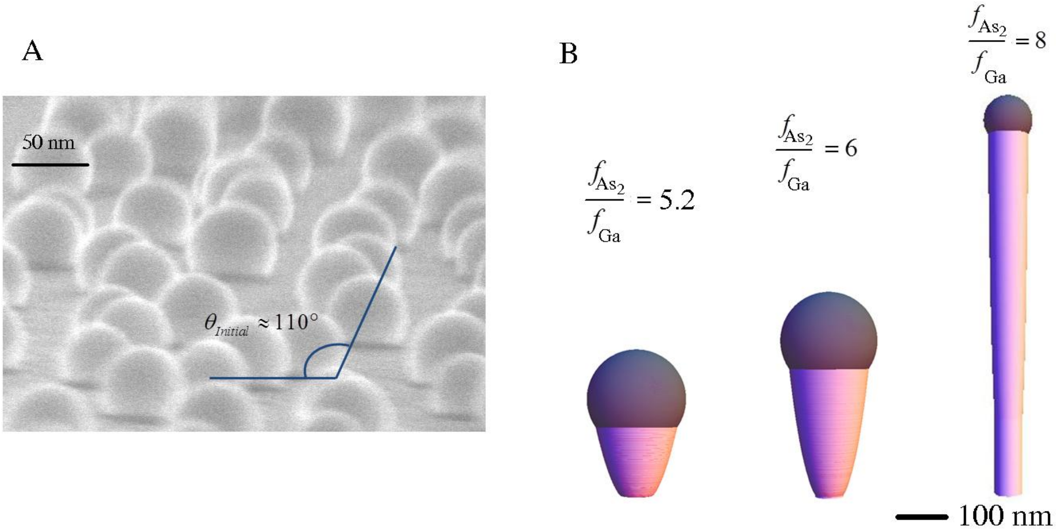

Figure 4-3. Around the lower limit of the V/III growth parameter window, a small change in the incoming As_2 beam flux may cause a big change in the NW morphology. (A) To estimate the initial contact angle and liquid size in the case of self-catalyzed GaAs on Si(111) covered with a native oxide layer, Ga was deposited at the same initial conditions as before a typical NW growth (here 1 min of Ga pre-deposition) but without opening the valve to the As cell. These initial conditions were used for the simulations shown in Figure 4-2 and (B). In (B) the same growth conditions as for the simulations shown in Figure 4-2 have been used.

For patterned growths done on an oxide layer (of approx. 20-30 nm of SiO_x), the substrate diffusion length is strongly desorption limited for both Ga and As species. As it has not been possible to find activation enthalpies for *av* transitions on oxide surfaces in the literature, we simply take it to be half the value on a corresponding crystalline surface. The density of incorporation sites at the oxide surface is set to zero. For the growths on Si (111) wafers with both the native oxide layer and the thermal oxide layer it is assumed that the low energy pathway of diffusion is one dimensional on the NW sidefacets (along the NW growth axis) and isotropic on the substrate.

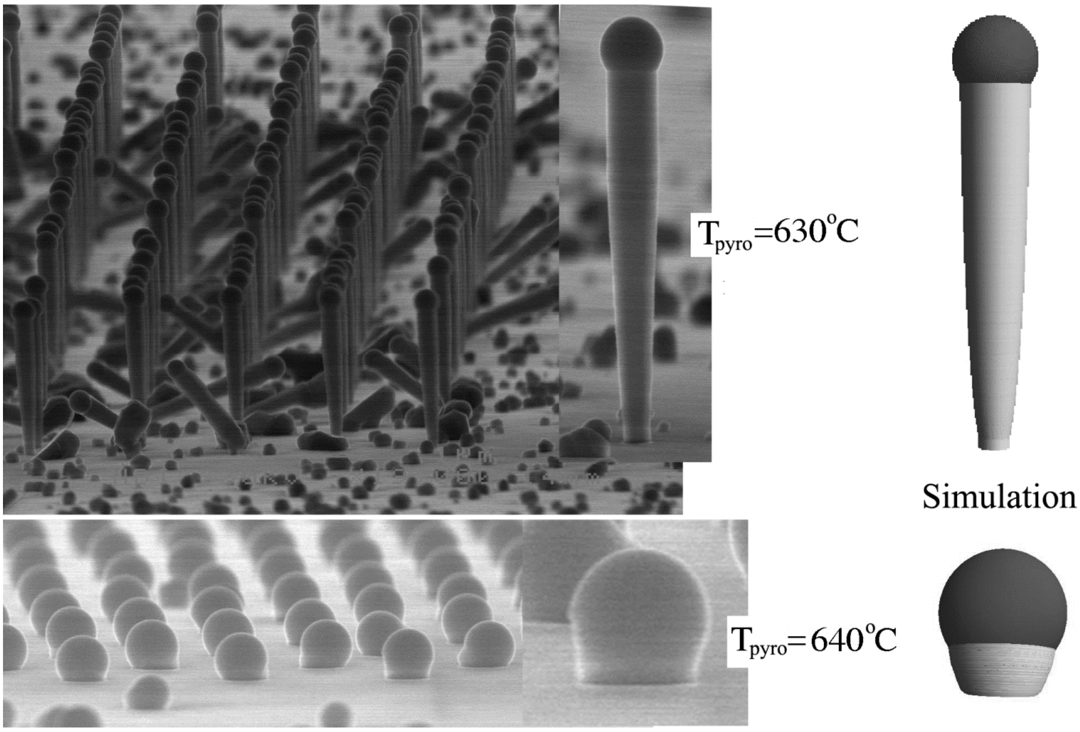

Figure 4-4. Investigation of the upper growth temperature at a given V/III ratio. Positioned Ga assisted GaAs NW growth on Si 111 substrate with a 30 nm thick SiO_x layer. The preparation of the holes in the oxide layer (see ref.52 for details) is done with e-beam lithography on the same 2” wafer and all processing was carried out before the wafer was cut into 4 ¼” wafers just before loading into the buffer chamber. This ensures that the preprocessing has a minimal effect on the final results when comparing the growths. The two growths are grown under exactly same conditions for 20 min, a Ga flux corresponding to a planar GaAs growth rate of $0.9\frac{\mu m}{hr}$ and a measured flux ratio of $\frac{f_{As_2}}{f_{Ga}}=3$ (measured with an ion-gauge filament), but with two different temperatures that were measured just before initiation of the growth with a pyrometer as $T_{pyro}=630°C$ and $T_{pyro}=640°C$. The activation enthalpy for the *av* transition of Ga adatoms on the oxide is set to half the value of the modeling on native oxide and the As species was set to desorb immediately from the oxide (i.e. $\Gamma_{al,As}=0$). Using the same conditions in the simulation (shown on the right) the sharp temperature transition seemed to be at $T_{simulation}=661°C$ and $T_{simulation}=667°C$, which means that there is still some fine tuning of parameters left to be done. The NW crystal formation completely stops at $T_{simulation}=669°C$.

5 Liquid-solid dynamics in regime II

The purpose of this chapter is to carry out a detailed analysis of the dynamical evolution of the liquid-solid phase transition and discuss how different growth conditions and morphologies can affect the specific crystal structure formation probabilities. For such an analysis the ω dependence cannot be neglected due to the anisotropic morphology[III], see Figure 5-1(A). The construction of the growth system at a given ω considered in this section is sketched in Figure 5-1 (B).

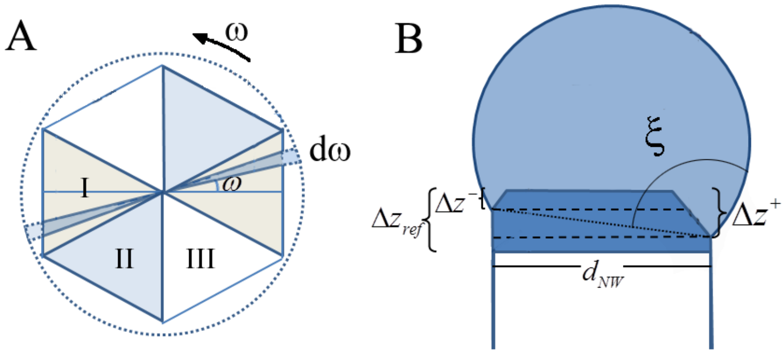

Figure 5-1. (A) Top view illustration of the liquid-solid growth system where three sections indicated with a color and roman numerals are identical but rotated $60°$ degrees, both in case of ZB and WZ structure. $\Delta G_{sys,j}(\omega)$ is the Gibbs free energy of a single slice throughout the growth system. (B) Side view illustration of the growth system at a given ω. The colored region indicates the growth system (dark blue: solid, light blue: liquid), where Δz_{ref} is a reference length to a position from where the solid is considered to be fixed as measured from the topfacet. Δz_{+} and Δz_{-} are the truncation heights at $\omega = 0°$ and $\omega = 30°$, respectively. ξ is the contact angle of the constant curvature construction and is a function of ω.

For a single faceted solid crystal the equilibrium shape is called the ‘Wulff shape’ and can be calculated exactly if the surface energy function in eq.(2.26) is known.[53] But the equilibrium shape of a liquid-solid system is extremely complex to derive and we need to make simplifying assumptions in order to make qualitative predictions of a corresponding liquid-solid ‘Wulff shape’. The Gibbs free energy of the total growth system is given by

$$G_{sys,j} = \int_{0}^{180^\circ} \Delta G_{sys,j}(\omega)\, d\omega \qquad (5.1)$$

where $\Delta G_{sys,j}(\omega)$ is the free energy of a thin 'double cake piece' throughout the whole system, as shown in the top view illustration of a NW with a typical six-fold axial symmetry in Figure 5-1(A). In the following sections will use different simplifications and discuss the predictions and consequences. First we will analyze the dynamics for a single cut through the growth system.

5.1 The single slice construction

In eq.(5.1), the integration of ω using analytical equations is difficult to carry out, thus we will start by looking at a single slice construction for which the liquid curvature stays constant. The choice of the parameter set $\{X(\omega)\}$ used with eq.(2.14) when describing the dynamics of the NW growth system is obviously crucial for the overall evolution of the structure and morphology in the simulation. Recent in-situ growth experiments[54,55,56] have suggested that a truncated morphology at the growth interface edge is a general growth phenomenon, and will therefore be taken into account here. Thus, we will choose the following set, $\{X\} = \{d_{NW}, \Delta z_+, \Delta z_-, \theta_{T+}, \theta_{T-}, \xi\}$, as our parameter set where θ_{T+} and θ_{T-} is the truncation angle at $\omega = 0^\circ$ and $\omega = 180^\circ$ respectively, see Fig 5-2 for details. Note that all these parameters are functions of ω, but only considering a single cut of a finite thickness (of say $d\omega = 1^\circ$) can give us important information of the total three dimensional system.

The *ls* system is continuously adjusting towards $\Delta\mu_{ls}^X = 0$ conditions, but the input of free energy from the beam fluxes, vapor and adatoms and the interplay with anisotropic solid and the nucleation limited growth on the top facet keep the system out of equilibrium. Under certain conditions, the solid can enter a regime where undesired facets are locked in because a free energy barrier has to be overcome in order to form a facet which lowers the total free energy of the system.

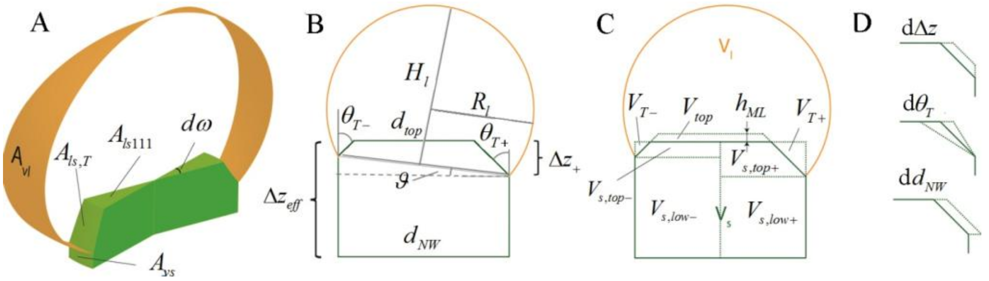

Fig 5-2: Single slice construction in regime II. (A) 3D figure showing the nanowire growth system used in the single slice model. (B) 2D illustration of the involved trigonometric quantities and (C) the volume elements. (D) 2D illustration of the three different ways the truncation can change during growth. The Gibbs free energy of this construction can be calculated using basic trigonometric relations, see Appendix C.

The liquid-solid driving forces of liquid $Ga_{1-x}As_x$ assisted GaAs NW growth is plotted as a function of truncation height Δz for a certain set of fixed parameters in Figure 5-3 using eq.(2.14) on the single slice construction around $\omega = 0°$. In Figure 5-3 (A) it is seen that the equilibrium value of $\Delta z_\pm$ is larger for smaller systems. For the single slice construction the equilibrium morphology will always have a negative truncation. However a non steady state evolution of the growth system can force the system into regime *I* and to get back to regime *II* will require nucleation of a truncated facet which needs a certain formation free energy. Figure 5-3 (B) it is seen that by varying the truncation in one side has a small effect on the truncation on the opposite side in the single slice construction. Figure 5-3 (C) shows an important general trend that truncation heights are generally smallest at smallest droplet sizes. This means that small relatively small droplets have higher probability of going into regime *I* than larger droplets^{III}. In Figure 5-3 (D) it is seen that a strong dependence of the liquid concentration on the truncation size indicates that it is the composition which plays a dominating role on the oscillating morphology as already predicted by ref.[40]. Figure 5-3 (E) and (F) shows the driving forces around certain facets in the case of ZB and WZ structure, respectively. For a certain set of orientations and parameters the system need to form another facet orientation to move into a quasi equilibrium state. If the potential barrier to form such a facet is large, the system can go into a metastable growth mode, or possibly regime *I*.

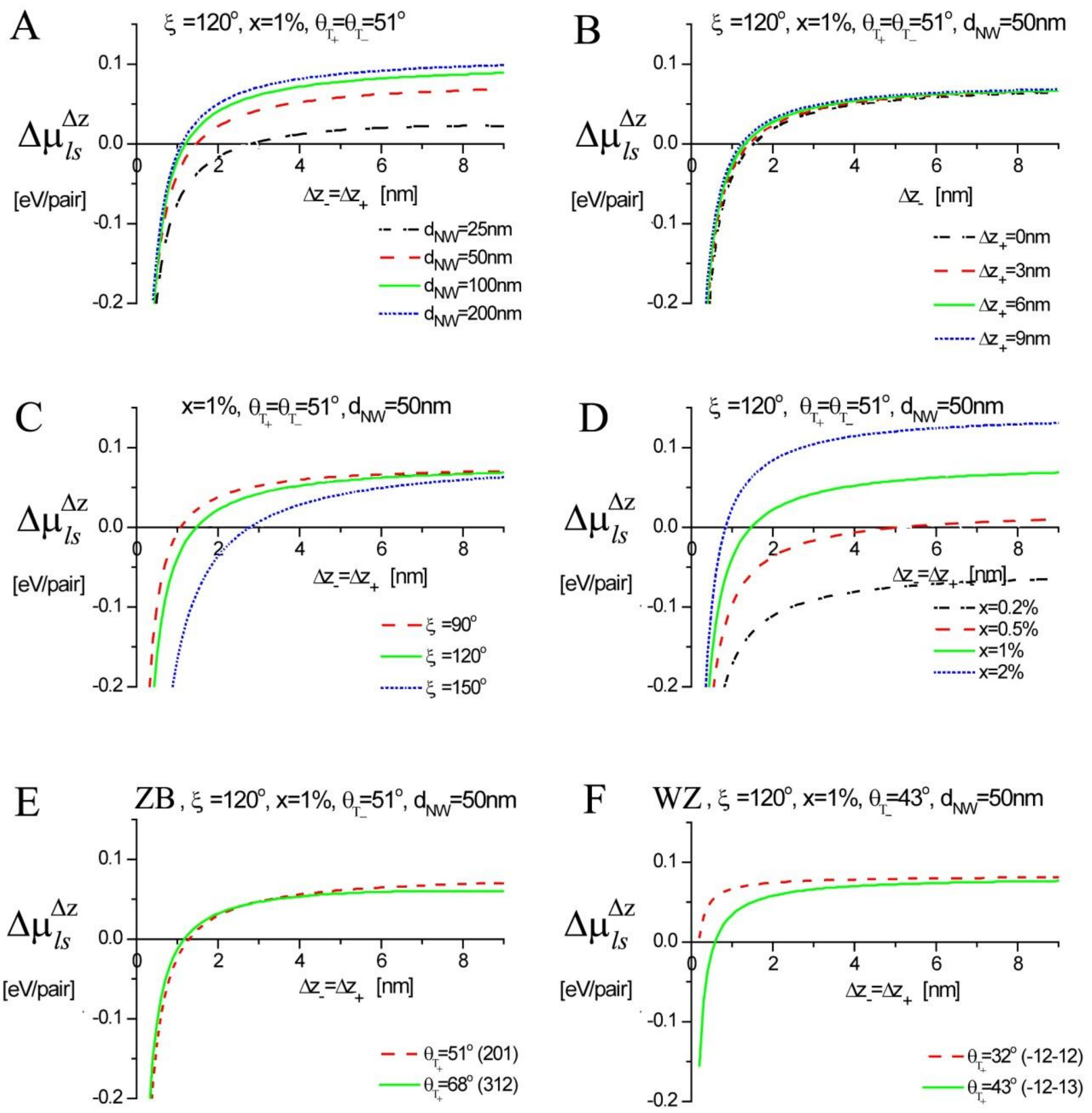

Figure 5-3. Plots of driving forces $\Delta\mu_{ls,i}^{\Delta z} = \delta\mu_{l-ERS.i} - \delta\mu_{s-ERS.i}^{\Delta z}$ of Ga Assisted GaAs NW growth as a function of the truncation size for the single slice construction at $\omega = 0°$ with $\left\{1\bar{1}0\right\}$ type sidefacets at $T = 630°C$. The equilibrium value of the parameters under the fixed conditions are where $\Delta\mu_{ls} = 0$. (A) It is seen that the equilibrium value of $\Delta z_{\pm}$ is larger for smaller systems, at least for the given set of parameters. For the single slice construction the equilibrium morphology will always have a negative truncation. (B) By varying the truncation in one side has a small effect on the truncation on the opposite side in the single slice construction. (C) Truncation heights are generally smallest at smallest droplet sizes. (D) A strong dependence of the liquid concentration on the truncation size indicates that it is the composition which plays a dominating role on the oscillating morphology as already predicted by ref.[40]. (E) and (F) shows the driving forces around certain facets in the case of ZB and WZ structure, respectively.

In Figure 5-4 (B) and (C) it is shown that the truncation angles affect the driving forces in a more complicated way than the other parameters which are chosen here. This implies that the system can stay far from equilibrium in a dynamical metastable and possibly steady state regime, see Figure 5-6.

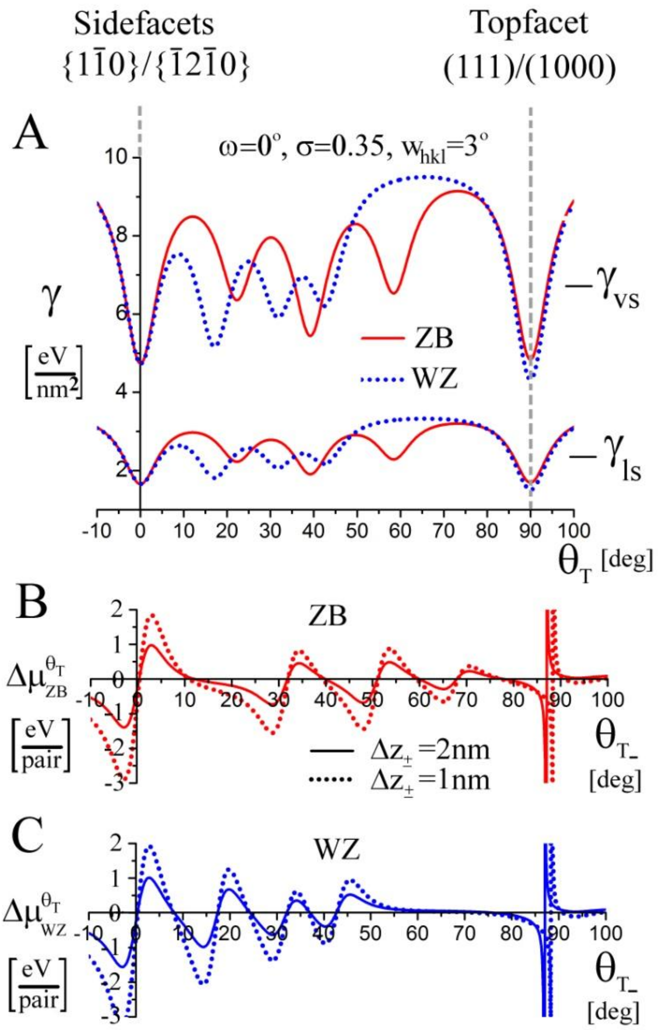

Figure 5-4. (A) The 2D γ-plots using eq.(2.26) for the *vs* and *ls* interfaces for the single slice construction in the case of ZB and WZ structure around $\omega = 0°$ and $\gamma_{pq0} = 10\frac{eV}{nm^2}$. The low energy orientations used are listed in Appendix B for ZB and WZ structure. The lowest interface energies just equal the lowest in ZB to emphasize the angular dependence. It is seen that when only taking account of the interface orientation with the highest symmetry WZ is dominant at small θ's and ZB is dominant at large θ's. Driving forces $\Delta\mu_{ls,i}^{\theta_T} = \delta\mu_{l-ERS.i} - \delta\mu_{s-ERS.i}^{\theta_T}$ for Ga Assisted GaAs NW growth as a function truncation angle in the case of ZB and WZ is plotted as a function truncation facet angle for ZB (B) and WZ (C), respectively. The parameter set are $d_{NW} = 50\,nm$, $\xi = 120°$, $x_V = 1\%$ and $\theta_{T+} = 51°$ for ZB and $\theta_{T+} = 43°$ for WZ. The stable points are the ones where the driving force is zero and the gradient of the driving force is positive. The plot tells us that it is not possible to switch freely between facet orientations. The singularities close to 90° are due to the definition of the truncation angle shown in Fig 5-2 (D), because the system cannot approach a single topfacet for a fixed Δz value.

The surface energies and the interface energy function given by play a crucial role on the NW growth in general and on the truncation dynamics in particular. The interface energy function is plotted for the single slice construction in Figure 5-4 using eq.(2.26). w_{hkl}, which specifies the half-width half maximum of the energy decreases around the (hkl) facet is an important parameter for the dynamical system. If w_{hkl} is small the corresponding truncation facet orientation is locked to a low energy facet orientation and it is unlikely that the facet can overcome the energy barrier $\Delta G_{ls,III-V}^{\theta_{T1}-\theta_{T2}}$ needed to form another facet and a more preferable configuration. In Figure 5-4 (B) and (C) shows how the *ls* driving force for truncation angle depends on the orientation for a given parameter set, where $\Delta z = 2nm$ is closer to equilibrium than $\Delta z = 1nm$. Examples of dynamical simulations are shown in Figure 5-5 and Figure 5-6. In Figure 5-5 a short simulation of the truncation dynamics shows the evolution of the truncation height and orientation.

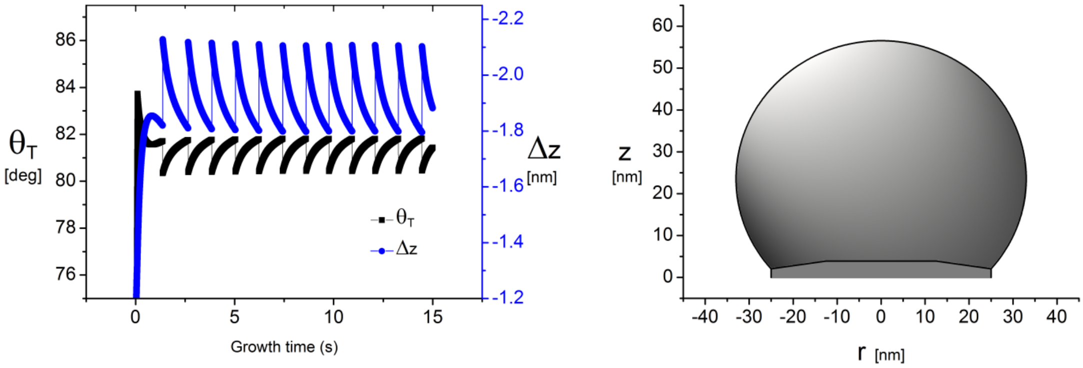

Figure 5-5. Example of a 15 sec growth simulation S6 of self-catalyzed GaAs NW on Si, where the quasi steady state growth mode is reached quickly, only after formation of the first ML. On the left, the truncation height and truncation angle are oscillating in coherent manner with periods of the formation of a ML at the topfacet. The NW morphology is shown after 15 sec of the growth on the right.

Only small oscillations on the atomic layer level are seen here, but a change in some of simulation parameters, such as changing the ratios between the involved interface energies can lead to stronger oscillations. For example a higher *vl* surface energy can give stronger oscillations. It is important to emphasize that this is a continuum approach where it has not been taking into account that facet orientations in principle becomes discrete when Δz becomes small. The formation of a new facet orientation can be nucleation limited if the barrier is larger than the single transition state barrier

$\Delta G_{ls,III-V}^{\theta_{T1}-\theta_{T2}} > \delta g_{ls,III-V}^{TS,ERS}$ and such a transition has to be treated in the framework similar to that of section 2.3. These transitions will not be treated in detail here, but in the simulations the probability of forming another truncation facet orientation simply depends on the evolution of the system morphology. For large values of w_{hkl} the angle of the truncation facet can change more or less freely and it will oscillate in accordance with the oscillations of the growth system. But, in fact to make qualitative predictions about a given growth system and the structural formation probabilities it is necessary to have reasonable good estimates of the parameters describing the surface energy functions.

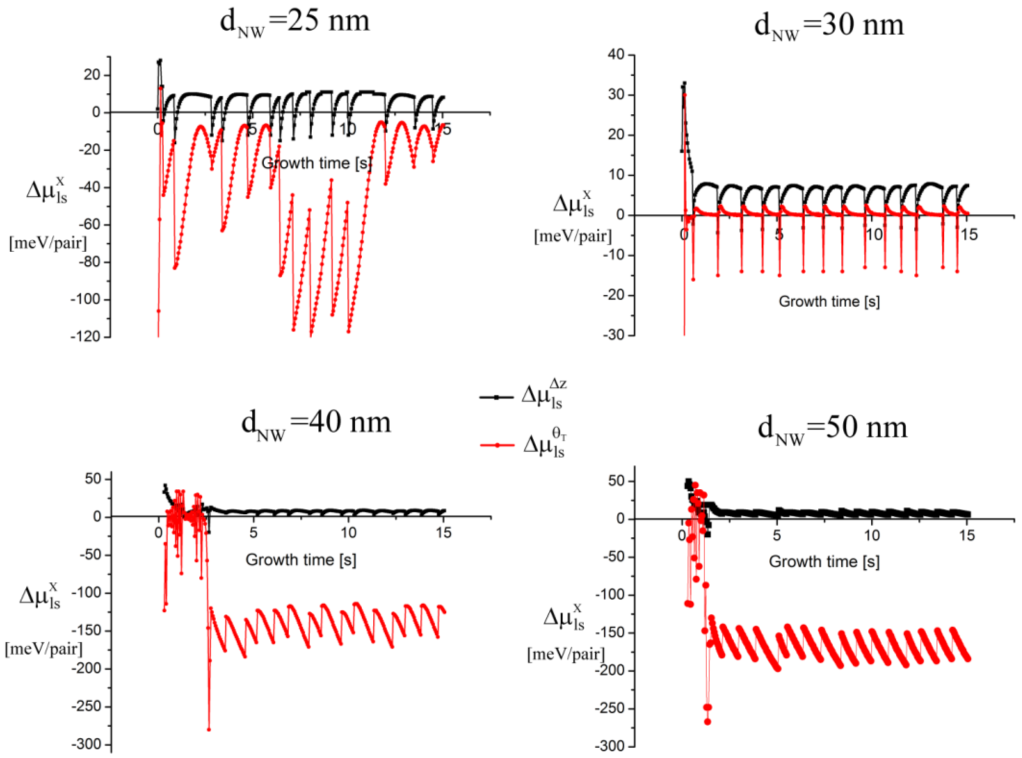

Figure 5-6. For a given set of initial conditions the *ls* driving forces forming the truncation facets are plotted as a function of 15 seconds of growth time (growth simulations S1). At smaller diameters the growth system seems highly unstable which is due to not only the initial conditions but also to the solid anisotropy. For $d_{NW} = 30\,nm$ the system moves into a steady state regime not far from equilibrium, this means that the initial conditions fit well with the energies for the system. At larger diameters the system moves into a steady state regime far from equilibrium, because the evolution of these systems prefers another configuration but are looked by the barrier of forming a more stable shape.

This is indicated in Figure 5-7 where each set of simulation parameters gives different results. For large values of w_{hkl} the angle of the truncation facet can change more or less freely and it will oscillate in accordance with the oscillations of the growth system

(Figure 5-5). But, in fact to make qualitative predictions about a given growth system and the structural formation probabilities it is necessary to have reasonable good estimates of the parameters describing the surface energy functions. This is indicated in Figure 5-7 where each set of simulation parameters gives different results. A strong anisotropy of the interface energy at the truncation implies that the facets can be locked in a far from equilibrium state in a dynamical metastable and possibly steady state regime, see Figure 5-6. For the single slice construction in regime *II* it is in principle possible to predict the impact of the system size and morphology on the relative formation rates of ZB and WZ stacking, given a set of simulation parameters.

In Figure 5-7 (A,B,C) three different simulations S1, S2, S3 of the truncation dynamics show some general trends as a function of the system size, even though huge quantitative differences are seen due to changes in the parameters determining the shape of the interface energy functions. The quantities which are plotted here are average values after reaching a quasi steady state, see Appendix D for examples of the truncation dynamics. Parameters used for the simulations are listed in Appendix B and E. If truncation edge nucleation dominates at the topfacet, WZ would be favored at small diameters and ZB at larger diameters according to the simulations shown in Figure 5-7 A, if considering only the facets with the lowest energies in the interface energy function (as plotted in Figure 2-5). In Figure 5-7 (B) it is seen that the truncation height seems to be smaller with increasing size of the system, even though it does not necessarily have a monotone dependence due to the anisotropic interface energy. In Figure 5-7 (C) the axial growth rate is strongly dependent on the size of the system, however the actual dependence depends on the simulation parameters used, where role of the relative liquid size does also play an important role on the truncation angle as seen in Figure 5-7 (D). Thus, due to the complexity of the growth system, the theoretical development is still not mature enough to make any conclusive statements on the structural formation probabilities as function of growth parameters.

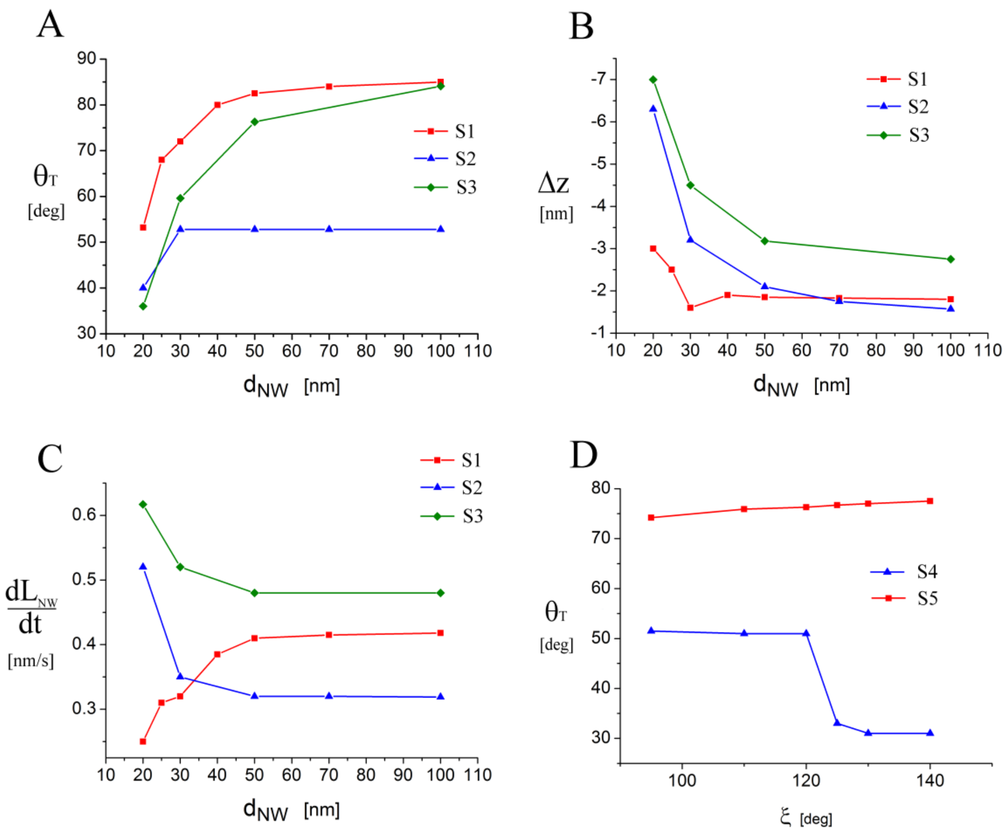

Figure 5-7. Simulations of 15 sec of growth in the single slice construction of self-catalyzed growth of GaAs in the beginning of growth, at $\omega = 0°$ where the system choose symmetry, $\Delta z = \Delta z_- = \Delta z_+$ and $\theta_T = \theta_{T-} = \theta_{T+}$. (A,B,C) Three different simulations S1, S2, S3 of the truncation dynamics show some general trends as a function of the system size, even though huge quantitative differences are seen due to changes in the parameters determining the shape of the interface energy functions. The quantities which are plotted here are average values after reaching a quasi steady state, see Figure 5-5 for examples of the steady state truncation dynamics. Parameters used for the simulations are listed in Appendix B. (A) All simulations we have done so far give a general trend, namely that smaller systems gives smaller average truncation angles. However it is difficult for the systems with sharp cusps in the $\gamma_{ls}(\theta)$ function, to break out of the local low energy angles and it will therefore stay constant almost without oscillations. (B) The truncation height seems to be smaller with increasing size of the system, even though it does not necessarily have a monotone dependence due to the anisotropic interface energy. (C) The axial growth rate is strongly dependent on the size of the system, however the actual dependence relies on the simulation parameters used. (D) Two simulations at $d_{NW} = 50\,nm$. The role of the relative liquid size does also play an important role on the truncation angle, but as the other plots also indicate, the huge parameter space needs to be explored in more detail before any refined conclusions can be made.

5.2 Geometrical analysis of a constant *vl* curvature construction and total facetting.

To analyze the total liquid-solid dynamics we need to include the ω- dependence on all parameters in the parameter set, $\{\mathrm{X}(\omega)\}$. However this is as mentioned a very complex problem and we will here make some geometrical simplifications in order to get qualitative ideas and better understanding about the three dimensional system. As compared to the single slice construction above at least one additional parameter, namely $\eta(\omega)$ (see eq.(2.24)), needs to be added to the parameter set. If the liquid is assumed to have a constant curvature an example of a choice of parameter set could be; $\{\mathrm{X}(\omega)\} \in \{d_{NW}, \eta, \Delta z_+, \Delta z_-, \theta_{T+}, \theta_{T-}, \xi\}$. The form of $\eta(\omega)$ which describes the cross sectional shape of the growth interface, is very important for the total configuration but it is also a very complex parameter to include. It has not been possible in the time of writing to find a consistent method to solve this system. In this section we will instead show some implications of typical assumptions used for modeling NW growth, which will serve as instructive and informative insight to the three dimensional anisotropic system. Such as under which configurations and conditions the NW growth system will move in and out of regime *I* and *II*. The free energy minimization process of the *ls* system during growth is complex mainly due to the interplay between the isotropic liquid and the anisotropic solid. If we imagine that the cusps of the gamma-plot shown in Figure 2-5 (B) and (C) are very sharp and deep, then the system will choose total sidewall facetting even at the TL, and the liquid phase will 'adjust' to this as long as the system is regime *II*. In regime *I* the nucleation statistics can be treated in the framework proposed in ref.[III], which is mainly a relevant regime during changes in growth conditions where the relative size of the liquid is decreasing. If we furthermore assume that the *vl* interface tension is strong, the isotropic (and assumed homogenous) liquid prefers a constant curvature due to a strong Laplace pressure. To describe such a system we will first choose a single slice construction which is oriented in such a way that $\omega = 0^\circ$ is in the direction of the liquid-solid displacement, Δr (see Figure 5-8 (A)). Using cylindrical coordinates, (r, ω, z), we can write two intersections between the wire and liquid as $(r_-, 180^\circ, z_-)$ and $(r_+, 0^\circ, z_+)$. For a given radius of curvature there exist two solutions, one for $\xi \geq 90^{\circ}$ and one for $\xi < 90^{\circ}$, as seen in Figure 5-8 (B). Here $z_{-} = -\frac{\Delta}{2} - \frac{d_{NW0}}{2}\sqrt{\frac{4R_l^2 - \Delta^2 - d_{NW0}^2}{\Delta^2 + d_{NW0}^2}}$, and the two intersections are given by

$$\left.\begin{aligned}\left(r_{-},180^{\circ},z_{-}\right) &= \left(-\sqrt{R_l^2 - z_{-}^2},180^{\circ},z_{-}\right)\\ \left(r_{+},0^{\circ},z_{+}\right) &= \left(-\sqrt{R_l^2 - z_{+}^2},0^{\circ},\Delta + z_{-}\right)\end{aligned}\right\} \quad for \quad \xi \geq 90$$
$$\left.\begin{aligned}\left(r_{-},180^{\circ},z_{-}\right)' &= \left(-r_{+},0^{\circ},-z_{+}\right)\\ \left(r_{+},0^{\circ},z_{+}\right)' &= \left(-r_{-},180^{\circ},-z_{-}\right)\end{aligned}\right\} \quad for \quad \xi \leq 90 \tag{5.2}$$

where $\Delta = \Delta z_{-} - \Delta z_{+}$ is difference in truncation in the two sides and d_{NW0} is the diameter at $\omega = 0^{\circ}$. The z-coordinate for intersection between wire and liquid as a function of ω are then given by, $z(\omega) = -\sqrt{R_l^2 - \left(\cos(\omega)d_{NW}(\omega) + \Delta r\right)^2 - \left(\sin(\omega)d_{NW}(\omega)\right)^2}$, where $\Delta r = \sin(\vartheta)\sqrt{R_l^2 - \frac{d_{NW0}^2}{4\cos(\vartheta)^2}}$ is the displacement between of center of the NW crystal and the liquid center at $\omega = 0^{\circ}$. Now analyzing the wetting consequences when assuming total facetting ($\eta(\omega) = 0$) will give us some qualitative ideas about the real system and under which conditions TL nucleation can take place. In Figure 5-9 the truncation heights are plotted for different relative sizes of the droplets and for six-fold and three-fold facetting. It is obvious that a relative large droplet will have a smaller probability of inducing positive truncations and it is also obvious that a hexagonal shape is the most convenient shape in relation with a liquid. If we allow for a three-fold facetting we need to define two lengths, r_{-} and r_{+}, to describe the diameter, see Figure 5-8 (C). It is very likely that for real systems that the truncation is negative all the way around the TL and only becomes positive at a given location when the liquid supersaturation is high and induce either TL nucleation or move the TL into regime *I*. A TEM image along the $[1\bar{1}0]$ zone axis of a GaAs NW with a Ga droplet on top is shown in Figure 5-8 (D). The red circle on the enlarged view is a perfect circle, which fits almost perfect to the shape of the Ga droplet.

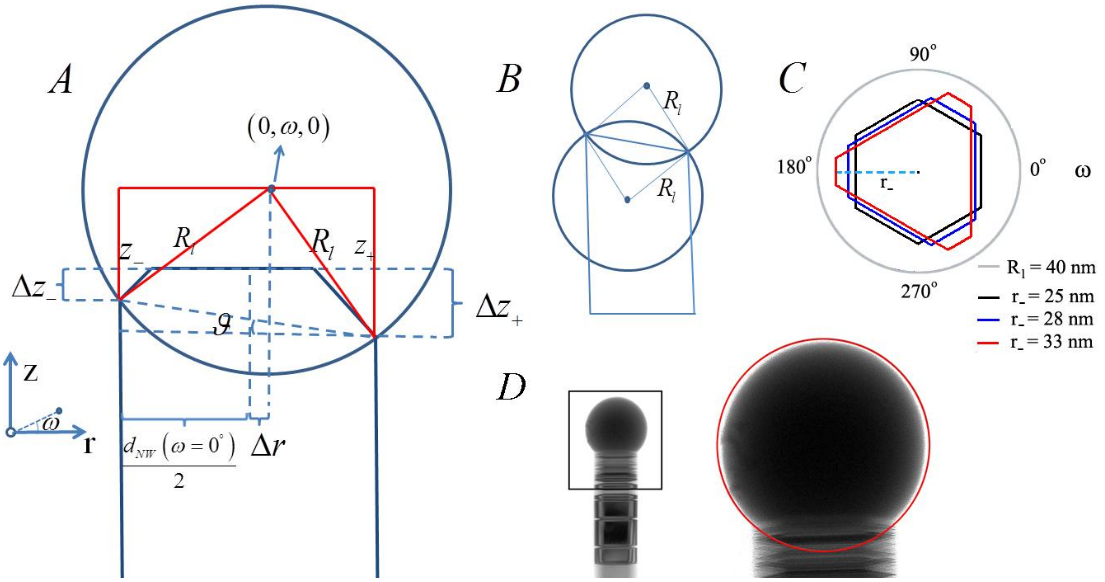

Figure 5-8. (A) Illustration of the trigonometry used to derive the Δz vs ω relation for the constant vapor-liquid curvature construction and $\eta(\omega)=0$. (B) For a given radius of curvature there exist two solutions, one for $\xi \geq 90^\circ$ and one for $\xi < 90^\circ$. (C) If we allow for a three-fold symmetric morphology we need to define two lengths, r_- and r_+, to describe the diameter. However for a given crystal volume only r_- is needed, see eq.(2.25). (D) A TEM image along the $[1\bar{1}0]$ zone axis of a GaAs NW with a Ga droplet on top. The red circle on the enlarged view is a perfect circle, which fits almost perfect to the shape of the Ga droplet.

Thus if this is a general property of the *ls* growth system, we can say that if the NW crystal completely faceted $\eta_0 = 0$ the truncation height would vary as a function of ω as shown in Figure 5-9. In the other extreme if the system is completely axi-symmetric $\eta_0 = 1$ the truncation height would be independent of ω. It is important to note that for real liquid-solid growth systems using the η_0 parameter to describe the system would give a value somewhere in between 0 and 1, and the amplitude of the curves in Figure 5-9 will be smaller. See the figure text for a discussion of different cases of total facetting and constant liquid curvature.

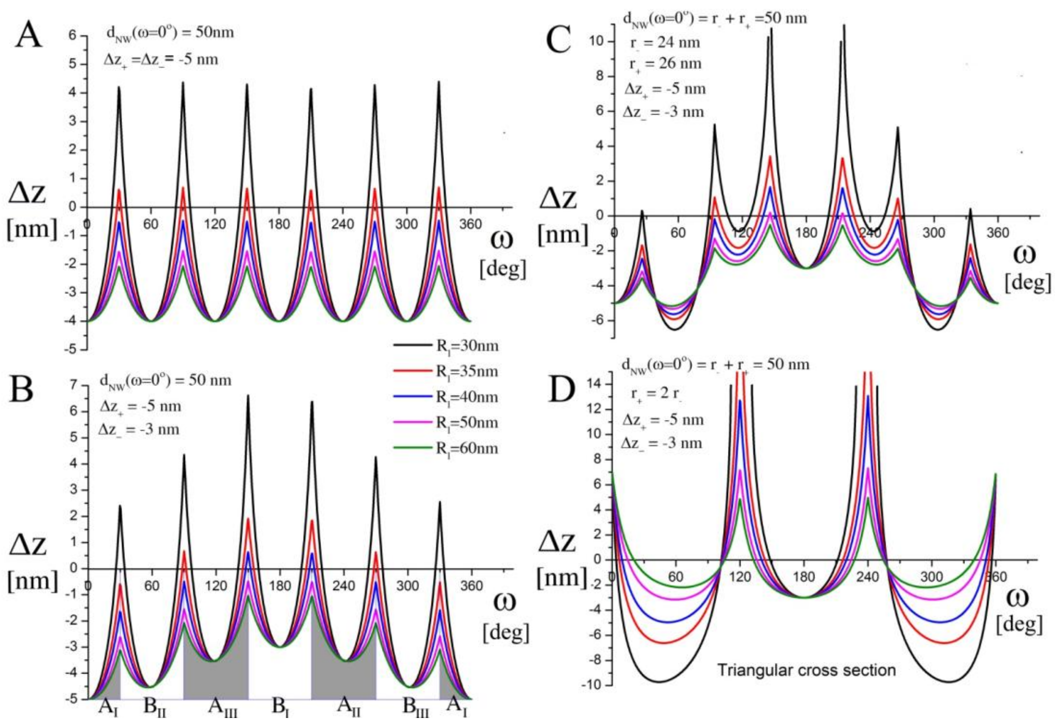

Figure 5-9. Geometrical representation of the truncation size, Δz, as a function of ω and different liquid sizes, for a NW system with $d_{NW}(\omega = 0^{\circ}) = 50\ nm$ assuming constant vapor-liquid curvature and total facetting at the same time. (A) Assuming equal truncation $\Delta z_- = \Delta z_+$ at both sides at $\omega = 0^{\circ}$, as initial conditions on a complete facetted solid hexagonal cross section. (B) If the crystal has three-fold symmetry but takes on a six-fold morphology it can be favorable to incline the growth system. However, assuming vertical sidewalls it can be shown that the system does not lower the free energy because the areas of A and B type facets are the same in total (indicated by grey and white regions) and the system either chooses to make the A facets smaller and the B facets larger as shown in (C). It should be noted that an inclination angle could be initiated by a non-isotropic incoming vapor flux due to the Marangoni effect[57] but this is out of the scope of this study. In (C) it is seen that if the solid induce even a small derivation from the hexagonal shape, it has a huge impact on the growth system which will most likely also be present in the real system. (D) In the extreme case of a triangular shaped NW and constant *vl* curvature, the system will be in regime *I* for all truncation sizes in the case of $R_l > 37\ nm$ around the edges of the triangle. This is because there is no solution to the sidefacet-liquid intersection problem. In this case the edges will be either rounded or TL has moved in on the topfacet and the facet edges may be completed by surface diffusion.

In Figure 5-10 we see the relationship between parameters; d_{NW}, ξ, Δz and ω under six fold and three fold symmetric sidewall facetting in the case of constant liquid curvature.

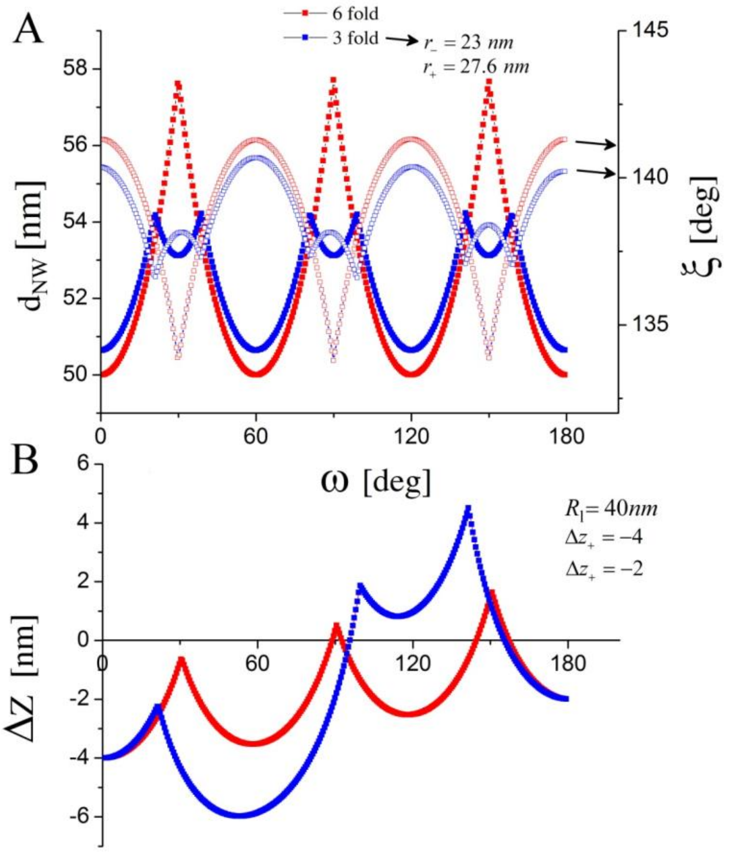

Figure 5-10. Comparison between a perfect 6-fold hexagonal shaped NW (red) and a three-fold cross sectional morphology (blue) for a given crystal volume, under the assumption of constant *vl* curvature and total facetting. (A) The solid dots represent the NW diameter and the open dots represent the contact angle. (B) In the case of a strong driving force towards 3-fold sidewall facetting it is likely that the TL will move in on the topfacet, here in the region around $\omega \sim 120^\circ$. For $\omega \in [180^\circ, 360^\circ]$, the curves are mirrored in $\omega = 180^\circ$.

6 Radial growth rate estimates for low temperature shell growth

In the previous chapters focus has been on the axial NW growth via the VLS mechanism. In this chapter we turn the focus towards radial shell vapor-solid (VS) growth, i.e. turning to conditions where the diffusion lengths of all the limiting growth elements are small due to a high driving force for the *as* incorporation. Such conditions are promoted at low temperatures and high pressures/beam fluxes. We will assume that the temperature is low enough and the beam fluxes high enough such that we can consider only contributions of the direct impingement from the beam flux of the limiting element. The radial shell growth is in many ways equivalent to standard planar growth where the limiting element is typically group III. Therefore, we only need to consider the incorporation of group III atoms, which at low temperatures and high beam fluxes of mainly group V is incorporated relatively close to the point of impingement on the sidewall. However it is important to mention that the surface might get rough under too low temperatures and/or too high pressures. Thus there is a certain limits and they therefore needs to be adjusted precisely. To obtain control of the radial growth rate the important parameter here is the diffusion length of group III elements, $\lambda_{NW,III}$, which ideally should be on the order of the nanowire diameter when growing a shell on a perfect faceted NW crystal. Different equations for the radial growth rate under different conditions are derived below. These formulas can be used to compare with the corresponding planar growth rate, and can give us important information on the whether the radial growth is obtained only by direct impingement, diffusion from the substrate or from vapor states.

6.1 Radial growth rates at low nanowire densities for $\lambda_{NW,III} << L_{NW}$

Here we derive an expression for radial growth rates in the case of non-tapered NWs grown at low temperatures, where shadowing effects from adjacent NWs are neglected, i.e. at low NW densities. Under these conditions we can neglect the axial growth and the NW length can be assumed to be constant, $L_{NW}(t_{rad}) = L_{NW}(t_{ax})$, where t_{rad} and t_{ax}

is the total radial and axial growth time respectively. At low temperatures the effective diffusion length of group III elements at the NW sidewall is small due to a high adatom to solid thermodynamic driving force. At a given time t of radial growth, the volume of the shell of a hexagonal shaped NW is given by the expression

$$V_{shell}(t) = A_{shell}(t)\cdot L_{NW} = \frac{3\sqrt{3}}{8}\left(d_{NW,rad}^{2}(t) - d_{NW,ax}^{2}\right)\cdot L_{NW} \tag{6.1}$$

where $d_{NW,rad}(t)$ is the diameter of the NW at radial growth time t and $d_{NW,ax}(\omega)$ is the diameter of the NW obtained during the axial growth step. The diameters is measured at $\omega = 30°$, see Figure 6-1A. Now due to a short sidewall diffusion length and total sticking of group III elements, conservation of mass implies $\frac{d}{dt}V_{shell}(t) = \Omega_{III-V} f_{III,\perp} A_{col}(t)$ where the effective collection area is given by $A_{col}(t) = \left(\frac{2+\sqrt{3}}{4}\right) d_{NW,rad}(t) L_{NW} \sin\left(\phi_{III}\right)$. With this, the time dependence on the NW diameter can be derived

$$d_{NW,rad}(t) = d_{NW,ax} + \frac{2+\sqrt{3}}{3\sqrt{3}} GR_{planar} \tan(\phi_{III})\cdot t \tag{6.2}$$

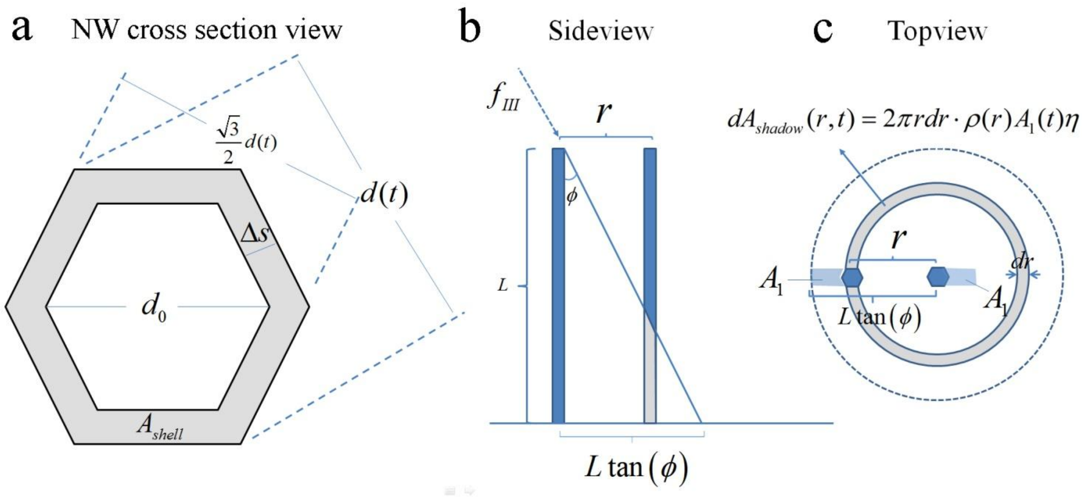

Figure 6-1. Geometrical considerations for deriving the formulas for the radial growth rates at low temperatures. (a) The radial growth is assumed to grow uniformly in a hexagonal cross sectional shape. (b) and (c), sideview and topview illustrations of the shadowing effect from a single adjacent NW. In (c) it is seen that the integration needs to be carried out from $r = L_{NW}\tan(\phi)$.

6.2 Radial growth rates including shadowing effects for $\lambda_{NW,III} << L_{NW}$

If the NW density ψ on the substrate is high and the NW lengths and diameters are relatively large, shadowing effects from adjacent NWs needs to be taking into account when estimating the radial growth rate. The average impinging flux towards the NW tip will be larger than at the bottom which will lead to reverse tapering effects if $\lambda_{NW,III} << L_{NW}$. It is therefore necessary to calculate the radial growth as a function of the NW length, l_{NW}. Here the mass continuity equation at a given element dl_{NW} at l_{NW}, is given as,

$$\frac{d}{dt} dV_{shell}(l_{NW},t) = \Omega_{III-V} f_{III} \left(dA_{NW}(l_{NW},t) - dA_{shadow}(l_{NW},t) \right) \tag{6.3}$$

where $dA_{NW}(l_{NW},t) = d(l_{NW},t)\sin(\phi_{III})dl_{NW}$ is the collection area of a segment dl_{NW} at l_{NW}. The shadowing term is given as

$$dA_{shadow}(l_{NW},t) = \int_{r'}^{(L_{NW}-l_{NW})\tan(\phi)} d\left(dA_{shadow,r'}(l_{NW},t) \right) \tag{6.4}$$

where $dA_{shadow,r}(l_{NW},t) = \psi(r) dA_1(l_{NW},t) 2\pi r dr$ is the shadowing effect from NWs located at r. $r' > d_{NW,rad}$ is the starting point of the integration which is the point from where it is likely to meet another NW. The effective area at which a single adjacent NW at r is shadowing a segment dl_{NW} at l_{NW} is given as

$$dA_1(l_{NW},t) = dl_{NW} \cdot d_{NW,rad}(l_{NW},t) \cdot \sin(\phi_{III}) \frac{d_{NW,rad}\left(l_{NW} + \frac{r}{\sin(\phi_{III})}, t \right)}{2\pi r}$$

. If we assume that the fraction of time at which a specific point on the NW is shadowed by the wire at l_{NW} is constant along the shadowed part, the radial growth in terms of the NW diameter can finally be derived,

$$d_{NW,rad}(l_{NW},t) = \mathrm{K}_1 + \left(d_{NW,ax} - \mathrm{K}_1\right)\exp\left(-\frac{4}{3\sqrt{3}} GR_{planar}\tan(\phi_{III})\mathrm{K}_1^{-1}\cdot t\right) \tag{6.5}$$

where $\mathrm{K}_1 = \dfrac{1}{\psi\left((L_{NW} - l_{NW})\tan(\phi_{III}) - r'\right)}$. Here $\psi(r) = \psi$ is a constant (from r' to infinity).

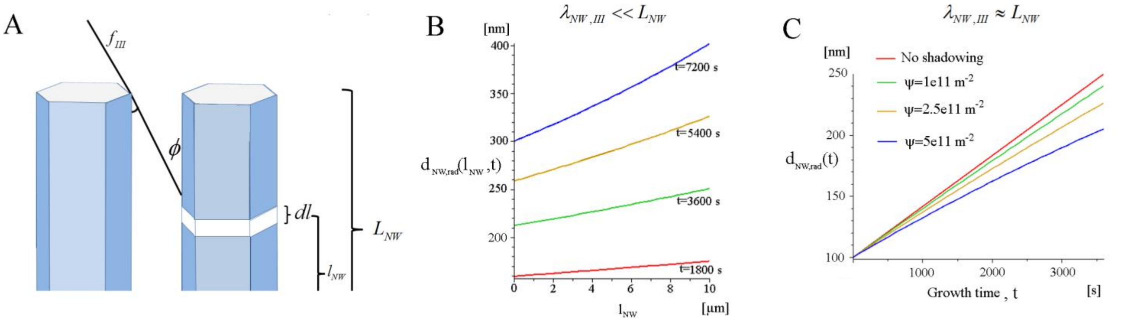

Figure 6-2. (A) Illustration of the geometrical considerations involved in the derivation of the shadowing effect. (B) Radial growth rates including shadowing effects for $\lambda_{NW,III} << L_{NW}$, as derived in section 6.2. The reverse tapering becomes more and more visible with time. For the plotting a NW density of $\psi = 2.5\cdot 10^{11}\,m^{-2}$ is used. (C) Radial growth rates including shadowing effects for $\lambda_{NW,III} \approx L_{NW}$, as derived in section 6.3.

6.3 Radial growth rates including shadowing effects for $\lambda_{NW,III} \approx L_{NW}$

If we are in regime a where the diffusion length is comparable to the length of the NWs ($\lambda_{NW,III} \approx L_{NW}$), and where the net transition flux of group III going from the substrate to the sidewalls is zero ($\Delta\Gamma_{a_{NW}a_{sub},III} = 0$), we can expect a uniformly distribution of the impinging material along the NW length. First, the effective area at which a single wire at interwire distance r is shadowing is given by $A_1(t) = \left(L_{NW}\tan(\phi) - r\right)\dfrac{d_{NW,rad}^2(t)}{2\pi r}$, where $\dfrac{d_{NW,rad}(t)}{2\pi r}$ is the fraction of time where a specific point on the NW is shadowed by the wire at r, see Figure 6-1B,C. In this case the shadowing effect on the collection area is simply given as $A_{shadow}(t)=\int\limits_{r'}^{L_{NW}\tan(\phi_{III})}\psi(r)A_1(t)2\pi r dr$. Using the mass continuity equation for group III,

$$\frac{d}{dt}V_{shell}(t)=\Omega_{III-V}\,f_{III}\left(A_{NW}(t)-A_{shadow}(t)\right) \tag{6.6}$$

and assume that $\psi(r)$ is a constant (from r' to infinity) and $L_{NW}\tan(\phi_{III})>>r'$, we arrive at the radial growth rate in terms of the diameter,

$$d_{NW,rad}(t)=\mathrm{K}_2+\left(d_{NW,ax}-\mathrm{K}_2\right)\exp\left(-\frac{4}{3\sqrt{3}}GR_{planar}\tan(\phi_{III})\mathrm{K}_2\cdot t\right) \tag{6.7}$$

with $\mathrm{K}_2=\dfrac{\sin(\phi_{III})}{\psi\left(\tan(\phi_{III})\left(\dfrac{L_{NW}\tan(\phi_{III})}{2}-r_0\right)+\dfrac{r'^2}{2L_{III}}\right)}$.

The equations derived in section 6.1, 6.2 and 6.3, can serve as estimates for radial growth rates. If the thickness does not corresponds to the estimated value predicted in section 6.1 and 6.2, it is most likely because $\lambda_{NW,III}<<L_{NW}$ is not fulfilled and that adatoms form the substrate are contributing to the growth. This means that in order to make the adatom diffusion length smaller, the temperature needs to be lowered or the As flux need to the raised. However, one should be careful not to exceed the roughening transition and degrade the crystal structure.

7 Analysis for structural phase formation in self-catalyzed GaAs nanowires

This chapter is primarily based on the results presented in the papers [II] and [IV], and the aim is to show and discuss both post growth and in-situ experimental characterization results of the crystal structure formation. It is well known that it is possible to affect the structural phase formation by tuning the growth conditions[58,II,IV]. In the case of self-catalyzed GaAs nanowires the preferential structure under quasi steady state growth conditions is typically ZB[59]. However, the density of twin planes (TPs) is generally observed to be highest in the beginning and in the end of the growth, consistent with previous reports on the structural distribution along the NWs[60,61]. This is an indication that changes in the growth conditions changes the relative formation rate probabilities discussed in section 3. However, it is important to mention that there can be a wide variety of structural distributions along the NW length as it depends on the complicated interplay between the various parameters describing the growth. Thus, it is not a straightforward task to obtain a perfect crystal structure throughout the whole NW because the effective V/III ratio, $\frac{I_V}{I_{III}}$, changes as the NW grows longer. This is seen in typical TEM images of a self-catalyzed GaAs NW in Figure 7-1, where the temperature and beam fluxes are kept constant during growth, but where the density of TPs and therefore the probability of forming WZ structure increases during growth.

To explain this we have to look at the adatom kinetics in the dynamical framework. In order to simulate a particular growth we need to make detailed considerations of the particular conditions which were present during growth. At typical growth conditions parasitic GaAs chunks is forming in between the NWs. This means that as the wires are growing the density of incorporation sites $\overline{c}_{inc,III(V),sub}$ changes in a very complicated way.

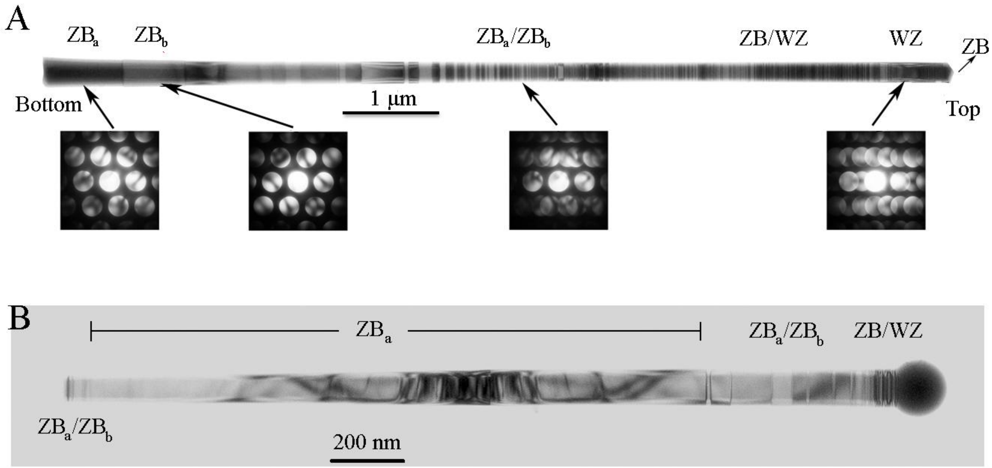

Figure 7-1. (A) A TEM image of a GaAs NW grown with a V/III ratio of 20 (as measured by the ion gauge) and a pyrometer temperature of 620°C for 30 min.[II] The Convergent Beam Electron Diffraction (CBED) patterns in the insets below stems from nanosize regions along the wire as shown. The relatively large ZB$_a$ and ZB$_b$ parts at the NW root are separated by a twin plane, which rotates the structure by 180 degrees around the wire axis. The pattern corresponding to the ZB$_a$/ZB$_b$ region reveals closely separated ZB$_a$ and ZB$_b$ parts and the density of twin planes is seen to increase as we move towards the tip. Finally, the structure keeps rotating at every mono layer which produces the small segment with the WZ structure. (B) A TEM image of a GaAs NW grown for 40 min with a V/III ratio of 8 (as measured by the ion gauge) and a pyrometer temperature of 635°C. The TPs appearing at the bottom and at the tip is a typical structural distribution for Ga-catalyzed GaAs NWs. The structural distribution depends on the relative size of the liquid phase (which changes during growth, see Figure 5-5) because it has a huge influence on the nucleation statistics, see section 3 and 5.1.

However, as a first approximation we will for simplicity neglect this dependence as well as adatom diffusion of As and contributions from the vapor states of the As species will be neglected (This just means that the V/III ratio is higher in the simulation as secondary adsorption effects is proportional to the beam flux of the material in excess, As). For all other parameters, the simulation shown in Figure 7-2 is based on the type of modeling presented in Chapter 4, where the relative size of the droplet in terms of the contact angle is shown as a function of the growth time (or nanowire length). Under these simulation parameters the nanowire diameter stays constant but the evolution of the liquid size is not monotonous.

Relating the structure to the relative size of the liquid as predicted in section 5.1, we would expect to be in regime II, where the probability of getting ZB structure is larger at larger contact angles and vice versa for WZ. Relating to the structural distribution in Figure 7-1 (A), we do not see the higher probability of forming WZ in the initial growth stage as predicted by the simulation. This can have many explanations, such as the contact is much larger at the very beginning, accumulation of material at small due to a large amount of parasitic growth in between the wires or maybe the wires characterized in the TEM have not been broken off at the root, ect. At least we cannot neglect the validity of the trend in the simulation as many growths seem to show a higher probability of forming WZ at the initial stages of growth as seen in Figure 7-1B and ref.[II,60].

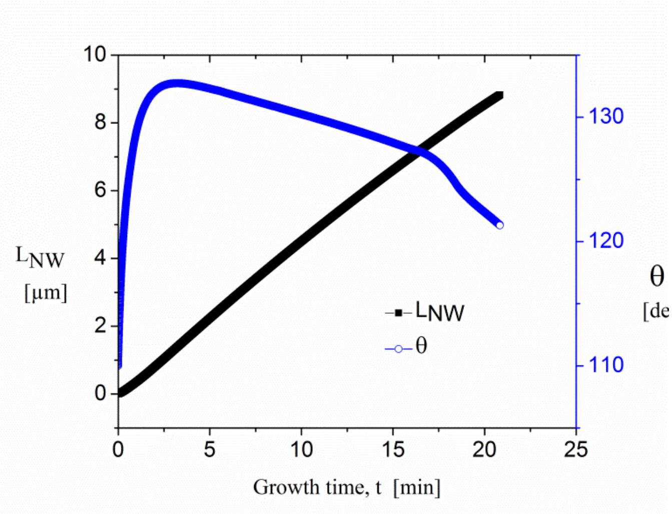

Figure 7-2. An example of a self-catalyzed GaAs NW growth simulation which uses the framework presented in section 4.1. It is here assumed that the initial contact angle is $\theta_{initial} = 110°$ with a nanowire diameter of 100 nm. Basic parameters; $\frac{f_{As_2}}{f_{Ga}} = 20$, $GR_{planar} = 0.3\frac{\mu m}{hr}$ and $T = 630°C$. The huge change in the relative droplet size at the initial growth stage is a typical trend in the simulation. This is because the conditions for collection of material changes rapidly in the beginning and because the wetting conditions change from substrate wetting to wetting at the top of a NW with vertical sidewalls.

To give an indication of the dynamical mechanisms determining the relative stacking probabilities and to check the assumption that the important parameter is the relative size and shape of the liquid phase, an in-situ X-ray diffraction experiment on growing NWs were performed at the SPring-8 X-ray synchrotron radiation source in Japan, see ref.[IV]. In-situ X-ray diffraction experiment on growing NWs is an experiment which is superior to a study using RHEED because it is possible to monitor even small changes in the amount of a given crystal structure during the complete growth cycle, and because X-ray characterization of NWs has already proven to be a powerful tool for determining their structure and shape[62,63]. For details on the experimental setup, see ref.[IV].

The growth temperatures used are approx. $T = 630°C$ and the Ga fluxes corresponding to $GR_{GaAs} \cong 0.1 - 0.3\frac{\mu m}{hr}$. Like in-situ TEM measurements[38], the growth has to be done without substrate rotation, which means that the side-walls which are not exposed to the direct beam are only stabilized due to the v states. It is expected that the WZ peak stems from NW growth only. A sketch of the in-situ growth characterization is illustrated in Figure 7-3, where a typical CCD image at a given time is also shown.

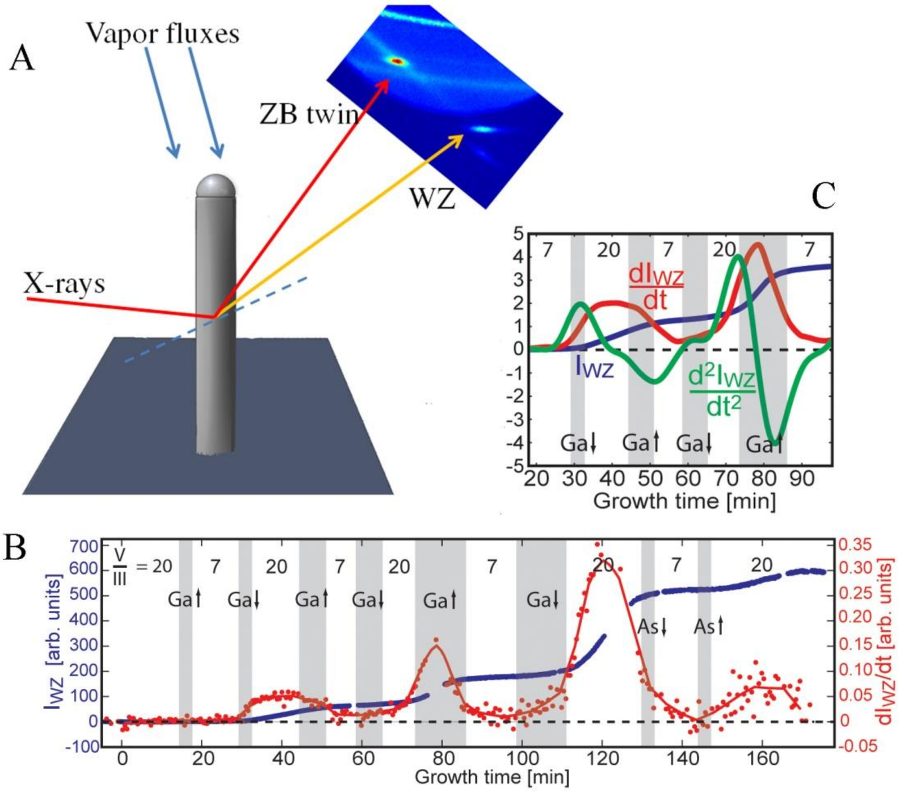

Figure 7-3. Growth 'A'. (A) Sketch of the in-situ X-ray diffraction characterization of ZB and WZ formation during NW growth. The diffracted x-rays are detected with a CCD camera and the relative intensities arising from scattering in different crystal planes are found by integrating around the pixels containing the corresponding Bragg peak. (B) WZ structure formation analysis of during 'growth A' using in-situ x-ray characterization. The blue points show the intensities of single images of the WZ [1 0 -1 1] Bragg peak, I_{WZ}, during the complete growth cycle. The red points give the corresponding gradients, which is a direct measure for the formation of WZ structure (the solid line is a guide to the eye). The grey regions indicates periods where the Ga flux is changed between V/III ratios of 7 and 20, except the last two changes, which were done with a corresponding change in the As flux. In (C), the green curve shows the derivative of the WZ formation, $\frac{dJ_{WZ}}{dt}$, which is measure of how the WZ formation rate, J_{WZ}, is changing.

The WZ formation rate during growth is presented for two independent growths '𝔄' and '𝔅' in Figure 7-3 (B) and Figure 7-4(A), respectively. In the first growth '𝔄', the Ga flux is changed linearly at different rates in periods indicated by the grey regions. The last two grey regions in '𝔄' indicate the time where the As flux was changed correspondingly at a fixed Ga flux. In growth run '𝔅', the rate of change of the Ga flux is the same in all regions, but an extended period with high group III flux was included. The growth details can be found in the supplementary information of ref[IV].

The gradient of the intensities (red curves in Figure 7-3 (B) and Figure 7-4 (A)) are measures of the WZ formation rate, J_{WZ}. It is observed that WZ is primarily formed when going from low to high V/III ratios, which could indicate that the growth takes place in regime II. However it is obvious that there is not a direct correspondence between the V/III ratios and the formation of WZ structure. The derivative of the , $\frac{dJ_{WZ}}{dt}$, is a measure of how J_{WZ} is changing during growth. If $\frac{dJ_{WZ}}{dt}$ is positive (negative), J_{WZ} is increasing (decreasing). In Figure 7-3(C), $\frac{dJ_{WZ}}{dt}$ is plotted for a period of growth '𝔄'. From this plot, it is seen that J_{WZ} is not directly correlated with the V/III ratio or total flux. Because the time needed for the adatom kinetics and liquid diffusion to reach quasi steady state conditions are much smaller compared to time scales of NW growth[64] liquid composition or liquid ordering is ruled out as the primary effect. Also changes in surface energies due to changes in vapor pressure or adatom concentration seem to play a minor role in this case. Thus, if these effects play a role on the growth structure evolution it must be in interplay with the shape of the growth interface region where the structure is formed. In growth '𝔅' we see the same trends as in '𝔄', but surprisingly we observed a decrease in the WZ peak intensity as seen in the midsection of Figure 7-4 (A). A decrease in I_{WZ} can be explained by either desorption of the WZ structure or a crystal phase transition to ZB structure.

Because it is difficult to explain desorption due to a higher Ga flux, we find it likely that a WZ-ZB phase transition has taken place under special conditions where the Ga droplet has exceeded a critical size. This is confirmed by post growth SEM and TEM analyses which show that there are two overall types of NW morphologies in this growth of approximately equal density. All analyzed NWs exhibit similar structure and morphology as shown in Figure 7-3 (B) and (C). The first types of NWs are the ones which are able to continue the axial growth under the complete growth cycle. They exhibit three WZ sections corresponding perfectly to the three periods of high WZ structure formation rate seen in the x-ray diffraction data. The second types are the ones in which the axial growth were terminated by a 'bulge' formation, seen in Figure 7-4(C). For these NWs we either see a much smaller WZ segment of the corresponding first segment as seen Figure 7-4 (B) or nothing at all, indicating that a crystal phase transformation has taken place during the 'bulge' formation under the following low V/III period.

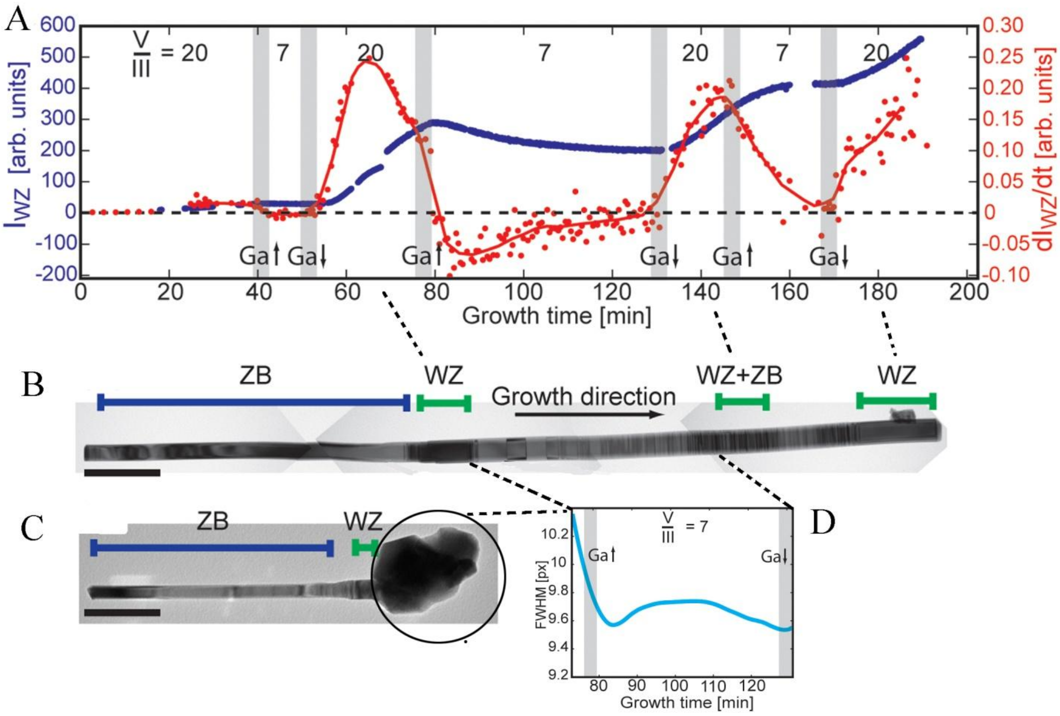

Figure 7-4. (A) WZ structure formation analysis of during 'growth B' using in-situ x-ray characterization. (B) and (C) TEM images of the two different types of NWs from the growth shown in Figure 7-3 C. The structure along the length was identified using Convergent Beam Electron Diffraction analysis. As seen in the straight wires (A) there are three sections with WZ structure, which corresponds to the three regions of high WZ formation in Figure 7-3 C. In Figure 7-3 C it is also seen that the amount of WZ is decreasing in the period $t_g \cong [80s:125s]$. From SEM and TEM images it is seen that approximately half of the wires had suffered from a bulge formation during the second increase in Ga flux. During this step the WZ structure formed prior to this step were most likely transformed into ZB. This is concluded because the WZ formation is negative during this step and because the segments are either much shorter or even absent in the 'bulged' wires. Scale bars are 500 nm. (C) shows the FWHM in units of CCD pixels which is an inverse measure of the average WZ crystal size during growth. It is seen that average WZ crystal size decreasing in a long period of time, consistent with the assumption of WZ to ZB phase transition.

Thus increasing the Ga flux very rapidly may lead to these ‘bulge’ morphologies, because a change in the effective V/III ratio can be too fast for maintaining axial growth conditions. It is therefore likely that the WZ structure formed in the previous period with high V/III ratio is transformed into ZB structure during the ‘bulge’ formation in the low V/III ratio period. This phenomenon is similar to the WZ to ZB transition during epitaxial burying observed by Ref. [65]. In Figure 7-4 (C) the FWHM evolution of the WZ peak is shown for the period including the bulge formation which takes place in the first V/III=7 period in the graph. As the FWHM is an inverse measure of the average size of the WZ crystal segments, the increase indicates that the WZ segments is getting smaller and the following decrease is where WZ segments start to disappear.

This is a strong indication that the dominating structure formed depends on the lowest free energy of the total liquid-solid interface region. This also indicates that the activation energy for reconstruction of the structure of during growth is relatively small, and that the structure formed by the nucleus is not necessarily the same as the final structure formed in the NW.

Thus in conclusion, many things indicate that the shape and relative size of the liquid phase play the dominant role on the crystal structure formation rates, consistent with the theoretical formulation and predictions.

8 Qualitative analysis of Be-doping mechanisms during axial and radial growth of self-catalysed GaAs nanowires

In order for NWs to become a technological reality and not only for photovoltaic applications, control of doping is very important. In this analysis we will study the Be doping mechanisms during axial and radial growth modes of self-catalyzed GaAs NWs. This chapter is based on the results which will be presented in paper IX.

We will distinguish between three main incorporation paths as shown in Figure 8-1;

1) Axial incorporation through the VLS mechanism
2) Radial incorporation through the VS mechanism
3) Interdiffusion, diffusion of carriers within the volume of the NW.

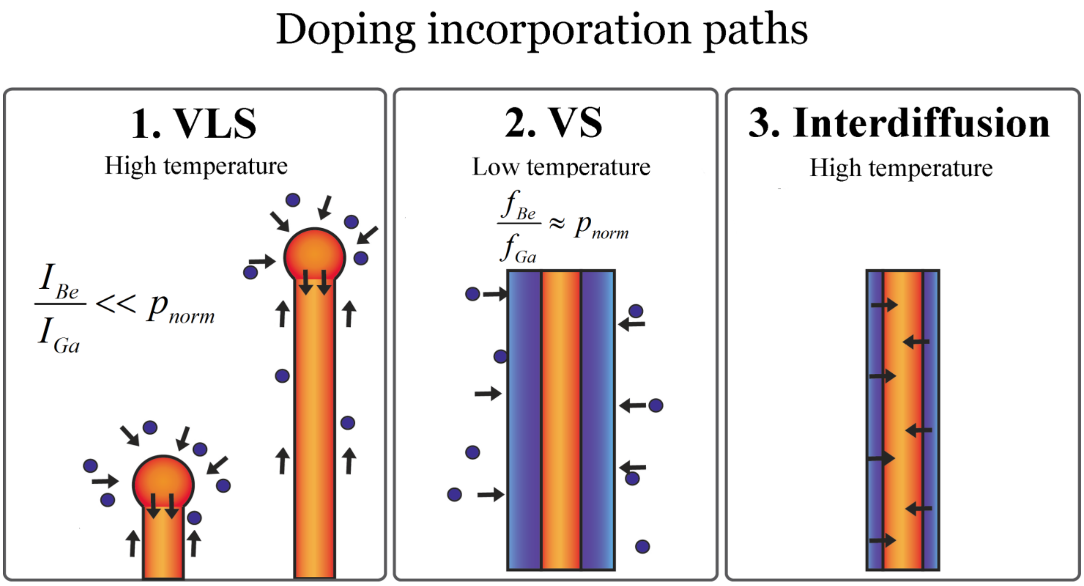

Figure 8-1. Three main dopant incorporation paths are considered in the analysis. 1) Incorporation through the droplet during the axial VLS growth. Under typical self-catalyzed GaAs VLS conditions the effective Be/Ga ratio at the growth interface is much lower than in the corresponding planar growth with the same beam flux ratios. 2) Lowering the temperature to radial VS growth conditions means than the diffusion length of Ga becomes smaller (see Chapter 6) and the doping levels should in principle correspond to the corresponding planar doping levels, if the angles ϕ_i of the incident beam fluxes of Be and Ga atoms are the same. 3) The third doping mechanism which is dominant at VLS growth temperatures and which cannot be neglected for Be doping is interdiffusion, leading to a more uniformly doped NW.

Doping incorporation through the VLS growth mode of III-V NWs is not well understood because, as we have seen in chapters 2-5, the growth kinetics of the involved elements are complicated and it does not become easier by introducing dopants as the relative ratio of elements towards the growth front depends strongly on the adatom kinetics.

Also doping via the radial VS growth mode is not necessarily straightforward as in the planar case, because of the nanostructured morphology. However, if the temperature is low enough and /or the pressure high enough such that $\lambda_{NW,i} << L_{NW}$ is fulfilled for both Be and Ga species, the doping level should correspond to the equivalent planar doping level if the orientations of the incoming beams are the same (see section 6.1 radial growth analysis). To give some insight into the Be incorporation mechanisms during axial VLS and radial VS growth of self-catalyzed GaAs nanowires, six different types of growths with varying doping profiles were carried out, see Figure 8-2. First we show that it is possible to fabricate good reliable ohmic contacts as seen in Figure 8-2 (A), which were achieved by using Pd/Ti/Au contacts followed by an annealing step. In Figure 8-2 (B) we show the apparent conductivities obtained from each growth using four-probe measurements to avoid contact resistance. We have carried out approximately 5 to 15 electrical measurements on each type of NW at room temperature, and an overview of the growth are listed in Figure 8-2 (C). All the contacts was drawn using the auto-contacting software presented in ref.[XV].

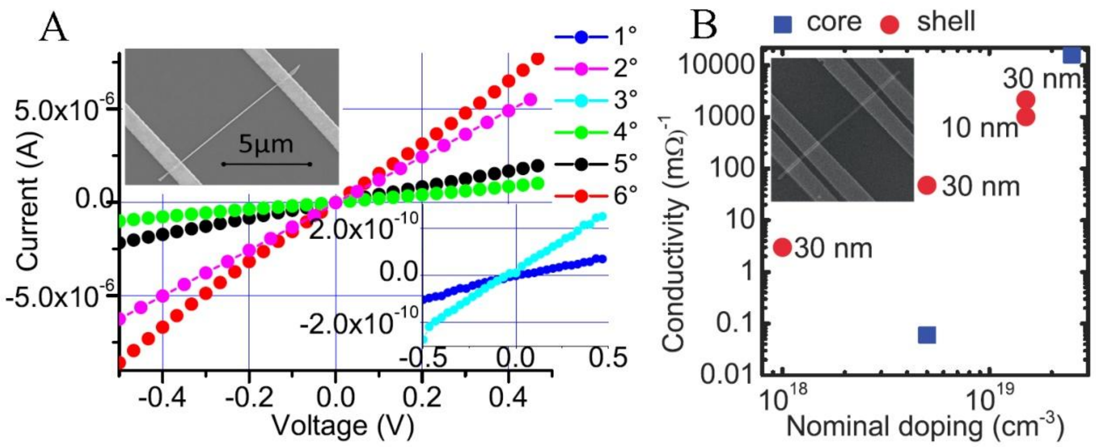

C

Growth no.	t_{ax} [min]	t_{rad}/Shell thickness [min]/[nm]	p_{norm} [cm^{-3}]	Apparent conductivity $(\Omega m)^{-1}$
1	30	0	$5\cdot 10^{18}$	0.06 ± 0.03
2	60	0	$2.5\cdot 10^{19}$	16000 ± 5000
3	45	30	$1\cdot 10^{18}$	3 ± 2
4	45	30	$5\cdot 10^{18}$	50 ± 20
5	30	10	$1.5\cdot 10^{19}$	1000 ± 600
6	30	30	$1.5\cdot 10^{19}$	2200 ± 500

Figure 8-2 (A) Electrical measurements performed on the six growths with two Pd/Ti/Au contacts, which are clearly ohmic due to the linearity of the curves. (B) The apparent conductivity is obtained from 4 point measurements (C) Table of the six growth analyzed in the section which all were grown with an equivalent planar growth rate of $GR_{Ga} = 0.27\frac{\mu m}{hr}$. The VLS growth step was grown for t_{ax} with a flux ratio of $\frac{f_{As_2}}{f_{Ga}} = 60$ and substrate temperature of $T = 630°C$, while the radial VS growth step was grown for t_{rad} with $\frac{f_{As_4}}{f_{Ga}} = 100$ and a substrate temperature of $T = 460°C$. Using the formula for radial growth rates (eq.(6.2)) under low NW densities we have that 1 min of radial growth corresponds roughly to formation of a thickness of 1 nm. The equivalent planar doping levels p_{norm} are calibrated from Be doped GaAs (100) substrates prior to growth with Hall bar measurements. The apparent conductivity σ_{app} is the mean conductivity measured from all the four probe contact configurations of the respective samples using eq.(8.1), and the uncertainty is the standard derivation. Only one device from growth number 2 has been measured, and uncertainty is a rough estimate. This figure is taking from ref.[IX]

The apparent conductivities σ_{app} are obtained from the classical Drude formalism, where the effective carrier concentration in the conducting region can be written as

$$p_{eff} = \frac{\sigma_{app}}{e\mu} \tag{8.1}$$

Here μ is the electron mobility, which has been measured at room temperature for self-catalysed GaAs NWs grown by MBE to be $\mu = 31\frac{cm^2}{V \cdot s}$.[66] σ_{app} is given by $\sigma_{app} = \frac{length}{R_{res} \cdot area}$, where R_{res} is the resistance extracted from the four probe measurements, $area$ is cross sectional area of the nanowire and $length$ is the distance between the conducting leads. Thus if we assume that the density of Be atoms incorporated during growth is equal to the density of carriers, then we can use eq.(8.1) to examine the Be incorporation during the different types of growth. However in the analysis and the correlation of doping mechanisms and electrical carriers we need to consider additional effects:

i) Surface depletion due to band bending

ii) The doping profile and how it is affected by interdiffusion of dopants during growth

Before we take account of these effects we look at the apparent conductivities of the core and the shell. The apparent conductivity obtained from the NWs of growth number 1 (which is a result of only 30 min of VLS growth) is extremely small as compared to the other types of growths. Comparing growth number 1 with growth number 4 which has been grown with the same conditions except an additional shell thickness of 30 nm in growth number 4, we can see a huge difference. If we separate the transport contribution due to the VLS step and calculate the apparent conductivity of the contribution from the VS step we get; $\sigma_{shell} = 50 \pm 20(\Omega \cdot m)^{-1}$ and an corresponding apparent shell doping concentration, $p_{shell} = (2 \pm 1) \cdot 10^{17}\, cm^{-3}$. Even though we have not taking account of surface depletion yet this indicates that the doping contribution due to the VLS step appears to be extremely low. This suggest that only a small amount of Be atoms are incorporated through axial growth and will therefore only contribute by a negligible amount to the conduction. This is not surprising as the NW growth rate is much larger than the corresponding planar growth rate, and it is unlikely that the overall kinetics of Be species is comparable with that of Ga species.

The band bending is due to a difference in Fermi levels between the surface oxide layer and the bulk. This forms a surface depletion region of an effective width *w*, which depends strongly on the doping concentration in the bulk. To find *w* we will use Poisson equation in cylindrical coordinates,

$$\frac{1}{r}\frac{\partial}{\partial r} r \frac{\partial \varphi(r)}{\partial r} = -\frac{e p(r)}{\varepsilon \varepsilon_0} \tag{8.2}$$

where $\varphi(r)$ is the electric potential, $p(r)$ is the density of carriers and ε and ε_0 is the dielectric constant and the permittivity of free space. The build-in potential Φ_{bi} which causes a depletion width around the surface depends on the doping concentration in the wire. However because the wires are generally highly doped the Fermi level E_f is close to the valance band level in the bulk $E_{V,bulk}$, and this difference will therefore be neglected for simplicity. This means we can use the value $\Phi_{bi} \approx E_f - E_{V,surf} = 0.5eV$ as found in ref.[67] for the relative surface potential. Solving eq.(8.2) using the boundary conditions of vanishing electric field in the NW center and the relative surface potential $\varphi\left(\frac{d_{NW}}{2}\right) = \Phi_{bi}$, one obtains an equation for the depletion layer width *w* which depends on d_{NW} and the doping concentration in the shell p_{shell},

$$-w^2 + d_{NW} w - 2\left(\frac{d_{NW}}{2} - w\right)^2 \ln\left(\frac{d_{NW}}{d_{NW} - 2w}\right) = \frac{4\varepsilon\varepsilon_0 \Phi_{bi}}{e \cdot p_{shell}} \tag{8.3}$$

where it is assumed that $p(r) = p_{sur}$ throughout the wire. This is in principle only a reasonable approximation as long as the shell thickness is larger than w. This means that eq.(8.3) is not a good approximation at low doping levels and thin shells, but still it will keep the qualitative trend under these conditions. The actual doping profile in the NWs depends on the interdiffusion processes during growth. Now, Be incorporation via the sidefacets during axial and radial growth takes place via two different mechanisms. Interdiffusion of Be atoms during high temperatures are known to be significant in GaAs[68], see Figure 8-3. Thus, during axial growth there will be a concentration of Be adatoms on the NW sidewalls which will not only move around in the adatom state but also diffuse into the NW volume by interdiffusion. According to section 2.2 there are three main diffusion routes for an adatom; surface diffusion (*aa*), desorption (*av*) and incorporation (*as*). The *as* mechanism can further de divided into two types of incorporation mechanisms; incorporation due to radial growth at an incorporation site or by interdiffusion which can take place at all sites. If radial growth is neglected we can write the mean length displacement of a Be atom in the adatom state according to eq.(2.16) as,

$$\lambda_{NW,Be} \cong \sqrt{\bar{Z}'_{aa,Be} {l_a}^2 \exp\left(-\frac{\delta h^{TS,ERS}_{aa,Be}}{k_B T}\right)\left(\bar{Z}'_{as,Be} \exp\left(-\frac{\delta h^{TS}_{as,Be,\text{int}}}{k_B T}\right) + \bar{Z}'_{av,Be} \exp\left(-\frac{\delta h^{TS,ERS}_{av,Be}}{k_B T}\right)\right)^{-1}} \tag{8.4}$$

where $\delta h^{TS}_{as,Be,\text{int}}$ is the enthalpy barrier for interdiffusion. Now because our results suggest that $\lambda_{NW,Be} << \lambda_{NW,Ga}$, the life of the majority of the Be adatoms end either in an *as* or *av* state transition and not at the *ls* region. This means that we only need to look at the ratios between the two types of transitions, $\Delta\Gamma_{as,Be}$ and $\Delta\Gamma_{av,Be}$. It has not been possible to find measured or calculated activation enthalpies for desorption of Be adatoms on GaAs surfaces but the activation enthalpy for interdiffusion of Be in GaAs[68] is comparable to desorption enthalpies found from DFT calculations of other components[69,70]. Thus it is reasonable to assume that at least a non-negligible fraction of the Be adatoms diffuse into the volume of the NW due to the concentration gradient. This means that $\Delta\Gamma_{as,Be,\text{int}}$ is positive during growth but decaying as the Be concentration increase in the NW. However due to the fast time scale of adatom kinetics it is reasonable to assume that the Be concentration in the vicinity of the NW surface $p_{sur,Be}$ is kept at a quasi steady state concentration due to the constant incident Be flux. The interdiffusion process can be described by Fick's second law in cylindrical coordinates $\frac{\partial p(r,t_g)}{\partial t} = \frac{1}{r}\frac{\partial}{\partial r}\left(r\frac{\partial p(r,t_g)}{\partial r}\right)$ where it is assumed that the boundary conditions are independent of ω and z. The exact solution is given in ref.[71]. However on the level of accuracy in this study it is sufficient to solve the one dimensional Fickian diffusion equation assuming a semi-infinite medium, the Be concentration profile in the NW can be written as

$$p(r,t_g)=p_{sur}erfc\left(\frac{\frac{d_{NW}}{2}-r}{2\sqrt{D_{Be,\mathrm{int}}t_g}}\right) \tag{8.5}$$

where t_g is the diffusion time with an inter-diffusivity $D_{Be,\mathrm{int}}=0.655\exp\left(-\frac{2.43eV}{k_BT}\right)$,[68] and $erfc$ is the complementary error function. The low temperature shell growth is carried out at a substrate temperature of $T=465°C$, where the diffusion of Be is negligible, see Figure 8-3 (A).

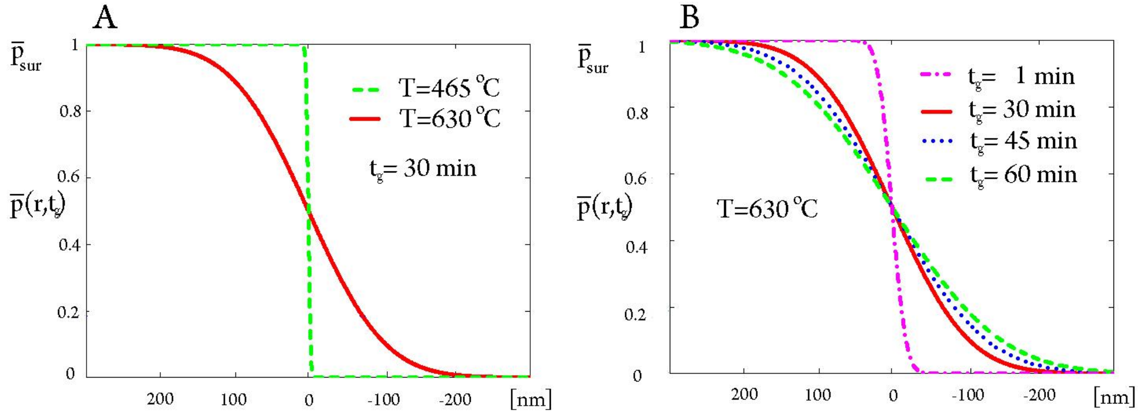

Figure 8-3. Interdiffusion of Be around a junction between a Be-doped GaAs and a undoped GaAs material. A) For typical growth times diffusion of Be inside the material can be significant during the VLS growth step, while it is negligible during the radial shell growth. B) The effect of growth time on the Be interdiffusion during the VLS growth step is high, especially during the first period of growth. This means that the doping density arising from the interdiffusion mechanism is reasonably uniform even though it has more time to diffuse at the NW root.

Thus after the complete NW growth the doping profile takes on a form as illustrated in Figure 8-4 (A), and can be written in the simple form,

$$p(r,t_g)\approx\begin{cases} p_{sur}erfc\left(\frac{\frac{d_{NW}}{2}-r}{2\sqrt{D_{Be,\mathrm{int}}t_g}}\right) & Core \\ p_{sur} & Active\ part\ of\ shell \\ 0 & Depletion\ region \end{cases} \tag{8.6}$$

Since the 4 point measurements are performed in the center of the nanowire, it is assumed that the interdiffusion took place half of the full VLS growth time even though it does not play a huge role as seen in Figure 8-3 (B). We integrate over the full NW cross section and include the depletion region as described by eq.(8.3). This enables us to deduce the doping concentration and electrical carrier concentration from the electrical measurements see Figure 8-4 (B).

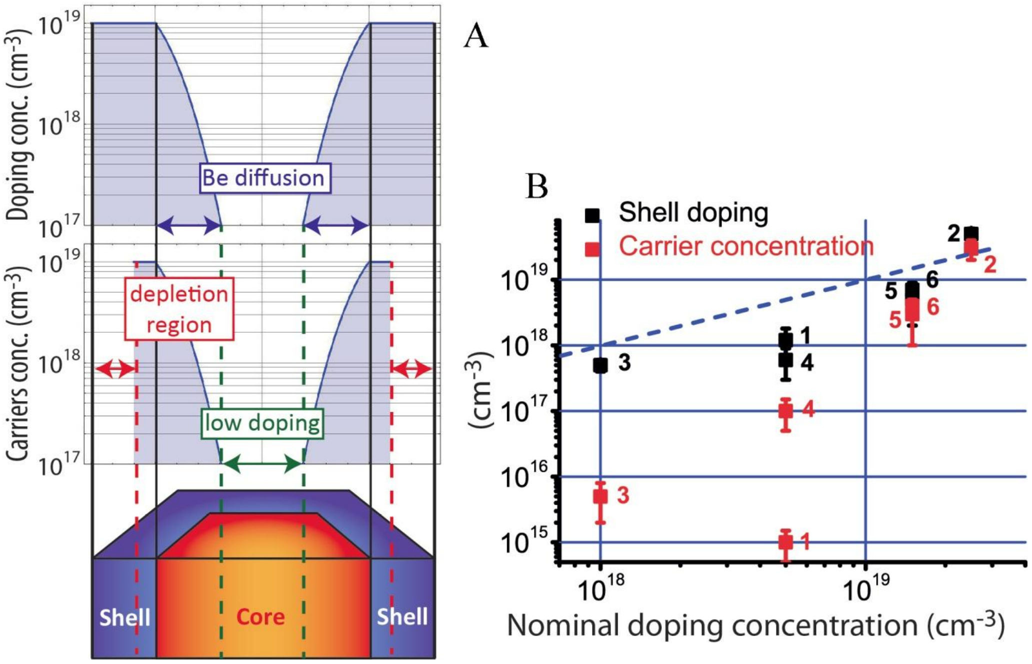

Figure 8-4. (A) Illustration of a cross sectional dopant distribution in the core-shell NWs. The doping and the carrier concentration are analyzed as a function of *r*. The Be concentration near the NW surface during VLS growth is here taken as the nominal doping concentration. (B) Comparison between apparent carrier density concentration (red) and calculated doping concentration in the shell (black). The blue dotted line represents nominal doping concentration. The error bar reported for every dots represent only the standard deviation calculated on the electrical measurements. Note that the calculated values for growth number 1 and 2 without shells have been calculated using eq.(8.3) which assume a shell with constant doping concentration. This means that there are some additional uncertainties related to these values. This figure is taking from ref.[IX].

For doping concentrations $< 5 \cdot 10^{18}\, cm^{-3}$ the depletion region is larger than the shell thickness. This concerns growths number 1, 3 and 4. These three growths exhibit a very low apparent conductivity. By taking the depletion region at the surface into account, the doping concentration at the shell is as predicted very close to the nominal doping concentration. For higher doping concentrations, the depletion region reaches few nm's and affects much less the overall apparent conductivity. It is interesting to note that even though the incorporation of Be via the VLS mechanism is negligible, it is possible to dope the NWs almost homogeneously during axial growth provided the Be flux is high. For nominal doping concentration $> 2 \cdot 10^{19}\, cm^{-3}$ the highly doped shell and the long growth time results into a strong diffusion of Be inside the core leading to an almost fully doped nanowire.

9 Single GaAs nanowire photovoltaics

This chapter is concerned with the growth and characterization of single nanowire solar cells with a radial p-i-n core-shell structure. These NWs are first grown with a p-doped core in a two step growth procedure as described in section 8. Hereafter the growth temperature is lowered and the As flux is increased for radial growth conditions, growing first an intrinsic (*i*) region (undoped) followed by a n-doped region, see Figure 9-1(A). A solar cell device needs a build-in electrostatic field to separate the electrons and holes generated from the incoming photons, and to extract the energy of the photons into electric work. Such a build in potential is established in semiconductors when a p-type material is brought together with a n-type material, because the respective p and n carriers diffuse across the p-n junction leaving ionized atoms on either side, as shown in Figure 9-1(B). The space charge sets up an electric field which prevents further (net) diffusion across the junction and an equilibrium state is established with a build in potential. Only an applied bias voltage or incoming photons can change this. If the energy of a photon is transferred to an electron in the valence band it will have energy enough to create an exciton (electron-hole pair) if the photon energy is higher than the band gab. But only in the depletion region (in the region where the bands bend) will efficiently separate the electron and hole before recombination.

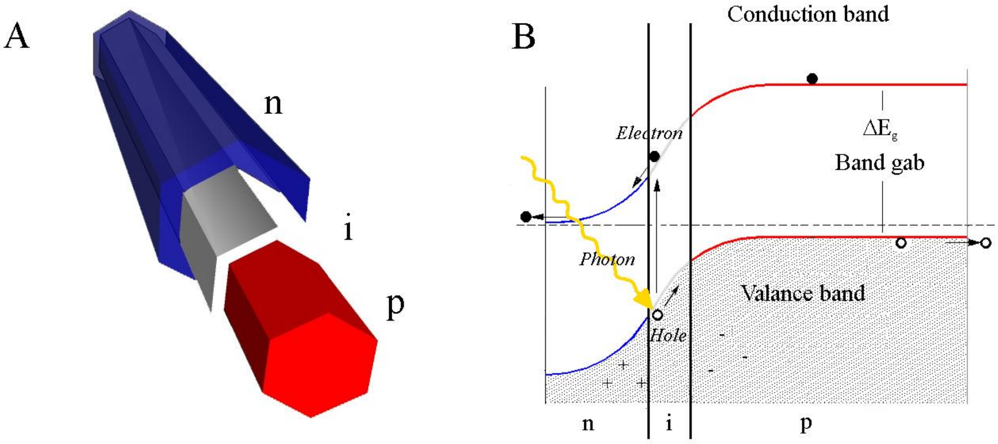

Figure 9-1. (A) Illustration of the core-shell p-i-n NW structure. (B) Illustration of the potential landscape for the electrons in the presence of a p-i-n junction. Photons with energies higher than the bandgab can create an electron hole pair which will be separated in the region where the bands bend and thereby contributing to the electric current.

The solar cell efficiency η_{eff} is defined to be the fraction of the total incoming sun power hitting the device, which is generated at the maximum power point by the device. The maximum power point is defined to be at the voltage where the device has the maximum performance, i.e. the maximum value of voltage times current. This can be written as $I_{sc}V_{oc}FF$, where I_{sc} is short circuit current (at zero bias), V_{oc} is the open circuit voltage (at zero current) and FF is the fill factor describing the 'squareness' of the curve. Thus if the projected area of the solar cell device towards the sun is A_{pj} and the sun power density is P_{sun}, the efficiency is given as, $\eta_{eff} = \frac{I_{sc}V_{oc}FF}{A_{pj}P_{sun}}$.

However for nanostructures light absorption is a complex phenomenon, with a strong dependence on the nanowire dimensions and absorption coefficient of the raw material.[72,73,74,75] When the NW diameter are smaller than or comparable to the radiation wavelength, optical interference and guiding effects play a dominating role on the reflectivity and absorption spectra. For highly absorbing semiconductors (such as direct bandgap, GaAs) exhibit resonances that increase the total absorption several-fold. Nanowires lying on a substrate also exhibit such resonances, often described by Mie theory.[76,77,78] This means that when the solar cell efficiency is measured on a single nanostructure using the classical formula for efficiency with the physical apparent projected cross section A_{pj}^{app}, it should be thought of as an apparent efficiency,

$$\eta_{eff}^{app} = \frac{I_{sc}V_{oc}FF}{A_{pj}^{app}P_{sun}} \tag{9.1}$$

which is a relative measure of the NW solar cell performance. Assuming that the shunt resistance in the device is high the open circuit voltage can be approximated as[79]

$$V_{oc} \approx \frac{nk_BT}{e}\ln\left(\frac{I_{sc}}{A_{pn}J_0}+1\right) \tag{9.2}$$

where n is the diode ideality factor, e is the elementary charge and J_0 is the reverse saturation current density. J_0 is a measure of the carrier recombination in the neutral regions on either side of the junction. In eq.(9.2) it is seen that a smaller A_{pn} for a given I_{sc} gives a higher open circuit voltage and therefore a higher efficiency in eq.(9.1). This is the drawback for NW solar cells with radial pin junctions because A_{pn} is relatively large. However the advantage of radial junctions is that it is easier to cover the NW volume with an effective depletion region and the quantum efficiency and I_{sc} is therefore higher. If we assume that J_0 is independent of I_{sc}, eq.(9.2) can be written as

$$V_{oc} \approx V_{oc}^{macro} + \frac{nk_BT}{e}\ln\left(\frac{P_{NW}}{P_{macro}}\right) \tag{9.3}$$

Here V_{oc}^{macro} is the open circuit voltage under a light concentration of 1 sun in a corresponding macroscopic device with a mean effective light power density P_{macro}, as predicted from the Lambert-Beer law, and P_{NW} is the mean effective light power density inside the NW (as described by for example Mie theory). The apparent efficiency can therefore be written as[79]

$$\eta_{eff}^{app} \approx \eta_{eff}^{macro}\left(1 + \frac{nk_BT}{eV_{oc}^{macro}}\ln\left(\frac{P_{NW}}{P_{macro}}\right)\right) \tag{9.4}$$

where η_{eff}^{macro} is the efficiency in a corresponding macroscopic planar device under one sun. Thus, because of the strong light absorption resonance effects in GaAs NWs they can act as natural light concentrators, which can lead to increased efficiencies of macroscopic solar cells based on nanowires. The perfect nanowire based solar cell would therefore consist of an axial p-n junction if the overall internal quantum efficiency is as high as for the 'radial' device. This may be achieved by using the right doping levels and optimising the cell in terms minimizing surface recombination rates with the use of surface passivation, as shown in section 9.3. In the following sections we will examine the photovoltaic characteristics and especially the light absorption properties of lying and standing self-catalyzed GaAs NWs.

9.1 Growth, fabrication and characterization of single lying p-i-n core-shell nanowires

In 2009 Colombo et al.[80] reported on I-V measurements on single lying GaAs p-i-n NW structures where both the p and the n part were doped with Si. This is possible because Si typically p-dope under VLS growth (Ga rich conditions) and n-dope under VS conditions (As rich conditions). They obtained an apparent efficiency of $\eta_{eff}^{app} = 4.5\%$ using eq.(9.1). Here we will follow the approach by Colombo et al. and make I-V characterization on the same type of wires, however with slightly different NW dimensions and doping concentrations and where the p-core is doped with Be.

The Be-doping study presented in Chapter 8 was unfortunately not carried out before a long growth series of core-shell p-i-n NWs structures were done, however optimizing the structures will be easier for the next series of growths. The apparent efficiency was tried measured on several different types of NW solar cell devices, but only very few successfully contacted wires were achieved. This could be due to problems contacting the p part (mainly due to difficulties in the etching step of the shell) because many showed ohmic behaviour (conductance through the n-shell). The few devices which showed diode behaviour had apparent efficiencies of no more than around $2-3\%$, and it was not been possible to get enough data to present a serious study on efficiencies as a functions of growth conditions and nominal doping concentrations. Fortunately before the results of chapter 8 were known, a growth was tried where the p-part was grown two steps, an axial and radial step. It turned out that this type of growth was not only easier to contact but also of extremely good quality. They have been used for many different photovoltaic applications, such as an electrically driven point light source in forward bias[XIV], for single lying solar cell (section 9.2) and for advanced light absorption experiments[XII] (section 9.4). The growth and fabrication of these devices in outlined below.

First the VLS growth step was carried out with a nominal Ga growth rate of $GR_{Ga} = 0.27\frac{\mu m}{hr}$, for 45 min, at T=630°C and V/III ratio of 60. The p-doping is achieved with a beryllium flux corresponding to a nominal level of $3.5\text{x}10^{19}$ atoms/cm^3. The diameter of the core is about 120 nm. After the growth of the doped core, the MBE conditions are switched from axial to radial growth: the substrate temperature is lowered down to 460°C, the As source is switched from As_4 to As_2, the V/III ratio increased to 150. Under these conditions the radial growth rate is approximately $\sim 1\frac{nm}{\min}$ for relatively low NW densities and short diffusion lengths, according to section 6.1. The radial growth step started with 5 min of radial p-doping followed by 30 nm growth without any intentional impurity to create an intrinsic layer. Finally a 60 nm n-doped shell is grown using Silicon as a dopant, with a nominal concentration of $5\text{x}10^{18}$atoms/cm^3. The overall diameter of the final structure is about 300 nm while the length is approximately 10 µm.

After growth the wires were removed from the growth substrate by sonication in isopropanol and drip dried onto strongly p-doped Si(100) substrates covered with 500nm thermal SiO_2 and pre fabricated alignment marks. The contact to the p-doped core was defining using e-beam lithography followed by a 45-60s etch at room temperature in citrid acid to etch away the n and i part. Metal evaporation of 5nm Ti followed by 200 nm Au is deposited on both the p and n-part. The contacts were annealed for 2min at 300°C in a N_2 atmosphere. In Figure 9-2 (A) a SEM image of the ready device is shown.

Before carrying out photovoltaic measurements on such structures it is necessary to ensure that it is the p-i-n junction which generates the photocurrent and not a Schottky diode at the metal-NW interface. To check this, a device was loaded on a moveable stage in a Laser setup with spot size diameter of approximately 2 µm, and then a scan along the length was performed.

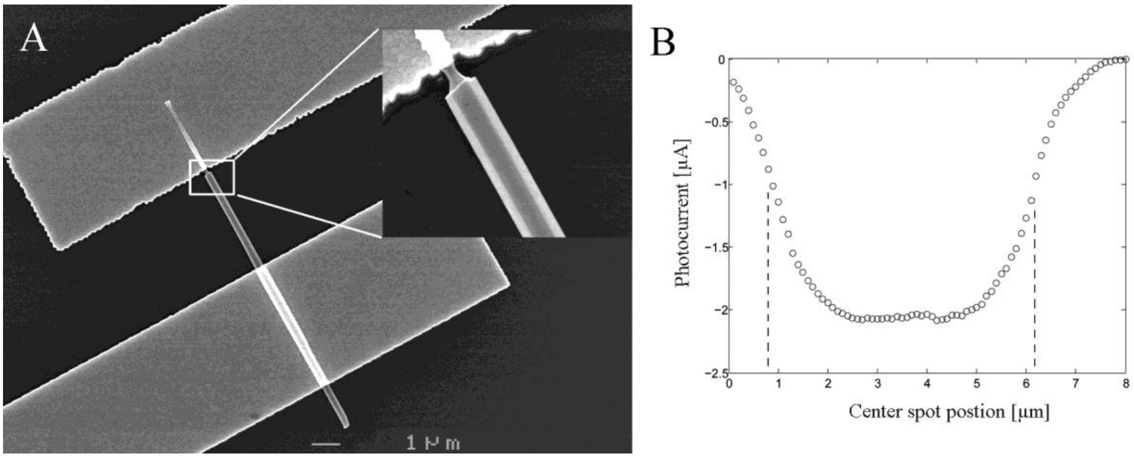

Figure 9-2. (A) A SEM image of a p-i-n GaAs NW contacted by two Au electrodes. To get in contact with the p part the n and i part was selectively etched around one contact, as seen clearly in the inset. (B) Laser induced photocurrent mapping was carried out along the length of the NW. The dotted lines indicate the position of where the contacts starts, revealing a spot size diameter of approximately 2µm. It is seen that the laser induces a photocurrent when above the bare NW and completely disappears when it moves across of the contacts.

In Figure 9-2(B) it is clearly seen that if there should be any positive contributions to the photocurrent from a possible Schottky junction, it is negligible (see figure text). Moreover the p-i-n junction along the length seems to be nice and uniform in the region selected.

To check the efficiencies of the NW solar cells the solar illumination was done with a standard solar simulator (LOT – Oriel 150W Xe lamp) with a 1” beam diameter and an AM1.5G filter. The 1-sun intensity was verified using a mono crystalline silicon solar cell calibrated at Radboud University Nijmegen against an NREL secondary cell standard.

9.2 I-V Characteristics of single lying GaAs pin junction solar cells, $\eta_{eff}^{app} = 11.5\%$

The *I-V* characteristics of six different wires from this growth are presented in Figure 9-3. They are characterized individually by measuring I-V curves in the dark and under AM1.5G and 2.5 times AM1.5G illumination. Under AM1.5G illumination we see that the apparent efficiencies 6.6%-11.5% are considerably higher than the best results previously reported for lying single NW solar cells[80,81,82]. However, comparing with state of the art GaAs planar solar cells[83], it is still much lower in terms of the FF and V_{oc} (It is difficult to compare the efficiencies due to the size-effects mentioned above). The main reason why it is difficult to obtain a high V_{oc} in NW solar cells with a radial p-n junction is most likely because of the large value A_{pn} in eq.(9.2). Thus in this sense an axial junction would be more efficient because A_{pn} would only be the cross sectional area of the wire. However, if light absorption takes place far from the junction (in the flat region in Figure 9-1B) the generated electron-hole pair might recombine with themselves or with other exiting defects such as the surface before being separated by the build-in electric field and therefore not contributing to the photocurrent.

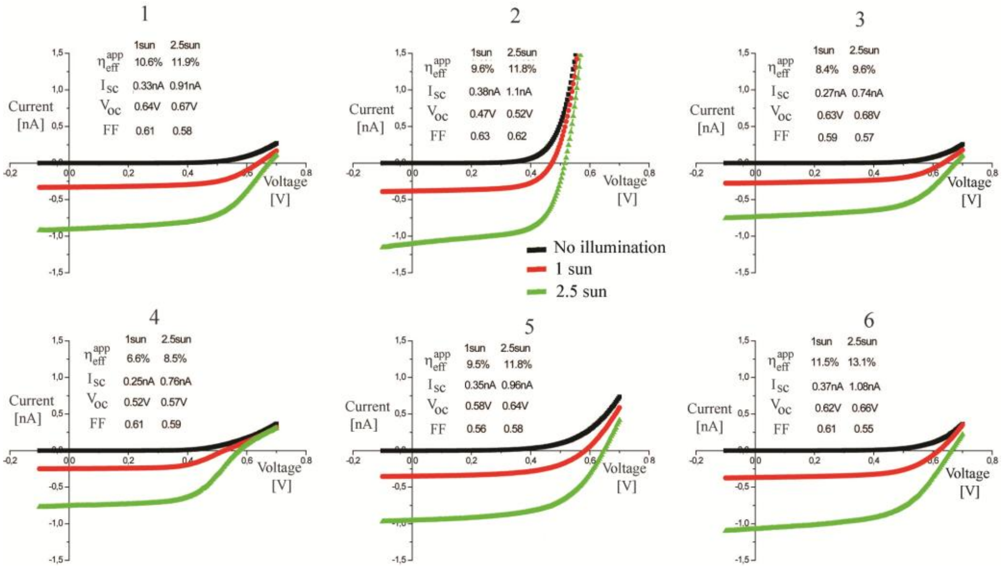

Figure 9-3. I-V measurements on six different lying NW solar cell devices originating from the same NW growth under dark, 1 sun (AM1.5G) and 2.5 suns illumination. Comparing with planar cells the V_{oc} is relatively low as predicted of radial junctions, however it is compensated by a high I_{sc}, due to the efficient light absorption. The apparent efficiency of 11.5% is to our knowledge the highest value reported for lying single NW solar cells.

9.3 The effect of higher bandgab and surface passivation on lying GaAs$_{1-x}$P$_x$ pin junction solar cells, $\eta_{eff}^{app} = 10.2\%$

This section is based on the results presented in ref.[XIII]. There can be many ways to increase V_{oc}, such as making A_{pn} smaller or increasing P_{NW} through optimizing the NW dimensions and solar cell design. However it is also possible increase V_{oc} by increasing the bandgab of the material. One way to increase the bandgab of the GaAs NWs is to form a ternary alloy by adding Phosphorus to the NWs. If the silicon substrate is used as a bottom cell in a dual-junction Si/GaAs$_{1-x}$P$_x$ solar cell the theoretical 1-sun peak efficiency is predicted to be with a 1.7 eV bandgap top cell[84,85]. This corresponds to a top cell consisting of GaAs$_{0.8}$P$_{0.2}$. A relative uniform composition with $x \approx 0.2$ along the NW length is achieved through a detailed growth study presented in supplementary information to ref.[XIII]. The I-V characteristics of lying GaAsP NW solar cells show the effect of surface passivation leading to an increase in I_{sc} and especially V_{oc} and *FF*, see Figure 9-4.

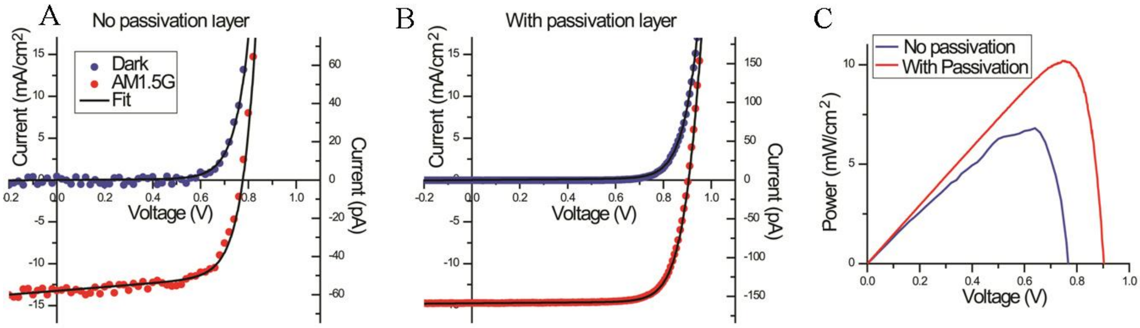

Figure 9-4. Characterization of single lying GaAs$_{0.8}$P$_{0.2}$ NW solar cells with (A) and without surface passivation (B). The I-V characteristics is shown under dark and AM1.5G illuminated conditions of the unpassivated and passivated SNWSCs with the highest efficiency of the sample. It is seen that not only the solar cell characteristics are improved but the current seems also much more stable for the passivated samples. (C) P-V comparison between the best passivated cells (P_{max} = 10.2 mW/cm^2) and unpassivated cells (P_{max} = 6.8 mW/cm^2). The figures are taking from ref.[XIII].

Since NW solar cells have a high surface to volume ratio, it is critical to passivate the sidefacets, i.e. stopping charge carriers from reaching the surface and recombining with surface states. By growing an additional shell of 5nm highly n-doped InGaP it is possible compare surface passivated and un-passivated solar cells. Since the rate of surface recombination typically increases rapidly with bias, introducing a surface passivation layer should give a large increase in V_{OC}, and only a small increase in I_{SC}, which is precisely what is observed in Figure 9-4. The combination of higher bandgap and surface passivation makes it possible to achieve a much higher V_{oc} than in the unpassivated GaAs samples in section 9.2.

9.4 Light absorption effects in lying GaAs pin junction solar cells covered with Ag nanoparticles

This section is based on the results presented in ref.[XII]. The resonant optical phenomena which were predicted by Mie in the case of spherical particles in 1908,[86] is the main reason why light absorption in III-V nanostructures cannot be described by the usual Lambert-Beer law. The high refractive index of GaAs NWs forms a cavity in which the light can circulate by multiple total internal reflections from the boundary often referred as leaky mode resonances.[87] In NWs these leaky modes can be modified by the interaction with the metal particles, and in the case of NWs decorated with metallic particles, we show in ref.[XII] how the symmetry of the wire and the particle modes plays a critical role in the optical interaction between these objects. For this reason P_{NW} can be affected in different ways, with enhancement, suppression or shift in the resonant position and intensity. The light absorption were investigated by measuring the photocurrent as a function of laser position, see Figure 9-5. As the distance between the contacts is about 7 µm with a 2 µm long array of nanoparticles in the middle and the laser spot is about 1.5 µm, we can distinguish between regions with and without particles. For details on the experiment setup see ref.[XII]. Spectral photocurrent measurements on NWs from the same batch as presented in Figure 9-3, but with the presence of metal particles positioned with high accuracy on the topfacets, were performed and analyzed. Typical photocurrent maps of a device at different wavelengths are shown in Figure 9-5(B). It is seen that for certain wavelengths, the metal particles induce an increase in the NW light absorption, while for other wavelengths the presence of the nanoparticles reduces the absorption in the NW. At other wavelengths no observable changes can be detected.

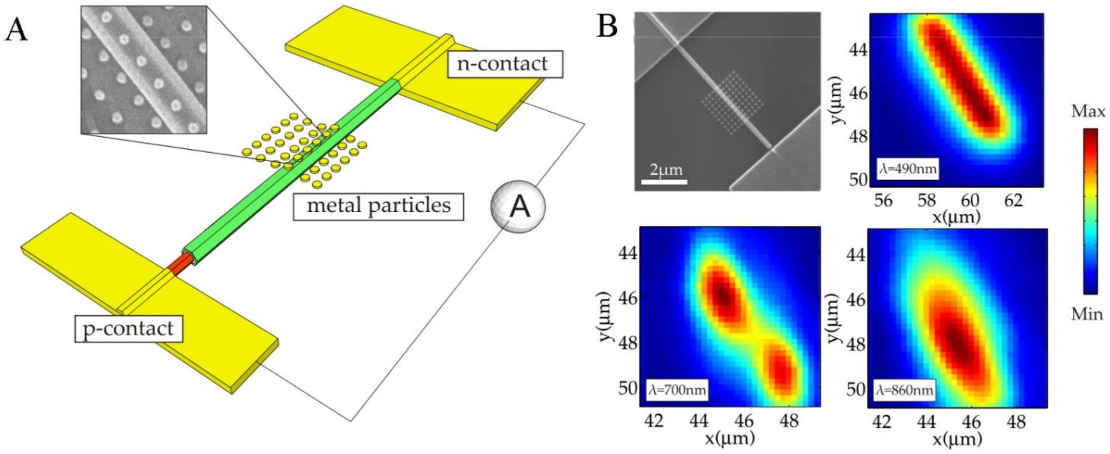

Figure 9-5. (A) Illustration of a p-i-n junction GaAs nanowire (NW) where the top facet is covered with a row of Ag nanoparticles. (B) As in Figure 9-2(B), the I_{sc} is measured as a focused laser beam is scanned over the structure shown in the SEM image at the top left corner of the picture. The other images show examples of photocurrent maps (x and y are spatial coordinates while the color map represents the intensity of the measured short circuit current) with all the possible effects induced by the metal particles: absorption suppression at λ=700nm, enhancement at λ=860 and no apparent effect at λ=490nm. This figure is taking from ref.[XII].

Lying NWs can exhibit enhanced absorption due to excitation of transverse electric (TE) and transverse magnetic (TM) resonances normal to the wire axis, which are of similar magnitude and similar in nature for NWs with $d_{NW} \geq 200nm$.[XII]

Assuming an infinitely long cylinder, the excitation of leaky modes can be predicted analytically as a function of the dielectric constant and wire diameter by analytically solving Maxwell's equations with appropriate boundary conditions, using a full-field finite-difference frequency-domain (FDFD) simulation.[88] Using this approach the exact hexagonal geometry of the NW can be precisely considered. Figure 9-6 shows FDFD simulated absorption efficiency maps as a function of wavelength for d_{NW} in the relevant range, for NWs lying on a semi-infinite SiO_2 substrate.

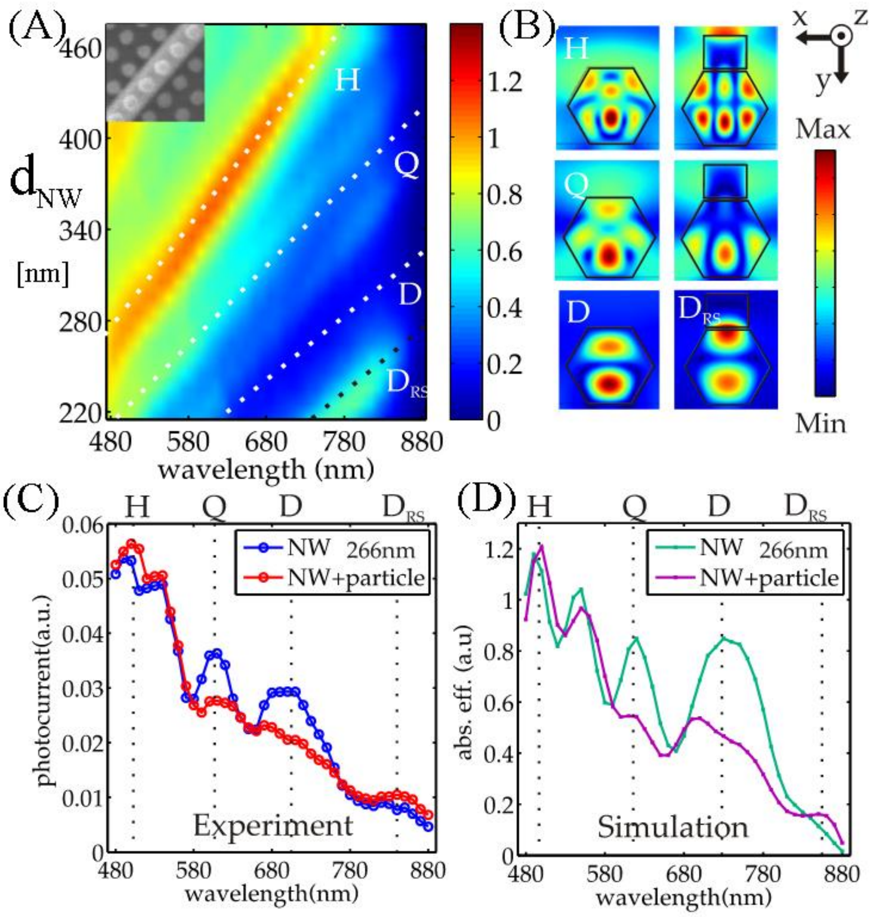

Figure 9-6. (A) Simulation of the absorption efficiency for a NW with metal particles deposited topfacet with respect to the nanowire diameter and incoming wavelength of the laser light. The different letters label the resonant modes of the nanowire: H-Hexapole, Q-Quadrupole, D-Dipole, D_{RS}-Dipole Red Shifted; (B) Plots of the absolute value of the magnetic field along the NW axis. The left column shows the field patterns in a NW with $d_{NW} = 266\,nm$ obtained without Ag particles for the different resonant modes while in the right column shows the modification of these patterns by the Ag particle. (C) Photocurrent as a function of the incoming wavelength for a bare nanowire and for a nanowire with a particle (red), which is seen to be very consistent with simulations of absorption efficiency in (D). This figure is taking from ref.[XII].

The dashed white lines in the picture refer to the occurrence of the resonant modes. The labels D, Q and H are used to name the resonances involved, they stand respectively for Dipole, Quadruple and Hexapole, from the number and symmetry of the maxima of the electromagnetic field involved in the resonance, see Figure 9-6(B).

9.5 Fabrication and characterization of single vertical p-i-n core-shell nanowires as grown on Silicon (111), $\eta_{eff}^{app} = 40\%$

As shown in eq.(9.4) the solar cell efficiency depends on the light intensity inside the NW. This section is based on the work presented in paper [XI], and will show that the configuration of standing NWs act as effective build-in light concentrators under one sun and can therefore potentially raise the solar cell efficiency limit. In order to fabricate such a device a detailed fabrication procedure needs to be carried out. A rough sketch of the 4 main steps of the solar cell device fabrication are shown in Figure 9-7, each of which are described in detail below.

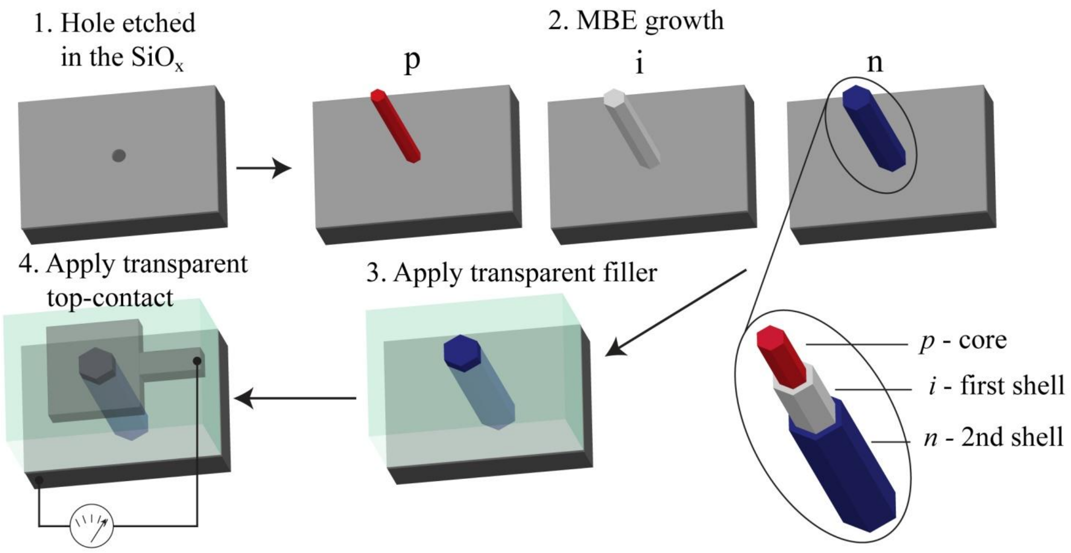

Figure 9-7. Sketch of the main steps of the NW solar cell fabrication described in detail above.

1) A heavily p-type doped silicon 111 substrate with a layer of 30 nm thermal SiO$_x$, is used to predefine positions for single GaAs nanowire growth. This is done by opening small holes in the oxide with a diameter of about 50-70nm using e-beam lithography and BHF etch. To locate the NW positions larger alignment markers with a certain relative coordinate are also defined, as shown in Figure 9-8.
2) The GaAs NWs are grown in a MBE chamber, where the axial core growth where grown by a 60 min Ga assisted vapor-liquid-solid growth mechanism at a temperature of $T = 630°C$. During this step the Be shutter was open in order to obtain a p-type inner core in connection with the p-type substrate through interdiffusion as explained in Chapter 8. As seen in section 4.2 due to the high desorption rate of both Ga and As on the oxide layer, the Ga rate needs to be high which for these growth are given by a

corresponding planar growth rate of $\sim 0.9 \mu m / hr$, and with a beam flux ratio (as measured by an ion gauge) of ${}^{V}\!/_{III} \sim 4$. As the diffusivity and desorption rate of Be on the thermal oxide surface is unknown, we cannot directly use the results obtained in chapter 8 and the doping levels in the core is uncertain. We therefore finished the p-part of the cell with radial growth step at $T = 460°C$ with a corresponding planar growth rate of $\sim 0.3 \mu m / hr$, and with a beam flux ratio of ${}^{V}\!/_{III} \sim 50$, followed by an annealing step to interdiffuse Be atoms into the core in order to ensure that the p-part is doped enough. During core growth of the solar cell sample the corresponding planar doping levels of the p-part was: $3.5 \times 10^{17} cm^{-3}$ for the core growth and for the shell growth, $7 \times 10^{18} cm^{-3}$. The final dimensions of the p core where a length of ~2.5 µm and a diameter of ~250 nm. After the annealing step 10 min radial growth of undoped shell was grown using same conditions as in the radial p-part. This step was to make sure that the p and n part are separated. Finally 30 min of Si doped n-part was doped using a corresponding planar doping level of $7 \times 10^{18} cm^{-3}$

3) After the NW growth, first a filler, SU-8 photo resist, is spun-on at 4000rpm for 45s and cured with 1min UV light and 3min on a hotplate at 185°C. Then an etch-back with 1-3 min of oxygen plasma etch is performed to leave the top of the nanowire free of any filler.
4) The top contact is then made by standard e-beam lithography. After the development the sample is etched 30s in oxygen plasma, 5-10 s in BHF, and then quickly transferred (within 1min) to a high vacuum chamber for evaporation of top contact. This is done in order to get a clean and oxide free nanowire top. For the top contacts we have made devices with both Au-Ge-Au top contacts (5nmAu, 6nmGe, and 30nmAu) and 75nm indium-tin-oxide (ITO) top contacts. The ITO is after liftoff heat treated at 185°C for 3 min to obtain higher transparency. The Au-Ge-Au contact gives a good N-type contact. Contact to the back side of the silicon wafer is done by standard silver glue. And the electrical circuit is from the backside of the wafer to the top-contact.

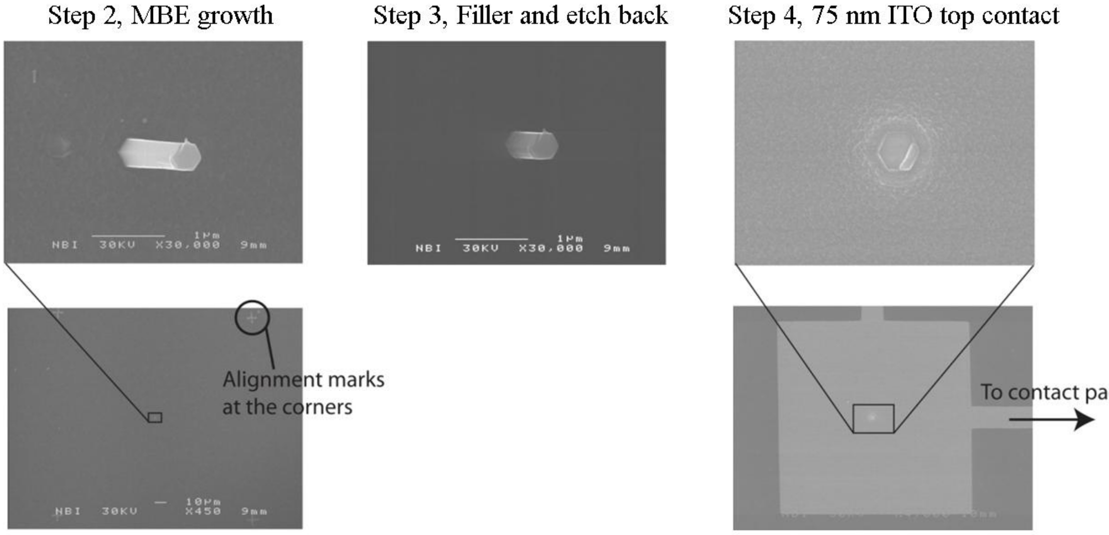

Figure 9-8. SEM images of the last three steps for the fabrication procedure of single vertical nanowire solar cells. The images are tilted 20deg and all images are of the same device.

Measurements on two devices using the ITO top contact will be shown here. The first device shown in Figure 9-9 exhibits an amazing short circuit current density of 180 mA/cm^2 when normalized to the projected area. This leads to an apparent efficiency of 40%, in spite of the relatively low V_{oc} and FF. The low values of V_{oc} and FF tells us that the p-i-n structure is far from optimized and that there is a huge potential for improvement.

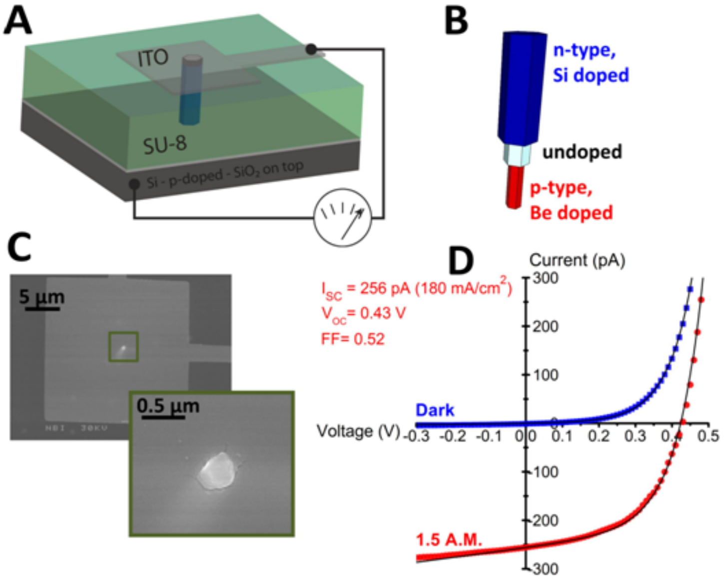

Figure 9-9. This figure is taking from paper [XI]. (A) A illustration of the vertical single nanowire radial p-i-n-device connected to a p-type doped Si wafer with a transparent filler SU8 and a transparent topcontact ITO. (B) Doping structure of the nanowire. The p-type doped core is in contact with the doped Si substrate and the n-type doped shell is in contact with the ITO (C) A SEM image of the device seen from the top electrode. The nanowire is ~2.5 µm high and has a diameter of about 425nm. (D) Current voltage characteristics of the device in the dark and under AM 1.5G illumination, showing a very high apparent short circuit current density.

The second device shows a short circuit current of 173mA/cm^2 and an apparent efficiency of 28%. The reason for these very high efficiencies is the mismatch between the absorption cross-section and the physical bounds of the nanowires, hinting at a very large absorption cross section. Light absorption resonance effects in single standing GaAs nanowires is more than one order of magnitude more efficient than what would be predicted from the Lambert-Beer law.

I-V characteristics of the devices were measured in the dark and under AM 1.5G illumination. Experimental data of device 1 are shown in Figure 9-9 (D). In the dark, the device exhibits typical diode behavior with an ideality factor of 2.6,[89] and a short-circuit current of 256 pA. The diameter of the nanowire is approximately 425nm which corresponds to an apparent photo-generated current density of 180 mA/cm^2. The actual nanowire solar cells are not optimized as seen from the open circuit voltage V_{OC} and fill-factor FF which are respectively 0.43 and 0.52. This indicates that the solar cell device is far from optimized. The NWs can be improved by optimizing the resistivity, thickness of the doped layers[90] and by surface passivation, as seen in section 9.3. The generated power at the maximum power point is 57 pW, corresponding to 40 mW/cm^2. In order to understand the extreme photon collection boost in free standing single GaAs nanowires, a finite element method is used to model a 2,5 µm long nanowire as a function of its diameter and of the wavelength of the plane wave radiation propagating along the nanowire axis.[91,92,93] This is analyzed in detail in ref.[XI]. Two dominant absorption branches for low and high diameters is observed, corresponding to resonances similar to Mie resonances observed in nanowires lying on a substrate. Light absorption in the standing nanowire is enhanced by a factor between 10 and 70 with respect to the equivalent thin film. Another way to express this enhancement in absorption is through the concept of an absorption cross-section. The absorption cross-section is defined as $d_{abs} = d_{NW}\sqrt{\frac{P_{NW}}{P_{macro}}}$ where $\frac{P_{NW}}{P_{macro}}$ is the absorption efficiency. It is largely accepted that the absorption cross-section in nanoscale materials is larger than their physical size. In systems such as quantum dots, the absorption cross-section diameter can exceed the physical size by a factor of up to 8.[94] To further understand the absorption boost in the standing devices, we have spatially mapped the photocurrent generated by device 2 for three different excitation wavelengths: 488, 678 and 800 nm. The results are presented in Figure 9-10 (A) where the EQE in terms of the projected area is plotted for lying and standing NWs.

We see that standing NW configuration is much more efficient in terms photon collection and light concentration. In Figure 9-10 (B), (C) and (D) show a photocurrent mapping at three different wavelengths. It is seen that a photocurrent from an area much larger than the size of the laser spot appears for all three wavelengths. A fit to the data allows estimating an effective absorption cross-section diameter of 1.2 μm (488 nm), 1.0 μm (678 nm) and 1.3 μm (800 nm) respectively. Hence, the absorption boost in our device is due to an unexpected large absorption cross-section of the vertical nanowire geometry. This is equivalent to a built-in light concentration of about 8, which is in good agreement to what the theory predicts, see ref.[XI]. In addition, we speculate that the top contact geometry further contributes to the resonant absorption effect, thereby increasing the absorption cross-section and the boost in photo-generated current. The asymmetric shape in the light absorption mapping especially in (C) and (D) may be due to a slight tilt between the nanowire axis and the incoming light and/or due to a non planar top contact.

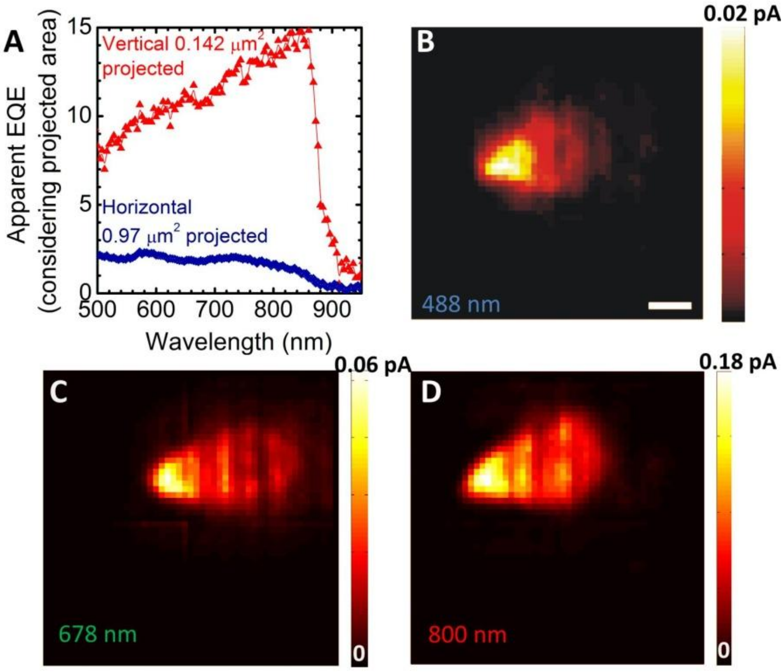

Figure 9-10. Optical characterization of a single nanowire solar cell (device 2). (A) External quantum efficiency (EQE) normalized by indicated projected area where vertical and horizontal nanowire solar cells are compared. As seen for the vertical standing solar cell a 15 fold increase in the photon collection is obtained close to the bandgab. (B-D) Scanning photocurrent measurements on our single vertical nanowire device for three different excitation laser wavelengths, normalized to the incident photon flux. The asymmetric shape in the light absorption mapping especially in (C) and (D) may be due to a slight tilt between the nanowire axis and the incoming light and/or due to a non planar top contact. The scale bar corresponds to 1 μm. This figure is taking from ref.[XI].

This un-optimized solar cell would have a short-circuit current of 20.5 mA/cm^2 and a conversion efficiency of only 4.6%, however improving in the p-i-n junction design (ex. an axial junction to get full benefit from the concentrator effect) and surface passivation can potentially lead to efficiencies even higher than state-of-the-art GaAs solar cells,[95] while still reducing the use of material substantially. In the supplementary information of ref.[XI], two device contacted with Au-Ge-Au top contacts (5nmAu, 6nmGe, and 30nmAu), is presented. Here it is shown that these devices have a much lower I_{SC} compared to the devices presented above which is what would be expected since the Au-Ge-Au top contact is much less transparent than the ITO. The V_{OC} is also lower but only slightly, probably due to the large decrease in I_{SC}, according to eq.(9.4).

In conclusion, a remarkable boost in the light absorption rate in single nanowire solar cells is observed. Especially the vertical configuration of the solar cell NWs leads to a major resonant increase in the light absorption cross-section. These results open a new avenue for third generation solar cells, local energy harvesters for nanoscale devices and photon detectors.

10 Conclusions and outlook

A theoretical formalism is proposed that involves the dynamics of axial III-V nanowire growth via the vapor-liquid-solid mechanism as a function of the basic growth parameters, partial pressures/beam fluxes and substrate temperature. The formalism relies on transition state kinetics driven by minimization of free energy of the total system. All chemical potentials are measured with respect to a common equilibrium reference state where the total system is in a thermodynamical equilibrium. The formalism makes it possible to model and understand the complex mechanisms of nanowire growth dynamics in greater detail and can serve as a strong analyzing tool when optimizing VLS growth of III-V nanowires. The theoretical framework has been implemented into a computer simulation model, and even though the program is in a preliminary stage, it shows good agreement with growth experiments and demonstrates that the theory can be used to model the dynamics of III-V NW growth at a new level of detail.

Dopant incorporation mechanisms during axial and radial NW growth have been discussed in detail. Controlling the doping levels in NWs is extremely important for the impact and applicability of future NW based devices. For the NW solar cells presented in this thesis, it has been necessary to dope the p-type core through a radial growth step, to ensure solar cells with good I-V characteristics.

A series of single NW solar cell experiments on both horizontal and vertical NW have been analyzed and discussed. A general property of the NW solar cells is that they provide a very high short circuit current, which indicates that they are efficient light absorbers. This is seen especially in a state of the art experiment where single standing nanowires as grown on the substrate exhibit a resonant absorption that is enhanced by more than one order of magnitude (a more than 15-fold enhancement). The substantial increase in absorption can be understood by a resonant and broadband increase of the absorption cross-section. Interestingly, the boost in light absorption occurs close to the bandgap, where there is the highest density of photons and where usually one encounters the smallest absorption. Such an enhancement leads in principle directly to an equivalent enhancement of efficiency due to the build-in concentrator property of standing nanowires.

For future research, understanding the growth mechanisms of III-V nanowires via the ‘vapor-liquid-solid’ method is important for controlling the growth of high quality NWs. Moreover, insight is needed in order to see new possibilities and for more efficient realization of both new and existing structures. It is not only important for the fabrication of solar cell devices but also for a wide variety of other applications, such as bio-sensors, high mobility NW transistors, photo-detectors and light emitting diodes.

Even though the understanding of VLS grown nanowires has advanced tremendously in the past decade we are still far from having a general unified and reliable quantitative description of nanowire growth. The theoretical formalism proposed in this thesis may serve as a basic framework to make overall predictions, not only about nanowire growth dynamics by the VLS mechanism, but it can also be adapted to other nanostructured crystal growth systems such as metals, oxides or even carbon nanotube formation from metal particles in chemical vapor deposition chambers. However due to complexity, still many assumptions and approximations are necessary when modeling the growth. For example, a precise modeling of the complete three dimensional liquid-solid NW growth systems still seems like a big challenge. To solve this problem would first require a technique to calculate the equilibrium shape of the total liquid-solid NW system exactly. To do this, a comprehensive set of extensive parameters is needed to make the full description. These parameters could then serve as a reference for the dynamic treatment in terms of thermodynamic driving forces. Also many other details of VLS growth needs to be addressed in higher detail, such as nucleation mechanisms and rates, secondary adsorption, impurity incorporation, controlled growth of axial heterostructures and other advanced structures. All of which I hope to get a chance to study in future projects. But it is generally hoped that the field of nanowire growth research will keep on moving forward in the understanding in the same pace as in the last few years.

In the case of NW photovoltaics, the next step will be to optimize the internal efficiency in the structures and characterize them as grown on the substrate (as shown section 9.5).

The extreme light absorption rate in these wires shows an enormous potential and may open a new avenue for third generation solar cells, local energy harvesters for nanoscale devices and photon detectors, and also for the general understanding of photovoltaic properties of nanowire based devices. This will without question be an interesting field to follow in the coming years.

11 Appendices

11.1 Appendix A. Adatom density calculations in a Fickian diffusion scheme

Here we will merge the adatom diffusion approach developed by Dubrovskii et al.[28] and Johansson et al.[29] with the framework of transition state kinetics. Solving the coupled adatom diffusion equations for diffusion along the NW facets and on an isotropic substrate, $D_{NW,i}\frac{d^2}{dz^2}\rho_{NW,i}(z) = D_{NW,i}\frac{\rho_{NW,i}(z)}{\lambda_{NW,i}^2} - f_{NW,i} - \Gamma_{sa(NW),i} - \Gamma_{va(NW),i}$ and $D_{sub,i}\frac{1}{r}\frac{d}{dr}\left(r\frac{d}{dr}\rho_{sub,i}(r)\right) = D_{sub,i}\frac{\rho_{sub,i}(r)}{\lambda_{sub,i}^2} - f_{sub,i} - \Gamma_{sa(sub),i} - \Gamma_{va(NW),i}$, with the boundary conditions, eq.(2.20)-(2.22), leads to the following expression for the adatom density on the NW sidewall,

$$\rho_{NW,i}(z) = \frac{\lambda_{NW,i}}{D_{NW,i}} \frac{\left(\begin{array}{l} -\cosh\left(\frac{z}{\lambda_{NW,i}}\right) K_{0,\frac{d_{NW}}{2\lambda_{sub,i}}} D_{NW,i}\lambda_{sub,i}\Delta\Gamma_{al,i} + \cosh\left(\frac{z-L_{NW}}{\lambda_{NW,i}}\right) K_{1,\frac{d_{NW}}{2\lambda_{sub,i}}} \left(\Gamma_{sub,i} D_{NW,i}\lambda_{sub,i}^2 - \Gamma_{NW,i} D_{sub,i}\lambda_{NW,i}^2\right) - \\ \sinh\left(\frac{z}{\lambda_{NW,i}}\right) K_{1,\frac{d_{NW}}{2\lambda_{sub,i}}} D_{sub,i}\lambda_{NW,i}\Delta\Gamma_{al,i} + \cosh\left(\frac{L_{NW}}{\lambda_{NW,i}}\right) K_{1,\frac{d_{NW}}{2\lambda_{sub,i}}} \Gamma_{NW,i} D_{sub,i}\lambda_{NW,i}^2 + \sinh\left(\frac{L_{NW}}{\lambda_{NW,i}}\right) K_{0,\frac{d_{NW}}{2\lambda_{sub,i}}} \Gamma_{NW,i}\lambda_{sub,i}\lambda_{NW,i} \end{array} \right)}{\cosh\left(\frac{L_{NW}}{\lambda_{NW,i}}\right) K_{1,\frac{d_{NW}}{2\lambda_{sub,i}}} D_{sub,i}\lambda_{NW,i} + \sinh\left(\frac{L_{NW}}{\lambda_{NW,i}}\right) K_{0,\frac{d_{NW}}{2\lambda_{sub,i}}} D_{NW,i}\lambda_{sub,i}}$$

(10.1)

where $\Gamma_{j,i} = f_{\perp,i} + \Gamma_{va,i} + \Gamma_{sa,i}$ is the generation flux of *i* adatoms of the *j*'th surface. As we are interested in $\Delta\Gamma_{al,i}$ which is a function of $\rho_{NW,i}(z = L_{NW})$,

$$\Delta\Gamma_{al,i} = \Xi_{al,i}\exp\left(-\frac{\Delta g_{al,i}^{TS,ERS}}{k_B T}\right)\exp\left(\frac{\delta\mu_{a-ERS,i}(\bar{\rho}_{NW,i}(L_{NW}))}{k_B T}\right)\bar{\rho}_{NW,i}(L_{NW}) - \Xi_{al,i}\exp\left(-\frac{\Delta g_{al,i}^{TS,ERS}}{k_B T}\right)\frac{\bar{\rho}_i^{ERS}}{x_i^{ERS}} x_i \exp\left(\frac{\delta\mu_{l-ERS,i}}{k_B T}\right)$$

(10.2)

Thus, isolating for $\rho_{NW,i}$ in eq.(10.1) at $z = L_{NW}$, without isolating $\rho_{NW,i}$ from $\delta\mu_{a-ERS,i}$ we get,

$$\rho_{NW,i}(L_{NW}) = \frac{\begin{pmatrix} \cosh\left(\frac{L_{NW}}{\lambda_{NW,i}}\right) K_{0,\frac{d_{NW}}{2\lambda_{sub,i}}} D_{NW,i}\lambda_{sub,i}\Xi_{al,i} \exp\left(-\frac{\Delta g_{al,i}^{ERS} - \delta\mu_{l-ERS,i}}{k_B T}\right) \frac{\bar{\rho}_i^{ERS}}{x_i^{ERS}} x_i + K_{1,\frac{d_{NW}}{2\lambda_{sub,i}}} \left(\Gamma_{sub,i} D_{NW,i}\lambda_{sub,i}^2 - \Gamma_{NW,i} D_{sub,i}\lambda_{NW,i}^2\right) \\ -\sinh\left(\frac{L_{NW}}{\lambda_{NW,i}}\right) K_{1,\frac{d_{NW}}{2\lambda_{sub,i}}} D_{sub,i}\lambda_{NW,i}\Xi_{al,i} \exp\left(-\frac{\Delta g_{al,i}^{ERS} - \delta\mu_{l-ERS,i}}{k_B T}\right) \frac{\bar{\rho}_i^{ERS}}{x_i^{ERS}} x_i + \cosh\left(\frac{L_{NW}}{\lambda_{NW,i}}\right) K_{1,\frac{d_{NW}}{2\lambda_{sub,i}}} \Gamma_{NW,i} D_{sub,i}\lambda_{NW,i}^2 + \sinh\left(\frac{L_{NW}}{\lambda_{NW,i}}\right) K_{0,\frac{d_{NW}}{2\lambda_{sub,i}}} \Gamma_{NW,i}\lambda_{sub,i}\lambda_{NW,i} \end{pmatrix}}{\begin{pmatrix} \frac{D_{NW,i}}{\lambda_{NW,i}} \left(\cosh\left(\frac{L_{NW}}{\lambda_{NW,i}}\right) K_{1,\frac{d_{NW}}{2\lambda_{sub,i}}} D_{sub,i}\lambda_{NW,i} + \sinh\left(\frac{L_{NW}}{\lambda_{NW,i}}\right) K_{0,\frac{d_{NW}}{2\lambda_{sub,i}}} D_{NW,i}\lambda_{sub,i}\right) + \frac{1}{\rho}\cosh\left(\frac{L_{NW}}{\lambda_{NW,i}}\right) K_{0,\frac{d_{NW}}{2\lambda_{sub,i}}} D_{NW,i}\lambda_{sub,i}\Xi_{al,i} \exp\left(-\frac{\Delta g_{al,i}^{ERS} - \delta\mu_{a-ERS,i}}{k_B T}\right) \\ -\frac{1}{\rho}\sinh\left(\frac{L_{NW}}{\lambda_{NW,i}}\right) K_{1,\frac{d_{NW}}{2\lambda_{sub,i}}} \lambda_{NW,i}\Xi_{al,i} \exp\left(-\frac{\Delta g_{al,i}^{ERS} - \delta\mu_{a-ERS,i}}{k_B T}\right) \end{pmatrix}}$$

(10.3)

where ρ is the density of adatom sites (Note that $\Xi_{al,i}$ is a triple line flux, i.e. a particle transfer per length per time). If we assume a barrier free *al* transition, the exponentials vanish in eq.(10.3) and the only dependence on $\delta\mu_{a_j-ERS,III(V)}$ is through the diffusion lengths as treated in Appendix diff. $\delta\mu_{a_j-ERS,III(V)}\left(\rho_{j,III},\rho_{j,V},T\right)$ at $z = L_{NW}$ can now be solved numerically at every step time in a double iterative process for both $\bar{\rho}_{j,III}\left(z = L_{NW}\right)$ and $\bar{\rho}_{j,V}\left(z = L_{NW}\right)$ choosing certain initial values, step size and acceptable error values depending on the computation time available and accuracy needed. The principle of a single numerical computation loop in a typical math language (here Mathcad) is shown below,

$$\delta\mu_{a_j-ERS,III(V)}\left(\rho_{NW,i},T,\delta\mu_{quess,III},\delta\mu_{quess,V},step,error\right)_i \cong \left| \begin{array}{l} \delta\mu_{III(V)} \leftarrow \delta\mu_{quess,III(V)} \\ \delta\mu_{V(III)} \leftarrow \delta\mu_{quess,V(III)} \\ \Delta_{III(V)} \leftarrow 1eV \\ while \left|\Delta_{III(V)}\right| > error \\ \quad \left| \begin{array}{c} F_{III} \leftarrow \delta\mu_{a_j-ERS,III}\left(\rho_{j,III}\left(L_{NW},\delta\mu_{III}\right),\rho_{j,V}\left(L_{NW},\delta\mu_V\right),T\right) \\ F_V \leftarrow \delta\mu_{a_j-ERS,V}\left(\rho_{j,III}\left(L_{NW},\delta\mu_{III}\right),\rho_{j,V}\left(L_{NW},\delta\mu_V\right),T\right) \\ G_{III} \leftarrow \delta\mu_{III} \\ G_V \leftarrow \delta\mu_V \\ \Delta_{III} \leftarrow F_{III} - G_{III} \\ \Delta_V \leftarrow F_V - G_V \\ \delta\mu_{III(V)} \leftarrow \delta\mu_{III(V)} + step\cdot sign(\Delta_{III(V)}) \quad if \quad \left|\Delta_{III(V)}\right| > error \wedge \left|\Delta_{V(III)}\right| > error \end{array} \right. \\ \begin{pmatrix} \delta\mu_{III} \\ \delta\mu_V \end{pmatrix} \end{array} \right.$$

(10.4)

where $\delta\mu_{a_j-ERS,III(V)}\left(\rho_{j,III}\left(L_{NW},\delta\mu_{III}\right),\rho_{j,V}\left(L_{NW},\delta\mu_V\right),T\right)$ is given by eq.(2.12) with $\bar{\rho}_{j,III(V)}\left(L_{NW},\delta\mu_{III(V)}\right)$ being the value from eq.(10.3). The calculated value of

$\delta\mu_{a_{NW}-ERS,III(V)}$ is a 1x2 matrix with $\delta\mu_{a_{NW}-ERS,III}$ and $\delta\mu_{a_{NW}-ERS,V}$ on each position. Note that much computation time is saved by choosing the simplest version $\delta\mu_{a_{NW}-ERS,i}\left(\rho_{NW,i},T\right)\cong k_B T\ln\left(\frac{\bar{\rho}_{NW,i}\left(z=L_{NW}\right)}{\bar{\rho}_{NW,i}^{ERS}}\right)$, which only requires one iteration loop for each element at each time step, which may be a rough but fairly reasonable simplification if only looking at axial growth. After this step, $\delta\mu_{a_{NW}-ERS,i}\left(\rho_{NW,i},T\right)$, is finally put into eq.(10.3) which is again put into eq.(10.2) and (10.1). Solving for the adatom density on the isotropic substrate (which is a reasonable approximation on (111) surfaces and amorphous oxide layers), leads to the following solution,

$$\rho_{sub,i}(r)=\frac{\lambda_{sub,i}}{D_{sub,i}}\frac{\left(\cosh\left(\frac{L_{NW}}{\lambda_{NW,i}}\right)K_{1,\frac{d_{NW}}{2\lambda_{sub,i}}}\Gamma_{sub,i}D_{sub,i}\lambda_{sub,i}\lambda_{NW,i}+\sinh\left(\frac{L_{NW}}{\lambda_{NW,i}}\right)K_{0,\frac{d_{NW}}{2\lambda_{sub,i}}}\Gamma_{sub,i}D_{NW,i}\lambda_{sub,i}^{2}+\left(\left(\Gamma_{NW,i}\lambda_{NW,i}^{2}-\Gamma_{sub,i}D_{NW,i}\lambda_{sub,i}^{2}\right)\cosh\left(\frac{L_{NW}}{\lambda_{NW,i}}\right)+\Delta\Gamma_{al,i}\lambda_{NW,i}D_{sub,i}\right)K_{0,\frac{r}{\lambda_{sub,i}}}\right)}{\cosh\left(\frac{L_{NW}}{\lambda_{NW,i}}\right)K_{1,\frac{d_{NW}}{2\lambda_{sub,i}}}D_{sub,i}\lambda_{NW,i}+\sinh\left(\frac{L_{NW}}{\lambda_{NW,i}}\right)K_{0,\frac{d_{NW}}{2\lambda_{sub,i}}}D_{NW,i}\lambda_{sub,i}}\tag{10.5}$$

11.2 Appendix B. Temperature and chemical potential independent parameters used for GaAs NW growth modelling

(Values without references are fitting parameters or estimated values.)

Parameters	**Values**	**Ref.**
$\Xi'_{al,Ga}$	$1 \cdot 10^4 nm^{-1} s^{-1}$	-
$\Xi'_{al,As}$	$1 nm^{-1} s^{-1}$	-
$\Xi_{ls,III-V} \exp\left(-\frac{\delta g^{TS,ERS}_{ls,III-V}}{k_B T} \right)$	$1 \cdot 10^3 nm^{-2} \cdot s^{-1}$	$at\ T = 630°C$
$\bar{Z}'_{aa,III}$, $\bar{Z}'_{aa,V}$	$1 \cdot 10^{-3}$	-
$\bar{Z}'_{as,III}$ $\bar{Z}'_{as,V}$	$1 \cdot 10^{-15}$	-
$\bar{Z}'_{av,III}$, $\bar{Z}'_{av,V}$	$1 \cdot 10^{-2}$	-
$\bar{Z}'_{av,III,sub}$, $\bar{Z}'_{av,V,sub}$	$1 \cdot 10^{-3}$	-
$\Delta h^{ERS}_{aa,\{1\bar{1}0\},Ga}$	$0.3 eV$	[70]
$\Delta h^{ERS}_{aa,\{1\bar{1}0\},As}$	$0.65 eV$	[70]
$\Delta h^{ERS}_{aa,\{111\},Ga}$	$0.3 eV$	[70]
$\Delta h^{ERS}_{av,\{1\bar{1}0\},Ga}$	$2.3 eV$	[70]
$\Delta h^{ERS}_{av,\{1\bar{1}0\},As_2}$	$2 eV$	[70]
$\Delta h^{ERS}_{av,SiO_x,i}$	$1 eV$	-
$\Delta h^{ERS}_{as,SiO_x,i}$	-	[96]
$\gamma_{vs,ZB\{311\}} // \gamma_{vs,WZ\{\bar{1}2\bar{1}2\}}$	$7 \frac{eV}{nm^2}$	-

$\gamma_{vs,ZB\{201\}} // \gamma_{vs,WZ\{\bar{1}2\bar{1}1\}}$	$6\frac{eV}{nm^2}$	-
$\gamma_{vs,ZB\{312\}} // \gamma_{vs,WZ\{\bar{1}2\bar{1}3\}}$	$7\frac{eV}{nm^2}$	-
$\gamma_{vs,ZB\{111B\}} // \gamma_{vs,WZ\{1000B\}}$	$5\frac{eV}{nm^2}$	-
$\gamma_{vl}(liquid\ Ga)$	$4.2\frac{eV}{nm^2}$	[97]

Facets and angles of lowest miller index orientations.

ZB facets			WZ facets	
$\omega = \{-30°, 90°..\}$	$\omega = \{0°, 60°..\}$	$\omega = \{30°, 150°..\}$	$\omega = \{-30°, 30°..\}$	$\omega = \{0°, 60°..\}$
$\{2\bar{1}\bar{1}\}A$ $\theta_T = 0°$	$\{10\bar{1}\}$ $\theta_T = 0°$	$\{11\bar{2}\}B$ $\theta_T = 0°$	$\{0\bar{1}10\}$ $\theta_T = 0°$	$\{\bar{1}2\bar{1}0\}$ $\theta_T = 0°$
$\{3\bar{1}\bar{1}\}$ $\theta_T = 10°$	$\{31\bar{1}\}$ $\theta_T = 31.5°$	$\{11\bar{1}\}$ $\theta_T = 19.5°$	$\{0\bar{2}21\}$ $\theta_T = 15.0°$	$\{\bar{1}2\bar{1}1\}$ $\theta_T = 17.1°$
$\{100\}$ $\theta_T = 35.3°$	$\{210\}$ $\theta_T = 50.8°$	$\{22\bar{1}\}$ $\theta_T = 35.3°$	$\{0\bar{1}11\}$ $\theta_T = 28.1°$	$\{\bar{1}2\bar{1}2\}$ $\theta_T = 31.7°$
$\{211\}$ $\theta_T = 70.5°$	$\{321\}$ $\theta_T = 67.8°$	$\{110\}$ $\theta_T = 54.7°$	$\{0\bar{1}12\}$ $\theta_T = 46.9°$	$\{\bar{1}2\bar{1}3\}$ $\theta_T = 42.8°$

Table 3. Facets for ZB and WZ structure for the upper hemisphere with the lowest predicted surface energies are described with a set of angles (ω, θ) as shown in. $\theta_T = 0°$ is defined to be the growth axis.

Parameters for the simulations of the truncation dynamics are shown in Table 4.

Simulation no.	$\theta_{T\_,0} = \theta_{T+,0}$	ξ_0	w_{hkl}	σ	γ_{vs0}	c_{hkl}
S1	50.8°	120°	10°	0.35	$10\frac{eV}{nm^2}$	1
S2	50.8°	110°	8°	0.4	$9\frac{eV}{nm^2}$	1
S3	50.8°	120°	15°	0.4	$9\frac{eV}{nm^2}$	0.71
S4	31.5°	–	3°	0.4	$8\frac{eV}{nm^2}$	1
S5	50.8°	–	15°	0.4	$9\frac{eV}{nm^2}$	0.71
S6	50.8°	130°	15°	0.5	$9\frac{eV}{nm^2}$	0.71

Table 4. Six types of simulations of 15 sec of Ga catalyzed GaAs growth in the single slice construction. Initial conditions marked with a subscript $_0$. 15 sec of growth was in all these cases enough to go into a quasi steady state growth mode. Basic growth conditions are in all cases: $\frac{f_V}{f_{III}} = 10$, $GR_{planar} = 0.3\frac{\mu m}{hr}$ and $T = 630°C$. The time steps are $\Delta t = 0.001s$ and at $t = 0$ the liquid composition is $x_{As} = 0.01$ and the truncation height is $\Delta z_{-,0} = \Delta z_{+,0} = -1nm$. All simulations are modeling the formation of ZB structure at $\omega = 0°$ where the structure is symmetric around the growth axis in the single slice construction.

11.3 Appendix C. Trigonometric relations for the single slice modeling

Following the single slice construction shown in Fig.1 (b), the associated trigonometric quantities are given by:

$$\begin{aligned}
\vartheta\left(\Delta z_{+},\Delta z_{-},d_{NW}\right) &= arctan\left(\frac{\Delta z_{+}-\Delta z_{-}}{d_{NW}}\right)\\
d_{eff}\left(\Delta z_{+},\Delta z_{-},d_{NW}\right) &= \frac{d_{NW}}{\cos\left(\vartheta\right)}\\
d_{top}\left(\Delta z_{+},\Delta z_{-},\theta_{T}^{+},\theta_{T}^{-},d_{NW}\right) &= d_{NW}-\Delta z_{-}\,\tan(\theta_{T-})-\Delta z_{+}\,\tan(\theta_{T+})\\
R_{l}\left(\Delta z_{+},\Delta z_{-},d_{NW},\xi\right) &= \frac{d_{NW}}{2\cos\left(\vartheta\right)\sin(\xi)}\\
H_{l}^{'}\left(\Delta z_{+},\Delta z_{-},d_{NW},\xi\right) &= R_{l}+\Xi(\xi)\sqrt{R_{l}^{2}-\left(\frac{d_{eff}}{2}\right)^{2}}\\
\Xi(\xi) &= \begin{matrix} 1 & for & \xi>\pi/2\\ -1 & for & \xi<\pi/2\end{matrix}
\end{aligned}\tag{10.6}$$

The volumes of the slice shown in Fig. 1(c) are given by:

$$\begin{aligned}
\Delta V_{s,low\pm}\left(\Delta z_{\pm},d_{NW}\right) &= \frac{{d_{NW}}^{2}d\omega^{2}}{8}(\Delta z_{ref}-\Delta z_{\pm})\\
\Delta V_{s,top\pm}\left(\Delta z_{\pm},\theta_{T\pm},d_{NW}\right) &= \frac{d\omega}{6}\Delta z_{\pm}\left[3\left(\frac{d_{NW}}{2}\right)^{2}+\left(\Delta z_{\pm}\,\tan(\theta_{T\pm})\right)^{2}-\frac{3}{2}d_{NW}\Delta z_{\pm}\,\tan(\theta_{T\pm})\right]\\
\Delta V_{s,T\pm}\left(\Delta z_{\pm},\theta_{T\pm},d_{NW}\right) &= \frac{1}{12}d\omega\left(\Delta z_{\pm}\right)^{2}\tan\left(\theta_{T\pm}\right)\left(3d_{NW}-2\Delta z_{\pm}\tan\left(\theta_{T\pm}\right)\right)
\end{aligned}\tag{10.7}$$

and the total liquid and solid volumes are therefore given by

$$\begin{aligned}
\Delta V_{l}\left(\Delta z_{+},\Delta z_{-},\theta_{T+},\theta_{T-},d_{NW},\xi\right) &= \frac{2d\omega}{2\pi}\frac{1}{3}\pi H_{l}^{'2}\left(3R_{l}-H_{l}^{'}\right)-\left(\Delta V_{s,top-}+\Delta V_{s,top+}\right)\\
\Delta V_{S}\left(\Delta z_{+},\Delta z_{-},\theta_{T+},\theta_{T-},d_{NW}\right) &= \Delta V_{s,low-}+\Delta V_{s,top-}+\Delta V_{s,low+}+\Delta V_{s,top+}
\end{aligned}\tag{10.8}$$

respectively. The corresponding number of atoms in the respective phases are given by, $\Delta N_{l(s)} = \frac{\Delta V_{l(s)}}{\Omega_{l(s)}}$, with $\Omega_{l(s)}$ being the atomic volumes. The areas of the side-, truncation-, and top-facet (see Fig. 2(a)) are given by:

$$\begin{gathered}
\Delta A_{vl}\left(\Delta z_{+}, \Delta z_{-}, d_{NW}, \xi\right) = \frac{2\, d\omega}{2\pi} 2\pi\, R_l\, H_l^{'} \\
\Delta A_{ls111}\left(\Delta z_{+}, \Delta z_{-}, \theta_{T+}, \theta_{T-}, d_{NW}\right) = \frac{1}{2} d\omega \left[\left(d_{NW} - \Delta z_{+} \tan(\theta_{T+})\right)^{2} + \left(d_{NW} - \Delta z_{-} \tan(\theta_{T-})\right)^{2}\right] \\
\Delta A_{ls\_T\pm}\left(\Delta z_{\pm}, \theta_{T\pm}, d_{NW}\right) = \frac{1}{2} d\omega \frac{\Delta z_{\pm}}{\cos(\theta_{T\pm})}\left(d_{NW} - \tan(\theta_{T\pm}) \Delta z_{\pm}\right) \\
\Delta A_{vs}\left(\Delta z_{+}, \Delta z_{-}, d_{NW}\right) = \left(2\, \Delta z_{ref} - \Delta z_{-} - \Delta z_{+}\right) \frac{d_{NW}}{2} d\omega
\end{gathered}$$

(10.9)

11.4 Appendix D. Including the effect of a triple line excess

An additional contribution to the free energy of the system may come from an inbalance of capillary forces meeting at the TL.[26] A change in one of the involved interface orientations implies a change in such a TL energy, and we will speak about a 'line stress' which is build in around the TL in order to reach mechanical equilibrium. Such a restoring force is either obtained by an increase in strain per unit TL length in the solid or by a local change in the *vl* curvature on the cost of more *vl* interface. Both effects alter the chemical potentials and therefore have an influence on the dynamics. The effect of TL forces on the growth of NWs was introduced by Schwarz and Tersoff[26], who used the tangential component of the TL force on a locally smooth solid surface to describe the TL motion, and the normal component altering the solid chemical potential at the TL. We will here take a slightly different approach and let the TL equilibration allow to take part in the total free energy minimization process in all dimensions. Because changes in the liquid volume induce changes in the TL excess, we assign the TL excess to the liquid phase for convenience and add an extra term to the liquid chemical potential as

$$\mu_{l,i}(x_{III},x_V,T,\omega)=\mu_{l,i}^{\infty}(x_{III},x_V,T)+\gamma_{vl}\frac{\partial A_{vl}}{\partial N_{l,i}}+\frac{d\Upsilon(\omega)}{dN_{l,i}} \qquad (10.10)$$

Here $d\Upsilon(\omega)$ is the TL tension at ω and Υ is the total TL excess. The effect of the TL force on crystal growth is difficult to quantify mainly because it has been difficult to measure experimentally. Nevertheless if we as in ref.[26] define an effective width of the TL, w_{eff}, the TL force along the pq interfacial component can be written as,

$$f_{pq}=w_{eff}\left(\gamma_{pq}+\gamma_{qw}\cos(\theta_q)+\gamma_{pw}\cos(\theta_p)+\tau\kappa_{pq}\right) \qquad (10.11)$$

where pqw is any cyclic permutation of *vls*. τ is the line excess free energy depending on f_{pq} itself and κ_{pq} the line curvature at ω projected on the pq component. Assuming the TL curvature is negligible, the net force along all interfaces at the TL in eq.(10.11) vanish at equilibrium, and the surface energies and corresponding contact angles are given by $\gamma_{pq} = \frac{\sin(\theta_{w,eq})}{\sin(\theta_{p,eq})}\gamma_{qw}$ and $\cos(\theta_{p,eq}) = \frac{\gamma_{qw}^2 - \gamma_{pq}^2 - \gamma_{pw}^2}{2\gamma_{pq}\gamma_{pw}}$. Away from equilibrium, we will describe the TL excess per length as,

$$d\Upsilon(\omega) = \frac{d_{NW}(\omega)}{2} d\omega \left| f_{TL}(\theta_l(\omega), \theta_s(\omega)) \right| \tag{10.12}$$

with

$$\left| f_{TL}(\theta_l, \theta_s) \right| = \sqrt{f_{ls\|}^2 + f_{ls\perp}^2 + \tau^2\kappa^2} = w_{eff}\sqrt{\left(\gamma_{ls} + \gamma_{vs}\cos(\theta_s) + \gamma_{vl}\cos(\theta_l)\right)^2 + \left(\gamma_{vs}\sin(\theta_s) - \gamma_{lv}\sin(\theta_l)\right)^2 + \tau^2\kappa^2}$$

being the net force per length at ω. The effect of the TL energy on the NW growth depends strongly on the choice of w_{eff}. Thus, for the modelling shown in the previous sections did not include this term.

11.5 Appendix E. Discussion on the derivation of the steady state nucleation rate using the general formulation

Derivation of nucleation rates in literature typically uses the picture of a large homogenous mother phase which is independent of the nucleation rate itself. Thus, one speaks about a given steady state nucleation rate, from a constant net formation of clusters of various sizes. However, because the interface we are considering is too small to hold a representative distribution of clusters, we will speak of it as a probability of finding a given cluster rather than a distribution, and the derivation can be carried out in the same approach as in the classical picture.

Attachment of atoms to a 2D cluster containing *n* pairs comes from the liquid by direct attachment and we will ignore the possibility of two small clusters merging together to form a larger cluster. This gives the general equation for the steady state nucleation rate[98,99]: $j^{st} = c_1\Gamma_{ls}\left[\sum_{n'=2}^{n-1}\frac{\prod_{k=2}^{n'}\Gamma_{s_{n'},l}}{A_{n'}\Gamma_{ls}^{n'-1}}\right]^{-1}$, where c_1 is the concentration of single III-V pairs attached to the interface. The attachment frequency to a cluster containing *n'* pairs is given as $\Gamma_{ls,III-V}A_{n'}$, where $A_{n'}$ are the active step area of the cluster. Using the kinetic formalism presented in section 2, the forward flux is given as, $\Gamma_{ls,III-V} = \Xi_{ls,III-V}x_V \exp\left(-\frac{\delta g_{ls}^{TS,ERS} - \delta\mu_{l-ERS,III-V}}{k_BT}\right)$, using eq.(2.3). The detachment frequency of III-V pairs from a cluster of n' pairs is given by the term $\Gamma_{s_{n'},l}A_{n'}$, where the backward flux is given by $\Gamma_{s_{n'},l,III-V} = \Xi_{ls,III-V}x_V^{ERS}\exp\left(-\frac{\delta g_{ls}^{TS,ERS} - \delta\mu_{s_{n'}-ERS,III-V}}{k_BT}\right)$, using eq.(2.3) and eq.(2.4). $\delta\mu_{s_{n'}-ERS,III-V}$ is here the chemical potential of a cluster of n' pairs. With this the steady state nucleation rate is given as:

$$j^{st} = c_1\Gamma_{ls}\left[\sum_{n'=1}^{n^*-1}\left(\frac{1}{A_{n'}}\left(\frac{x_V^{ERS}}{x_V}\right)^{n'-1}\exp\left(\frac{\sum_{i=2}^{n'}\left(\delta\mu_{s_i-ERS,III-V} - \delta\mu_{l-ERS,III-V}\right)}{k_BT}\right)\right)\right]^{-1} \qquad (10.13)$$

The summation in the exponential $\Delta G_{n'} = \sum_{i=2}^{n'} \left(\delta\mu_{s_i - ERS, III-V} - \delta\mu_{l-ERS, III-V} \right)$ is the formation energy of clusters of size n'. The $\frac{1}{A_{n'}} \left(\frac{x_V^{ERS}}{x_V} \right)^{n'-1}$ term is not included in the typical result of the steady state nucleation rate[43] and is a result of the kinetic approach used here. In the capillary approximation ($n^* >> 1$) the overall summation in eq.(10.13) is typically replaced by an integral. However, the $\frac{1}{A_{n'}} \left(\frac{x_V^{ERS}}{x_V} \right)^{n'-1}$ term complicates the derivation of the analytical expression for the nucleation rate. In any case using the general formulation we see that the nucleation rate is predicted to increase with composition faster than the traditional result. Detailed theoretical analysis of the nucleation rate of finite size systems using different kinetic approaches is currently under process. For the simulations presented in this thesis, we have used the traditional result of the nucleation rate as outlined in section 3.

12 References

---

[1] R.S. Wagner and W. S. Ellis, App. Phys. Lett. 4, 5 (1964)

[2] F. Glas, J. C. Harmand and Patriarche, G. *Phys. Rev. Lett.* 99, 146101 (2007)

[3] E. I. Givargizov, 31, 20 (1975)

[4] K. Hiruma, M. Yazawa, T. Katsuyama, K. Ogawa, K. Haraguchi, M. Koguchi and H. Kakibayashi, J. Appl. Phys. 77, 447 (1995)

[5] V. G. Dubrovskii, N. V. Sibirev, Phys. Rev. E 70, 031604 (2004)

[6] V. G. Dubrovskii, N. V. Sibirev, and G. E. Cirlin, *Technical Physics Letters*, 30, 8 (2004)

[7] V. G. Dubrovskii, G. E. Cirlin, I. P. Soshnikov, A. A. Tonkikh, N. V. Sibirev, Yu. B. Samsonenko, and V. M. Ustinov, Phys Rev B 71, 205325 (2005)

[8] J. Johansson, C. P. T. Svensson, T. Mårtensson, L. Samuelson, W. Seifert, J. Phys. Chem. B., 2005, 109 (2005)

[9] K. A. Dick, C. Thelander, L. Samuelson and P. Caroff , *Nano Lett.*, *10*, 9 (2010)

[10] M. S. Gudiksen, L. J. Lauhon, J. Wang, D. C. Smith and C. M. Lieber, *Nature*, 415 (2002)

[11] J. Johansson and K. A. Dick, *CrystEngComm*, 13 (2011)

[12] Fontcuberta i Morral, A.; Colombo, C.; Abstreiter, G.; Arbiol, J.; Morante, J. R.; *Applied Physics Letters*, 2008, 92, 063112

[13] S. Breuer, C. Pfüller, T. Flissikowski, O. Brandt, H. T. Grahn, L. Geelhaar and H. Riechert, *Nano Lett.*, 11, 3 (2011)

[14] Perea, D. E.; Allen, J. E.; May, S. J.; Wessels, B. W.; Seidman, D. N.; Lauhon, L. J.; NanoLetters, 2006, 6, 2, 181-185

---

[15] Allen, J. E.; Hemesath, E. R.; Perea, D. E.; Lensch-Falk, J. L.; Li, Z, Y.; Yin, F.; Gass, M. H.; Wang, P.; Bleloch, A. L.; Palmer, R. E.; Lauhon, L. J.; *Nature Nanotech*, 2008, 3, 168-173

[16] J. Tersoff, M. D. Johnson and B. G. Orr, *Phys. Rev. Lett.,* 78, 2 (1997)

[17] F. Glas, *J. Appl. Phys.* 108, 073506 (2010)

[18] H. Eyring, *Journal of Chemical Physics,* 3, 107-115 (1935)

[19] The steric factor is here defined as the fraction of the total collision cross section in the p state which leads to a transition

[20] It can be discussed if such an equilibrium state of two or more distinct phases really exists in the pure form in nature as the specific kinetic properties of atomic states at the interfaces are not described within the statistical treatment of thermodynamics. Thus, if we do not require stability at lowest free energy for the interface states, the free energy difference per atom across an interface under dynamical equilibrium conditions would be given as, $\Delta\mu_{pq,i}^{eq} = \delta g_{pq,i}^{TS,eq} - \delta g_{qp,i}^{TS,eq} - k_B T \ln\left(\frac{\bar{c}_{p,i}^{eq}}{\bar{c}_{q,i}^{eq}} \frac{\Xi_{pq,i}}{\Xi_{qp,i}} \right)$, where '*eq*' refers to a stable system but with different chemical potentials. However such an effect will only push the *ERS* parameters a little, and the overall dynamical behavior will remain the same and will therefore not be considered further here.

[21] Even though the prefactors in principle could be derived analytically, it is a complex problem and will eventually involve estimations and simplifications for different entropy contributions and effective coordination numbers and they are therefore more reasonably used as fitting parameters.

[22] F. Glas, *Phys. Status Solidi B* 247, 2, 254–258 (2010)

[23] Here $\delta g_{vl,i}^{TS,ERS}$ is assumed to be more negative than $\delta\mu_{v-ERS,i}$ and $\delta g_{bq,i}^{TS,ERS} < \delta\mu_{b-ERS,i}$ is obvious as the beam has a low entropy and a high enthalpy. For the modeling we generally use $S_{b,i} \approx 1$ and $S_{v,i} \approx 1$. This seems reasonable because it is known that there exist a certain threshold flux for both

---

group III and group V where planar growth rates gets limited by the respective element and gets proportional to the flux of limiting elements. Thus at least for the beam fluxes all elements seem to stick.

[24] F. Hommeril and B. Mutaftschiev, *Phys. Rev. B,* 40, 1 (1988)

[25] T. Rieger, S. Heiderich, S. Lenk, M. I. Lepsa, D. Grützmacher, *Journal of Crystal Growth,* 353, 1 (2012)

[26] K.W. Schwarz and J. Tersoff, *Phys. Rev. Lett.* 102, 206101 (2009)

[27] In this continuum approach, these activation free energies should be seen as effective values depending on the surface reconstruction and the roughness of the facet, and is in principle also temperature dependent. However for a given surface reconstruction, surface roughness and therefore $\Delta g_{sa,i}$ is a slowly varying function of T and can reasonably be ignored at typical growth temperatures of III-V NWs.

[28] V. Dubrovskii et al. *Phys. Rev B,* 79, 205316 (2009)

[29] J. Johansson, C. P. T. Svensson, T. Mårtensson, L. Samuelson, W. Seifert, J. Phys. Chem. B., 2005, 109 (2005)

[30] V. G. Dubrovskii, N. V. Sibirev, R. A. Suris, G. E. Cirlin, V. M. Ustinov, M. Tchernysheva,; J. C. Harmand, *semiconductors*, 40, 9, 1075-1082 (2006)

[31] Seino, K.; Ishii, A. Kawamura, T.; *Jpn. J. Appl. Phys*. 39, 4285 (2000)

[32] K. Brakke, *Exp. Math.* 1, 141 (1992)

[33] X. Yu, H. Wang, J. Lu, J. Zhao, J. Misuraca, P. Xiong, and S. V Molnár, Nanoletters, dx.doi.org/10.1021/nl303323t

[34] K. A. Dick, J. Bolinsson, B. M. Borg, and J. Johansson, *Nano Lett.*, 12, 6 (2012)

[35] If the critical nucleus on the top facet becomes smaller than two atoms the growth obviously becomes diffusion limited. But maybe more relevant, if the NW growth rate is so high that the liquid diffusivity

---

becomes the rate limiting factor for the ML completion we will also speak of going into a diffusion limited growth regime on the topfacet.

[36] V. G. Dubrovskii; N. V. Sibirev, J. C. Harmand, F. Glas, *Phys. Rev. B,* 78, 235301 (2008)

[37] Glas, F. Harmand, J-C and Patriarche, G. *Phys. Rev. Lett.* 104, 135501 (2010)

[38] S.-H. Oh et al., *Science* 330, 489 (2010)

[39] A.D. Gamalski, C. Ducati and S. Hoffmann, *J. Phys. Chem. C* 115, 4413 (2011)

[40] C.-Y. Wen et al. *Phys. Rev .Lett.,* 107, 025503 (2011)

[41] D. Kashchiev, Surface Science 14, 209 (1969)

[42] Y. B. Zeldovich, *Acta Physicochim. USSR* 18, 1 (1943)

[43] I. Markov, Crystal growth for beginners, 2nd, Chapter 2.2, World Scientific, Singapore (2003)

[44] J. Johansson, J. Bolinsson, M. Ek, P. Caroff, and K. A. Dick, *ACS Nano*, *6*, **7** (2012)

[45] Yeh, C-Y.; Lu, Z. W.; Froyen, L. S.; Zunger, A.; *Phys. Rev. Lett.,* 46, 10086 (1992)

[46] V. G. Dubrovskii, G. E. Cirlin, N. V. Sibirev, F. Jabeen, J. C. Harmand, and P. Werner, *Nano Lett.*, 11, 1247–1253 (2011)

[47] O. Redlich and A. Kister, *Ind. Eng. Chem.*, 40, 345-348 (1948)

[48] Ansara et al., *Calphad*, 18, 2 (1994)

[49] A. T. Dinsdale, *Calphad*, 15,4 317-425 (1991)

[50] M. Tmar, A. Gabriel, C. Chatillon and I. Ansara, *Journal of Crystal Growth,* 69, 421-441, (1984)

[51] C. Colombo, D. Spirkoska, M. Frimmer, G. Abstreiter and A. Fontcuberta i Morral, *Phys. Rev. B* 77, 155326 (2008)

[52] S Plissard, G Larrieu, X Wallart and P. Caroff, *Nanotechnology*, 22, 27 (2011)

---

[53] G Wulff, *Zeitschrift fur Krystallographie und Mineralogie*, 34, 449 (1901)

[54] S.-H. Oh et al., *Science* 330, 489 (2010)

[55] A.D. Gamalski, C. Ducati and S. Hoffmann, *J. Phys. Chem. C* 115, 4413 (2011)

[56] C.-Y. Wen et al. *Phys. Rev .Lett.,* 107, 025503 (2011)

[57] S. Abbasoglu and I Sezai, *Engineering with Computers* 23, 2 (2007)

[58] K. A. Dick, P. Caroff, J. Bolinsson, M. E. Messing, J. Johansson, K. Deppert, L. R. Wallenberg and L. Samuelson, *Semicond. Sci. Technol.* 25**,** 024009 (2010)

[59] G. E. Cirlin, V. G. Dubrovskii, Yu. B. Samsonenko, A. D. Bouravleuv, K. Durose, Y. Y. Proskuryakov, B. Mendes, L. Bowen, M. A. Kaliteevski, R. A. Abram and D. Zeze, *Phys. Rev. B* 82, 035302 (2010)

[60] Jabeen, F.; Grillo, V.; Rubini, R.; Martelli, F.; *Nanotechnology*, 9, 275711 (2008)

[61] D. Spirkoska et al. *Phys. Rev. B*, 80, 245325 (2009)

[62] S. O. Mariager, C. B. Sørensen, M. Aagesen, J. Nygård, R. Feidenhans'l, and P. R. Willmott, *Appl. Phys. Lett.* 91, 083106 (2007)

[63] S. O. Mariager, S. L. Lauridsen, C. B. Sørensen, A. Dohn, P. R. Willmott, J. Nygård and R. Feidenhans'l, *Nanotechnology* 21, 11 (2010)

[65] G. Patriarche, F. Glas, M. Tchernycheva, C. Sartel, L. Largeau and J-C Harmand, *Nano Lett. 8,* 6 (2008)

[66] B. Ketterer, E. Uccelli and A. Fontcuberta I Morral, *Nanoscale*, 4, 1789, 2012;

[67] G. Landgren, R. Ludeke, Y. Jugnet, J. F. Morar, and F. J.Himpsel, *Journal of Vacuum Science Technology B: Microelectronics and Nanometer Structures* 2, 351 (1984).

---

[68] M. Kazuya, K. Makoto, and T. Kiyoshi, *Jour. of App. Phys*. 54, 1574 (1983).

[69] V. Pankoke, P. Kratzer and S. Sakong, *Phys. Rev. B* 84, 075455 (2011)

[70] Activation enthalpies are based on DFT calculations are taken from the works; V. Pankoke, S. Sakong and P. Kratzer, *Phys. Rev. B* 86, 085425 (2012); J. N. Shapiro, A. Lin and D. L. Huffaker, *Phys. Rev. B,* 84, 085322 (2011)

[71] See section 5.3.1. in J. Chank, The Mathematics of Diffusion, 2ed. Clarendon Press, Oxford (1975)

[72] L. Tsakalakos et al, *J. Nanophot*. **1**, 013552 (2007)

[73] J. Zhu et al, *Nano Lett*. 9, 279-282 (2009).

[74] G. Mariani et al, *Nano Lett*. 11, 2490 (2011)

[75] O.L. Muskens, J. Gomez-Rivas, R.E. Algra, E.P.A.M. Bakkers, A. Lagendijk, *Nano Lett.* 8, 2638-2642 (2008).

[76] L. Cao et al, Nature Mater. 8, 643-647 (2009); C. Colombo et al, *New J. Phys*. 13, 123026 (2011)

[77] M. Heiss, A. Fontcuberta i Morral, *Appl. Phys. Lett.* 99, 263102 (2011).

[78] T. Kempa et al, *PNAS109*, 1407-1412 (2011).

[79] J. Nelson, *The Physics of Solar cells*, Imperical College Press. (2003)

[80] C. Colombo, M. Heiβ, M. Grätzel, and A. Fontcuberta i Morral, *Appl. Phys. Lett.* 94, 173108 (2009)

[81] Gutsche, C. *et al. Advanced Functional Materials* 22, 929–936 (2011).

[82] Kempa, T. J. *et al. Proceedings of the National Academy of Sciences* 109, 1407–1412 (2012)

[83] M. A. Green, K. Emery, Y. Hishikawa and W. Warta, *Prog. Photovolt: Res. Appl*. 19, 84 (2011)

[84] Meillaud, F., Shah, A., Droz, C., Vallat-Sauvain, E. & Miazza, C. *Solar energy materials and solar cells* 90, 2952–2959 (2006).

---

[85] R. R. LaPierre, *J. Appl. Phys.* 110, 014310 (2011)

[86] Mie, G. *Ann. Phys. 330*, 377-445, (1908)

[87] Nobis, T. Kaidashev, E. M. Rahm, A. Lorenz, M.; Grundmann, M. *Phys. Rev. Lett. 93*, 103903 (2004)

[88] Brongersma, M. L.; Kik, P. G., Eds. Springer Netherlands: Dordrecht, 131, 169 (2007)

[89] Supporting Information of ref.[IX]

[90] J. Nelson, 'The physics of solar cells' Imperial College Press (2003)

[91] A.F. Oskooi et al, Comp. *Phys. Comm.* 181, 687-702 (2010)

[92] J. Kupec, B. Witzigmann, *Opt. Expr*, 17, 10399-10410 (2009)

[93] Cao, L.Y. et al, *Nano Lett.* 10, 439-445 (2010)

[94] Leatherdale, C.A. ; Woo, W.K. ; Mikulec, F.V. ; Bawendi, M.G., *J. Phys. Chem. B* 106, 7619-7622 (2002)

[95] Especially axial junctions, which have the same junction area as the projected area would obtain the full benefit from such concentrator effect, and it would be possible to directly compare performance of GaAs nanowire solar cells under 1 sun with planar GaAs cells under 10 suns.

[96] The number of incorporation sites at the thermal oxide layer is set to zero in the modeling

[97] G. E. Cirlin et al. *Phys. Rev B* 82, 035302 (2010)

[98] R. Becker and W. Döring, *Ann. Phys.* 24, 719 (1935)

[99] W. K. Burton, N. Cabrera and F. C. Frank, *Phil. Trans. R. Soc. Lond. A* 243, 299-358 (1951)